Coherence and Singlet Fission of TIPS-Pentacene Probed by Two-dimensional Electronic Spectroscopy

Jessica M. de la Perrelle

A thesis submitted in partial fulfilment of the requirements for the degree of Master of Philosophy

October 2020

Department of Chemistry
The University of Adelaide
North Terrace Campus
Adelaide, South Australia 5005

Contents

Abstract **v**

Declaration **vii**

Acknowledgements **ix**

Abbreviations **xii**

List of Figures **xv**

List of Tables **xvii**

1 Introduction **1**
1.1 Two-dimensional Electronic Spectroscopy . . . 1
1.2 2DES Data Analysis Techniques . . . 2
1.2.1 Diagrammatic Assignment of Signals . . . 3
1.2.2 Diagrammatic Assignment of Coherence . . . 4
1.2.3 Fourier Transforms and Beating Maps . . . 5
1.2.4 Time-frequency Transforms . . . 7
1.2.5 Global Analysis . . . 8
1.2.5.1 Multi-exponential Models . . . 9
1.2.5.2 Models Incorporating Coherence . . . 10
1.3 Singlet Fission and TIPS-Pn . . . 10
1.4 Research Questions . . . 12

2 Methods **13**
2.1 Materials . . . 13
2.2 Sample Preparation . . . 13
2.2.1 Preparation of Solutions . . . 13
2.2.2 Preparation of TIPS-Pn Nanoparticles . . . 13
2.2.2.1 Optimisation of Re-precipitation Procedure . . . 14
2.3 Steady-state Spectroscopy . . . 15
2.4 Two-dimensional Electronic Spectroscopy . . . 15
2.4.1 Removal of Systematic Error from Ambient Temperature Fluctuation . . . 17
2.5 Broadband Pump-probe Spectroscopy . . . 19

3 Analysis of a Model System using a Flexible Data Analysis Framework **21**
3.1 Steady-state Characterisation of Cresyl Violet . . . 23
3.2 2DES of Cresyl Violet . . . 23
3.2.1 Fourier Transforms . . . 24
3.2.2 Time-frequency Transforms . . . 25
3.2.3 Global Analysis . . . 26

3.2.4 Global Target Analysis 27
3.3 Conclusions 31

4 Coherence of TIPS-Pn in Solution 33
4.1 Steady-state Characterisation of TIPS-Pn Solutions 35
4.2 Pump-probe of TIPS-Pn in Three Solvents 35
4.3 2DES of THF 39
4.4 2DES of TIPS-Pn in THF 44
4.5 Conclusions 51
4.6 Appendix 53
4.6.1 Additional Double-sided Feynman Diagrams 53
4.6.2 Additional CAS for TIPS-Pn in THF 55

5 Singlet Fission and Coherence in Amorphous and Crystalline TIPS-Pn Nanoparticles 59
5.1 Steady-state Characterisation of TIPS-Pn Nanoparticles 61
5.2 2DES of Amorphous TIPS-Pn Nanoparticles 61
5.3 2DES of Crystalline TIPS-Pn Nanoparticles 69
5.4 Conclusions 74
5.5 Appendix 76
5.5.1 Water Control Study 76
5.5.2 Extra CAS for Amorphous TIPS-Pn Nanoparticles, Low Photon Energy 77
5.5.3 PVA Control Studies 79
5.5.4 FT and Beating Maps for Crystalline TIPS-Pn Nanoparticles, High Photon Energy 81

6 Conclusion 83

References 87

Abstract

Two-dimensional electronic spectroscopy (2DES) is a type of ultrafast pump-probe (PP) spectroscopy with high time resolution and broadband pump and probe pulses. The high time resolution makes 2DES ideal for tracking ultrafast processes, and the broadband pump and probe allows 2DES to detect correlation between species or states of the system, which manifests as cross peaks in the 2DES data. Additionally, the broadband pulses allow excitation to a quantum superposition of states, a phenomenon known as coherence. This manifests as oscillatory features in the 2DES data with frequency equivalent to the difference in energy between the two states in the superposition. Analysis of coherence signals can reveal details about the vibrational and electronic structure of the system under investigation.

In this thesis, we begin with a study of the coherence and ultrafast relaxation of cresyl violet, a model two-level system with a single vibrational mode. We develop a flexible framework of data analysis techniques for the interpretation of 2DES data, incorporating Fourier transforms (FTs), time-frequency transforms (TFTs) and global analysis. With this framework, we find that cresyl violet exhibits vibrational coherence at $612\,\mathrm{cm}^{-1}$ with a dephasing lifetime of 600 fs. We find that the energy-dependence of this coherence is highly consistent with that predicted by a simple two-level model with the vibrational mode in both the ground and excited states. Additionally, we observe ultrafast relaxation associated with spectral diffusion and the dynamic Stokes shift with a rate constant of $1/k = 100\,\mathrm{fs}$. This analysis demonstrates a novel algorithm for globally and simultaneously fitting the coherence and kinetics of 2DES data.

We then use the analysis framework to investigate 6,13-bis(triisopropylsilylethynyl)-pentacene (TIPS-Pn) in dilute solutions and nanoparticles (NPs) of two morphologies. In concentrated solutions and solids, TIPS-Pn undergoes singlet fission (SF), an exciton multiplicative process that has the potential to increase the efficiency of photovoltaic devices by reducing energy loss through thermalisation. We use dilute solutions of TIPS-Pn to characterise the singlet states of TIPS-Pn when SF is absent. We observe coherence at $295\,\mathrm{cm}^{-1}$, $520\,\mathrm{cm}^{-1}$, $781\,\mathrm{cm}^{-1}$, $940\,\mathrm{cm}^{-1}$, $1159\,\mathrm{cm}^{-1}$ and $1341\,\mathrm{cm}^{-1}$ with lifetimes from 0.5 ps to 1.5 ps. The $940\,\mathrm{cm}^{-1}$ mode is attributed to non-resonant coherence of the solvent, tetrahydrofuran (THF), and displays surprisingly non-trivial energy-dependence, which is rationalised by a mechanism involving Raman scattering. The remainder of the modes are attributed to vibrational and vibronic coherence of the ground and first excited singlet state of TIPS-Pn.

We then study amorphous TIPS-Pn NPs, in which we observe largely similar coherence to that observed in dilute solutions of TIPS-Pn, indicating that TIPS-Pn has similar vibronic structure in amorphous solids and dilute solutions. We are unable probe SF in amorphous TIPS-Pn NPs due to the SF process being relatively slow compared to the available time window of the instrument. Finally, we investigate crystalline TIPS-Pn NPs. In these NPs, ultrafast SF is observed with a time constant of approximately 75 fs. However, no significant coherence is found, which is likely due to any coherences being outside the detection limits of the instrument. These studies contribute to the current understanding of the coherence of TIPS-Pn as isolated and weakly coupled molecules, which is yet to be fully characterised in the literature.

Declaration

I certify that this work contains no material which has been accepted for the award of any other degree or diploma in my name, in any university or other tertiary institution and, to the best of my knowledge and belief, contains no material previously published or written by another person, except where due reference has been made in the text. In addition, I certify that no part of this work will, in the future, be used in a submission in my name, for any other degree or diploma in any university or other tertiary institution without the prior approval of the University of Adelaide and where applicable, any partner institution responsible for the joint-award of this degree.

I give permission for the digital version of my thesis to be made available on the web, via the University's digital research repository, the Library Search and also through web search engines, unless permission has been granted by the University to restrict access for a period of time.

I acknowledge the support I have received for my research through the provision of an Australian Government Research Training Program Scholarship.

Jessica M. de la Perrelle
October 2020

Acknowledgements

I could not have completed this work without the support of a network of friends, family, and mentors.

Firstly, enormous thanks to my supervisors A/Prof. Tak Kee and A/Prof. David Huang. You have been patient and supportive supervisors and I will always be thankful for your advice, both scientific and otherwise. I'd also like to thank you for the opportunity to travel to conferences and your support in preparing my research for publication.

I'd like to thank the past and present members of the Huang/Kee research group for their friendship and support during my two years in the group. Alex Stuart and Rohan Hudson, you have kept me sane and helped me through no shortage of stressful times. To Dr. Patrick Tapping, thank you for letting me use the instrument you built, and for helping me learn to fix the alignment, then break it, then fix it again. Thanks also for your continual stream of helpful tips and useful bits of code, including the LaTeX thesis template.

To my parents, thank you encouraging me to pursue my passions and find my place in the world. To my housemate and friend, Hamish Pratt, thank you the late-night chats with chocolate and tea. And to my partner, Daniel Overend, thank you for everything. I could not have done this without you.

Abbreviations

2DES two-dimensional electronic spectroscopy

CARS coherent anti-Stokes Raman spectroscopy

CAS coherence-associated spectra

CSRS coherent Stokes Raman spectroscopy

CWT continuous wavelet transform

DAS decay-associated spectra

DLS dynamic light scattering

ESA excited-state absorption

FROG frequency-resolved optical gating

FT Fourier transform

GSB ground-state bleach

LO local oscillator

NOPA non-collinear optical parametric amplifier

NP nanoparticle

NR non-rephasing

ODE ordinary differential equation

PDI polydispersity index

PP pump-probe

PVA poly(vinyl alcohol)

R rephasing

ROF rotating optical flat

SAS species-associated spectra

SE stimulated emission

SF singlet fission

SPWVT smoothed-psuedo-Wigner-Ville transform

STFT short-time Fourier transform

SVD singluar value decomposition

TBP time-bandwidth product

TFT time-frequency transform

THF tetrahydrofuran

TIPS-Pn 6,13-bis(triisopropylsilylethynyl)pentacene

List of Figures

1.1 2DES pulse sequence and BOXCARS geometry schematic 2
1.2 Energy level diagrams for GSB, SE, and ESA pathways 3
1.3 Double-sided Feynman diagrams for GSB, SE, and ESA pathways . . . 4
1.4 Energy level diagrams for GSB, SE, and ESA pathways displaying coherence 5
1.5 Double-sided Feynman diagrams for GSB, SE, and ESA pathways displaying coherence 5
1.6 Chemical structure of TIPS-Pn 11

2.1 Simplified 2DES schematic 16
2.2 FROG traces for high and low photon energy ranges 17
2.3 Ambient temperatures over 12 hr 18
2.4 LO and FT of LO before and after randomisation of T axis collection order 18

3.1 Steady-state absorption, steady-state fluorescence, and structure of cresyl violet 23
3.2 Absorptive slices of 2DES data of cresyl violet, with selected T-slices . 24
3.3 Beating maps for cresyl violet 25
3.4 SPWVT for cresyl violet at selected points 26
3.5 Absorptive DAS from multi-exponential fit to cresyl violet 2DES data, model compared to data for selected T-traces 27
3.6 Absorptive SAS from fitting kinetic model incorporating coherence to 2DES cresyl violet data, model compared to data for selected T-traces . 29
3.7 Amplitude and phase CAS from fitting kinetic model incorporating coherence to cresyl violet 2DES data, with theoretical coherence locations and pathways 30

4.1 Steady-state UV–visible absorption spectrum of TIPS-Pn in three solvents 35
4.2 PP data for TIPS-Pn in three solvents, compared with three solvents without TIPS-Pn 36
4.3 FT of PP data for TIPS-Pn in three solvents, compared with three solvents without TIPS-Pn 37
4.4 Integrated FT of PP data for three solvents with and without TIPS-Pn 38
4.5 Beating maps at $912\,\mathrm{cm}^{-1}$ for THF 39
4.6 Energy level and double-sided Feynman diagrams for Raman processes and non-resonant coherence 40
4.7 2DES data for THF compared with global analysis model 42
4.8 Amplitude and phase CAS for THF 43
4.9 Absorptive slices of 2DES data of TIPS-Pn in THF, selected T-traces and assignment by double-sided Feynman diagrams 44
4.10 Integrated FT for 2DES of TIPS-Pn in THF 45

4.11 Absorptive DAS from global analysis of TIPS-Pn in THF, with selected T-traces . . . 46
4.12 Amplitude and phase CAS at 1341 cm^{-1} from global analysis of TIPS-Pn in THF . . . 47
4.13 Amplitude and phase CAS at 1159 cm^{-1} from global analysis of TIPS-Pn in THF . . . 48
4.14 Amplitude and phase CAS at 295 cm^{-1} from global analysis of TIPS-Pn in THF . . . 49
4.15 Double-sided Feynman diagrams for non-resonant coherence, third-order 53
4.16 Double-sided Feynman diagrams for non-resonant coherence, fifth-order compared to third-order . . . 53
4.17 NR double-sided Feynman diagrams for Figure 4.9 . . . 54
4.18 Amplitude and phase CAS at 940 cm^{-1} from global analysis of TIPS-Pn in THF . . . 55
4.19 Amplitude and phase CAS at 781 cm^{-1} from global analysis of TIPS-Pn in THF . . . 56
4.20 Amplitude and phase CAS at 520 cm^{-1} from global analysis of TIPS-Pn in THF . . . 57

5.1 Steady-state UV–visible absorption of amorphous and crystalline TIPS-Pn NPs . . . 61
5.2 Absorptive slice of 2DES data for amorphous TIPS-Pn NPs, with selected T-traces . . . 62
5.3 Integrated FT for amorphous TIPS-Pn NPs, compared with TIPS-Pn in solution . . . 63
5.4 Absorptive DAS from global analysis of amorphous TIPS-Pn NPs, with T-slices comparing the data to the model . . . 64
5.5 Amplitude and phase CAS at 1340 cm^{-1} from global analysis of amorphous TIPS-Pn NPs . . . 65
5.6 Amplitude and phase CAS 1160 cm^{-1} from global analysis of amorphous TIPS-Pn NPs . . . 66
5.7 Amplitude and phase CAS at 261 cm^{-1} from global analysis of amorphous TIPS-Pn NPs . . . 67
5.8 Representative absorptive 2DES maps for crystalline TIPS-Pn NPs in two energy ranges, with selected T-traces . . . 69
5.9 Comparison of PP data for crystalline TIPS-Pn NPs in the high energy range with parallel and perpendicularly polarised pump and probe . . . 71
5.10 Absorptive singlet and triplet pair SAS from global analysis of crystalline TIPS-Pn NPs, with selected absorptive T-traces compared to the model. 72
5.11 Total beating maps for crystalline TIPS-Pn NPs in the low photon energy range . . . 73
5.12 SPWVT of 2DES data for crystalline TIPS-Pn NPs in the low photon energy range . . . 74
5.13 Absorptive singlet and triplet pair SAS obtained from global fitting to 2DES data for crystalline TIPS-Pn NPs, with selected T-traces, low photon energy range . . . 75
5.14 Beating maps and selected T-traces and their FTs for water in the low photon energy region . . . 76

5.15 Amplitude and phase CAS at $800\,\mathrm{cm}^{-1}$ from global analysis of amorphous TIPS-Pn NPs 77
5.16 Amplitude and phase CAS at $520\,\mathrm{cm}^{-1}$ from global analysis of amorphous TIPS-Pn NPs 78
5.17 Beating maps and selected T-traces and their FTs for PVA in the low photon energy region 79
5.18 Beating maps and selected T-traces and their FTs for PVA in the high photon energy region 80
5.19 Selected beating maps for 2DES data for crystalline TIPS-Pn NPs with high photon energy pulse 81
5.20 Integrated FT of two 2DES data sets for crystalline TIPS-Pn NPs, high photon energy pulses 82

List of Tables

2.1 D_Z and PDI of amorphous TIPS-Pn NPs prepared by re-precipitation . 15

4.1 Comparison of observed PP solvent coherence frequencies with Raman modes 38

4.2 Best-fit lifetimes and coherence frequencies from global analysis of 2DES data for TIPS-Pn in THF 46

5.1 Best-fit decoherence times and coherence frequencies from global analysis of 2DES data for amorphous TIPS-Pn NPs 64

CHAPTER 1
Introduction

1.1 Two-dimensional Electronic Spectroscopy

Two-dimensional electronic spectroscopy (2DES) was developed in the late 1990s as an electronic analogue of 2D-NMR.[1,2] Since then, 2D electronic spectrometers have been used to study ultrafast photophysical phenomena in a range of systems, including organic semiconductors,[3–6] inorganic semiconductor nanocrystals,[7–9] and biological light-harvesting systems.[10–16] 2DES is a form of ultrafast pump-probe (PP) spectroscopy, where short laser pulses are used to excite the system and then probe the effect of that excitation over time. Conventional PP spectroscopy such as transient absorption is widely used to probe photophysical processes, but the use of 2DES as an alternative or complementary technique is increasing as 2DES has a number of advantages over conventional PP spectroscopy.

Two-dimensional electronic spectrometers are generally home-built, and a variety of designs have been reported in the literature.[17,18] All designs require the generation of broadband laser pulses in the UV–visible region, with short pulse duration desirable for high time resolution. 2D electronic spectrometers use a sequence of three broadband pulses with variable time delays between each pulse, illustrated in Figure 1.1a. An excitation energy (ω_1) axis is generated by scanning the time delay, τ, between the first and second pulses, which act as the pump, and observing the interference between the signal and local oscillator (LO). Fourier transform (FT) of the interferogram converts τ to ω_1. The third pulse acts as the probe, and the detection energy (ω_3) axis detected as-is using a CCD spectrometer. Time resolution is built up by scanning the delay time, T, between the second and third pulses. The three delay times τ, T, and t are often referred to as coherence, population, and signal time, respectively. The 2D electronic spectrometer used in this work uses a novel approach to generate the time delays between the three pulses, where a pair of rotating optical flats (ROFs) generate delay between the pulses by varying the thickness of glass that the beam passes through.[19] A common geometry used in 2D electronic spectrometers, including the one used in this work, is the BOXCARS geometry, where the three beams and the LO are arranged on the corners of a square (Figure 1.1b). Conservation of momentum leads to the third-order signal being emitted collinearly with the LO. The two most common pulse orderings are known as rephasing (R) and non-rephasing (NR), given by signal wavevectors $\boldsymbol{k}_s = -\boldsymbol{k}_1 + \boldsymbol{k}_2 + \boldsymbol{k}_3$ and $\boldsymbol{k}_s = +\boldsymbol{k}_1 - \boldsymbol{k}_2 + \boldsymbol{k}_3$, respectively. A description of the generation and compression of the broadband, ultrashort laser pulses and the geometry of the 2D electronic spectrometer used in this work can be found in the Methods, Section 2.4.

The design features discussed above give 2DES a number of advantages over conventional PP experiments such as transient absorption. In 2DES, both the pump and probe energies are derived from a broadband source, while in conventional PP typically only the probe is broadband. The resolution of both pump and probe energy allows for monitoring of changes in absorption as a function of time, pump energy and probe

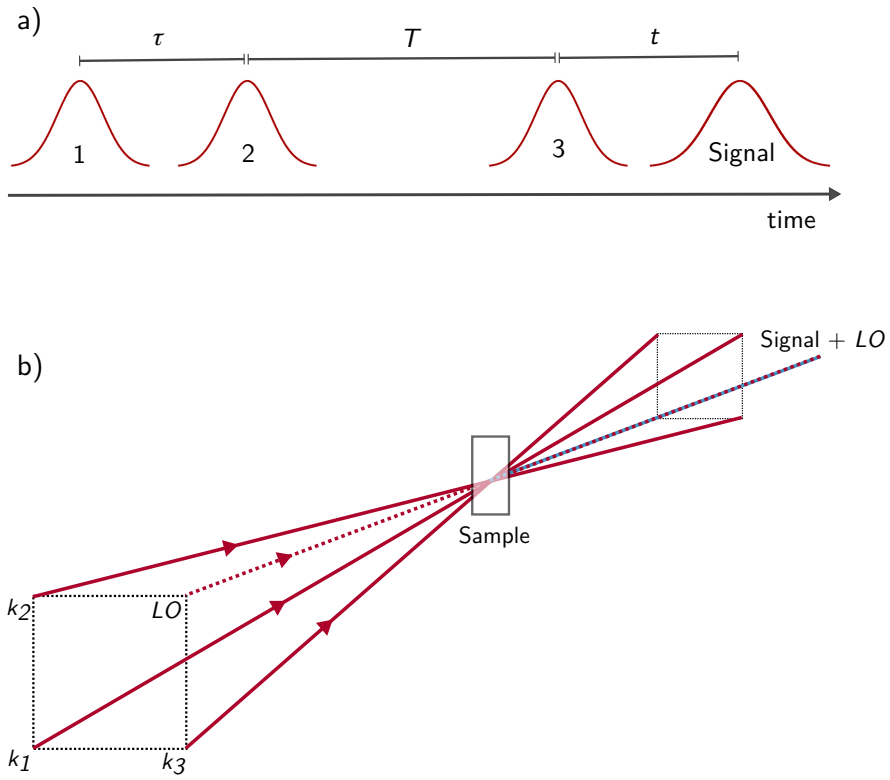

Figure 1.1: (a) Pulse sequence in 2DES. (b) Schematic of the BOXCARS geometry, with the three pulses, LO and signal labelled.

energy. This property enables 2DES to detect cross peaks which indicate correlation between different states or species in the system. Additionally, 2DES usually uses shorter laser pulses and has finer T control than conventional PP spectroscopy, which results in better time resolution and an increased ability to observe very fast processes and short-lived species. Finally, the broadness of the excitation pulses allows excitation to a superposition of quantum states during T. Such a superposition manifests as oscillatory signals in the data, with a frequency corresponding to the energy difference between the two states in the superposition. This phenomenon is known as coherence and can reveal detailed information about the electronic, vibrational or vibronic states of the system.

1.2 2DES Data Analysis Techniques

The complexity of the data generated in 2DES has resulted in the development of a diverse range of data analysis techniques. 2DES data can be interpreted visually, with assignment of signals often aided by data from other spectroscopic techniques such as transient absorption and steady-state absorption or emission spectroscopy. For 2DES, visual interpretation can also be aided by the use of double-sided Feynman diagrams, a diagrammatic representation of the pathways that generate 2DES signals.[20] For data with strong coherences, FTs along the T axis can be used, a technique sometimes referred to as 3D coherent spectroscopy.[21,22] Additionally, time-frequency transforms (TFTs) can be used to obtain both time- and frequency-resolution along the T axis.[23,24]

Furthermore, it is common to decompose the data into decay-associated spectra (DAS) by fitting to a multi-exponential model, and it was recently suggested that this method can be extended to a complex multi-exponential model, which has the advantage of including both coherence and kinetics in one fitting procedure.[25] Once a suitable physical model has been proposed, it is also common to simulate 2DES data using quantum calculations for the purposes of qualitative comparison to the experimental data.

1.2.1 Diagrammatic Assignment of Signals

Similar to other kinds of pump-probe spectroscopy, 2DES signals can be classified into three types: ground-state bleach (GSB), stimulated emission (SE), and excited-state absorption (ESA).[20] Both GSB and SE signals are the result of an increase in transmission (or decrease in absorption) of light of energy ω_3 as a result of absorption of light of energy ω_1. GSB signals arise from bleaching of the ground-state population by the excitation pulse, resulting in an increase in transmission of the detection pulse. SE occurs when the detection pulse triggers the radiative decay of an excited state, again resulting in what appears to be an increase in transmission. By convention, GSB and SE signals have positive intensity in 2DES data, which is usually expressed as the change in probe intensity due to excitation by the pump divided by probe intensity ($\Delta I/I$). In contrast, ESA results from absorption of the detection pulse by an excited-state species. This increase in absorption (decrease in transmission) is represented by a negative $\Delta I/I$.

However, since 2DES involves three ultrashort, broadband laser pulses, the pathways leading to the three signals described above are somewhat more complex than they are in conventional PP spectroscopy. The effect of the three laser pulses can be represented by simple energy level diagrams, as shown in Figure 1.2. In these figures,

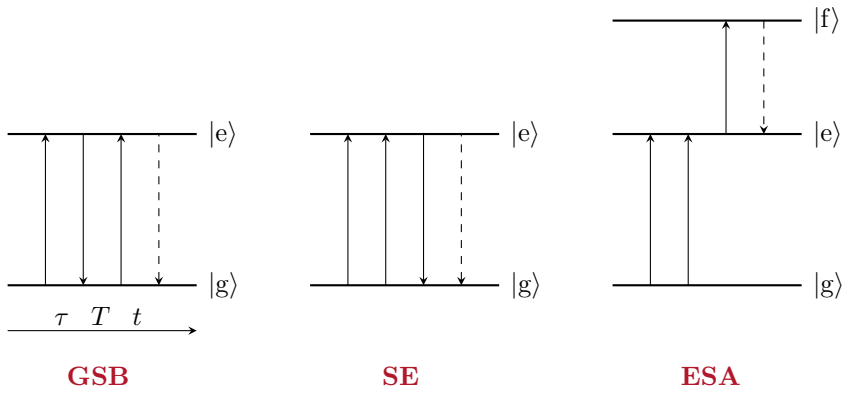

Figure 1.2: Energy level diagrams showing the interaction of the three laser pulses with the sample during GSB, SE and ESA pathways. Each solid arrow represents a single laser pulse, with time flowing from left to right as indicated by the horizontal arrow in the GSB diagram. A dashed arrow represents the detected signal. $|g\rangle$ represents the electronic ground state of the system, and $|e\rangle$ and $|f\rangle$ represent excited states.

time flows from left to right, and solid arrows correspond to the interaction of the three laser pulses, while the dashed arrow indicates the signal. Arrows pointing up represent absorptive interactions, while downward arrows represent emission interactions. These diagrams are accessible to readers outside the field, clearly illustrating the energy of

each pulse and the states involved. However, it is not immediately clear from these diagrams whether the interaction corresponds to a R or NR pathway.

An alternative and more complete diagrammatic representation of the pathways involved in 2DES is double-sided Feynman diagrams.[20] Examples of double-sided Feynman diagrams for the R and NR components of GSB, SE, and ESA signals are found in Figure 1.3. The absorptive ($\mathrm{Re}\{R + NR\}$) part of 2DES data is typically presented,

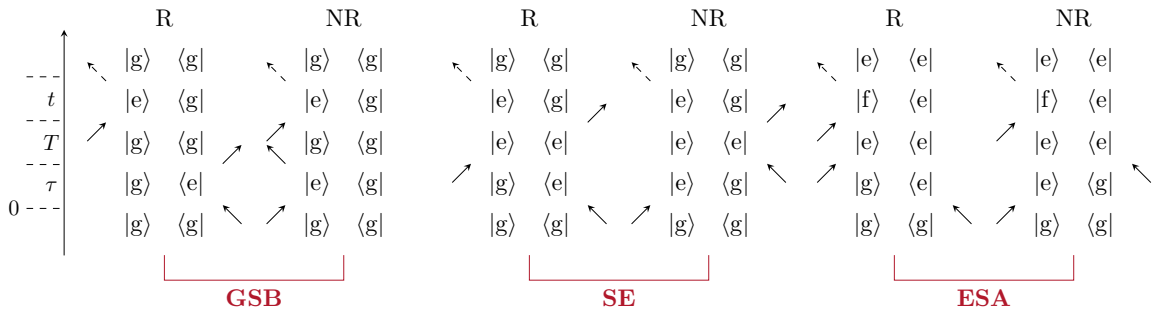

Figure 1.3: Double-sided Feynman diagrams for the R and NR contributions to GSB, SE, and ESA signals for a system with ground electronic state $|\mathrm{g}\rangle$, first electronic excited state $|\mathrm{e}\rangle$ and higher electronic excited state $|\mathrm{f}\rangle$. Time flows from bottom to top, as indicated by the vertical arrow on the left of the diagram. Refer to the main text for further details.

which hence contains contributions from both the R and NR pathways shown. In these diagrams, each solid arrow represents a laser pulse which acts as a perturbation to the system. Arrows pointing inwards represent absorptive interactions, while arrows pointing outwards indicate emissive interactions. The direction of the arrows also represents the direction of their wavevectors: arrows pointing to the right correspond to $+\boldsymbol{k}$, and arrows pointing to the left to $-\boldsymbol{k}$. Hence, R and NR diagrams can be easily distinguished by their differing sequence of left- and right-pointing arrows. The signal is represented by a left-pointing dashed emissive arrow. Time runs from bottom to top, and the time periods between the arrows correspond to the time delays τ, T, and t.

The bras and kets in the center of the double-sided Feynman diagrams represent the elements of the density matrix ρ, a description of the quantum mechanical system which can describe both pure and mixed states. Elements of the form $|\mathrm{A}\rangle\langle\mathrm{A}|$ indicate that the system resides purely in the state $|\mathrm{A}\rangle$, a *population state*, while elements of the form $|\mathrm{A}\rangle\langle\mathrm{B}|$ represent a superposition of states $|\mathrm{A}\rangle$ and $|\mathrm{B}\rangle$, a *coherence state*. If the system is in a coherence state, the probability of finding the system in $|\mathrm{A}\rangle$ or $|\mathrm{B}\rangle$ oscillates with frequency equal to the energy difference between the states $|\mathrm{A}\rangle$ and $|\mathrm{B}\rangle$. Each diagram starts and ends in a population state, and should be in a coherence state during τ and t. The energy difference between the bra and ket during τ and t determines the excitation and detection energy for the diagram. For example a diagram with $|\mathrm{A}\rangle\langle\mathrm{B}|$ appearing during τ will produce a 2DES signal at an excitation energy of $\omega_1 = |\omega_A - \omega_B|$.

1.2.2 Diagrammatic Assignment of Coherence

In the discussion above, diagrams where the system resides in a population state during T are shown. It is also possible for pathways to occur where the system is in a coherence state during T, indicated by $|\mathrm{A}\rangle\langle\mathrm{B}|$ where $\mathrm{A} \neq \mathrm{B}$.[20,26] In this case, the signal will

oscillate with a frequency that is equal to the difference in energy between the two states. Such coherences may be electronic, vibrational or vibronic in nature depending on the characteristics of the states $|A\rangle$ and $|B\rangle$. Energy level diagrams and double-sided Feynman diagrams illustrating vibronic and vibrational coherence are shown in Figures 1.4 and 1.5, respectively. Note that in some cases ω_1 or ω_3 is shifted with respect to the

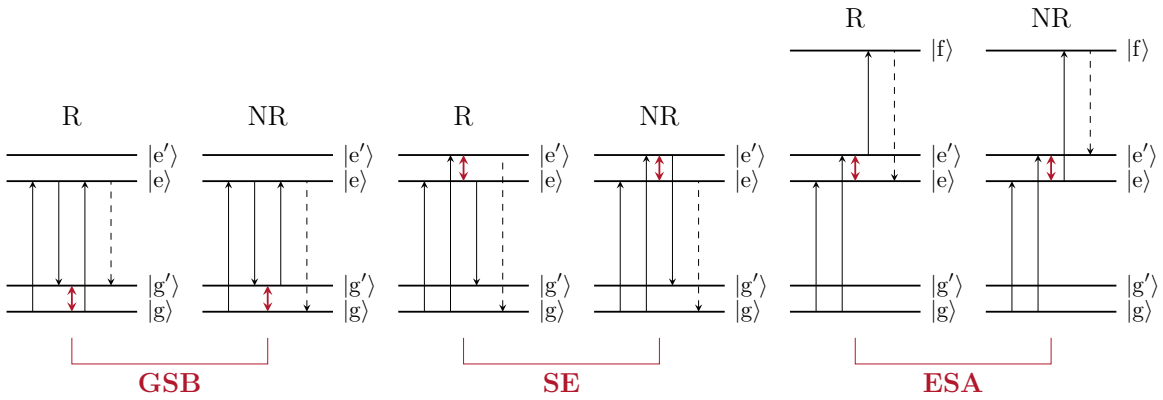

Figure 1.4: Energy level diagrams for a system with ground electronic state $|g\rangle$ and higher electronic states $|e\rangle$ and $|f\rangle$. In this example, vibronic and vibrational coherence are shown, with $|g'\rangle$ and $|e'\rangle$ representing vibrational levels of the $|g\rangle$ and $|e\rangle$ manifolds. R and NR GSB, SE, and ESA pathways are shown and beating frequencies are marked by red arrows.

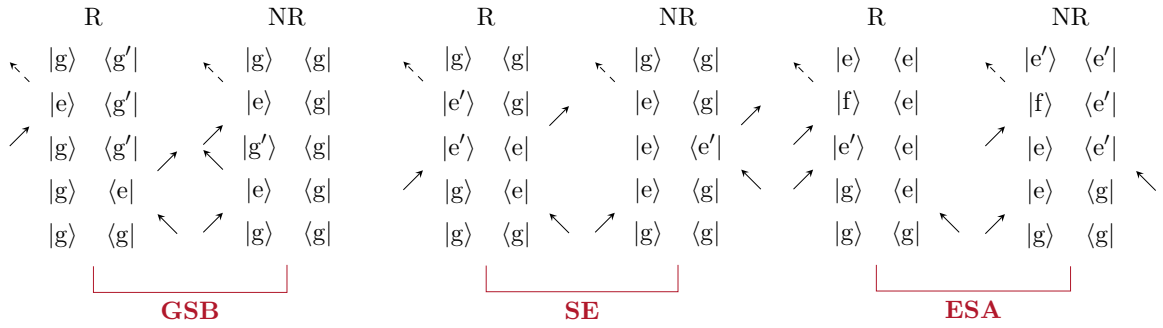

Figure 1.5: Double-sided Feynman diagrams corresponding to the pathways in Figure 1.4.

corresponding non-oscillating case (Figures 1.2 and 1.3) by the coherence frequency. Again, for the purposes of assignment, double-sided Feynman diagrams are preferable over energy level diagrams as they more clearly illustrate the difference between R and NR pathways as well as the states involved in coherence during T.

1.2.3 Fourier Transforms and Beating Maps

A widely used method for analysing oscillating signals is the FT (equation 1.1), which relates the signal in the time domain $s(T)$ to its counterpart in the frequency domain $S(\omega)$.

$$S(\omega) = FT\left\{s(T)\right\} = \int_{-\infty}^{\infty} s(T)e^{-i\omega T}\,dT \tag{1.1}$$

FT along the T axis converts that axis into an additional frequency axis ω_2 and reveals the dominant coherence frequencies of the signal during T. For a 2DES data set, FTs along T can be applied at each ω_1 and ω_3, generating a series of *beating maps* that show

the intensity of each frequency component as a function of ω_1 and ω_3. The advantage of applying FTs in this manner is that the pathways contributing to each coherence signal are separated out along the ω_2 axis, usually resulting in only one pathway per map.[21] Coherence usually appears at different ω_1 and ω_3 in the R and NR components of the data, and hence identifying the origin of coherence is clearer if the FTs are applied to the R and NR data separately. The beating maps corresponding to the total signal can be generated by summing the R and NR maps, due to the linearity of the FT.

Although 2DES data are typically represented as $\mathrm{Re}\{R + NR\}$, when calculating beating maps more information is obtained if the complex form of the R and NR data is retained. For real signals, the FT is symmetric about $\omega_2 = 0$ and only the positive frequencies are usually presented. However, when the signal is complex, the FT becomes non-symmetric about $\omega_2 = 0$ and the sign of the frequency can assist with identifying the source of the coherence. In this case, negative frequencies correspond to diagrams with $|\mathrm{A}'\rangle\langle\mathrm{A}|$ appearing during T and positive frequencies to $|\mathrm{A}\rangle\langle\mathrm{A}'|$, for $E_{\mathrm{A}'} > E_{\mathrm{A}}$.[27] This method has been used previously to identify and interpret coherence in organic semiconductors and photosynthetic systems.[28–30]

Applying a FT along the T axis in this way is an effective method for deconvoluting coherence pathways, however it presents some potential disadvantages. Firstly, FTs mask the possible T-dependence of the amplitude of the oscillatory component, although strongly damped oscillations will appear to have broadened peaks in the Fourier spectrum. Using an FT removes potentially interesting detail about coherences that are transient or short-lived. It would be advantageous to be able to recover the T-domain behaviour of each frequency component to characterise dephasing, which causes the coherence strength to decay over time. Secondly, applying a FT requires removal of the non-oscillatory behaviour of the system in order to dampen the strong $\omega_2 = 0$ signal. This is typically done by fitting the data to a multi-exponential model and applying the FT to the residual. Alternatively, a highpass filter may be applied prior to the FT. Regardless of the method, removing the non-oscillating component necessarily removes information about the kinetics of the system. Hence, the use of FTs forces a two-step analysis procedure, where the kinetics of the system must be analysed first, but this raises the issue that oscillations which the kinetic model cannot account for are still present in the data.

We must also be aware that experimental limitations impose limits on the resolution and range of detectable frequencies. The maximum population time available to the 2D electronic spectrometer used in this thesis is $\sim$500 fs. The limited T window restricts both our sensitivity to low frequencies ($\leq$200 cm^{-1}) and our frequency resolution. The appearance of the FT can be improved by zero-padding the data: adding a series of zeros to the ends of the experimental data to artificially increase the length of the T axis. However, zero-padding only provides a smoothing effect and does not truly increase the ω_2 resolution.

Additionally, the duration and spectral bandwidth of the laser pulses used in 2DES introduce limits to the ability to detect high frequency oscillations. For transform limited pulses, the maximum frequencies imposed by bandwidth and pulse duration of the pulse are equal, but this is not the case for non-transform limited pulses. For example, 12–fs laser pulses will be ineffective at detecting oscillations with periods below around half of the pulse duration, and hence the maximum detectable frequency using this pulse duration is around 1400 cm^{-1}, even if the bandwidth is high enough to excite modes above this limit. Similarly, laser pulses with low spectral bandwidth will

be unable to excite high frequency modes and hence these modes cannot be detected, even if the pulse duration is sufficiently short. These limits depend strongly on the capabilities of a particular instrument.

Coherence can be assigned using beating maps by matching the frequency and position on the beating maps to the corresponding double-sided Feynman diagrams. Although there has been much debate in the literature over the differences between electronic and vibrational coherences, they may in general be differentiated by the appearance of the R and NR beating maps.[27,31] Seibt and Pullerits[27] discuss the appearance of these beating maps for model systems displaying vibrational or electronic coherence. They find that for the model vibronic system the beating maps associated with vibrational coherence show a characteristic pattern of four signals per map, arranged on the corners of a square with side length equal to the coherence frequency. For the model electronic system, coherence manifests as two coherence signals per map, aligned vertically and separated by the coherence frequency. Electronic coherence is also typically much shorter lived than vibrational coherence.[26] However, FTs alone cannot return both frequency- and time-resolved information, and therefore it is desirable to use a signal processing technique that provides both the frequency of an oscillation and its strength over T.

1.2.4 Time-frequency Transforms

TFTs are a broad class of transforms that can be used to analyse a signal in the frequency and time domains simultaneously. Some common TFT algorithms that have previously been used to analyse 2DES data include the short-time Fourier transform (STFT)[32,33] and the continuous wavelet transform (CWT).[34,35] The STFT (equation 1.2) essentially performs a FT on subsets of the data $s(T)$ by applying a windowing function $h(T)$ that slides across the T axis. The windowing function $h(T)$ controls the time-frequency resolution of the STFT; a wider window produces finer frequency resolution and a narrower window produces finer time resolution.

$$\mathrm{STFT}(T,\omega) = \int_{-\infty}^{\infty} s(T')h^*(T'-T)e^{-i2\pi\omega T'}\,dT' \tag{1.2}$$

The CWT (equation 1.3) is a more refined algorithm that replaces the windowing function with an oscillating wavelet function Ψ.

$$\mathrm{CWT}(T,a) = \frac{1}{\sqrt{a}}\int_{-\infty}^{\infty} s(T')\Psi\left(\frac{T'-T}{a}\right)\,dT' \tag{1.3}$$

The wavelet takes a pseudo-frequency parameter, a, which stretches or compresses the wavelet to change its effective frequency. The magnitude of the CWT increases when the effective frequency of the wavelet matches that of the signal and a distribution is built up by scanning a and T. Both the STFT and the CWT are usually plotted as their bilinear versions: the spectrogram $|\mathrm{STFT}|^2$, and the scalogram $|\mathrm{CWT}|^2$.

A variety of other TFT algorithms exist, and their applicability to 2DES analysis has been discussed in detail by Volpato and Collini.[23,24] In particular, the smoothed-psuedo-Wigner-Ville transform (SPWVT)[36–38] has been identified in these works as a reliable bilinear transform with low contamination by artefacts provided that the smoothing windows h and g are chosen appropriately. The SPWVT is defined by equation 1.4.

$$\mathrm{SPWVT}(T,\omega) = \int_{-\infty}^{\infty} h(T') \int_{-\infty}^{\infty} g(T''-T) s\left(T''+\frac{T'}{2}\right) s^*\left(T''-\frac{T'}{2}\right) e^{-2\pi\omega T'}\, dT'\, dT'' \tag{1.4}$$

1.2.5 Global Analysis

Another way to analyse 2DES data is to extract the kinetics of the data using a global analysis algorithm. Global analysis has been an established analysis technique in the field of time-resolved spectroscopy for some time, particularly for transient absorption and time-resolved fluorescence experiments.[39–41] In the simplest case, global analysis involves simultaneously fitting each time-trace of a time-resolved multi-dimensional spectroscopic data set to a linear combination of exponential functions. A common extension of this technique is to fit the data to a particular kinetic model, which often returns more physically meaningful conclusions. The optimisation towards a kinetic model is often called global target analysis. Although these techniques are well-established in the wider field of time-resolved spectroscopy, they are yet to find such widespread used in the analysis of 2DES data. This Section reviews the theory of global analysis in the context of 2DES.

The quantity of data generated by a 2DES experiment can be very large, and hence efficient global analysis requires some mathematical shortcuts. Volpato et al.[25] describe a fitting algorithm which uses singluar value decomposition (SVD)[42] and a variable projection algorithm[43–45] to reduce the computation time required. For the purposes of this discussion we briefly describe it here. The aim of the fitting algorithm is to minimise the difference parameter Δ, given by the squared matrix norm of the difference between the data matrix $\mathbf{Y}$ and the model matrix $\mathbf{M}$ (equation 1.5).

$$\Delta = ||\mathbf{Y} - \mathbf{M}||^2 \tag{1.5}$$

The data matrix $\mathbf{Y}$ is created by reshaping the three-dimensional R and NR data matrices R_{ijk} and N_{ijk}. Indices j and k, which represent the ω_1 and ω_3 axes respectively, are combined into a single frequency index h, and the reshaped matrices are concatenated to form the complete data matrix $\mathrm{Y}_{ih} = [\mathrm{R}_{ih}\ \mathrm{N}_{ih}]$. Prior to reshaping, downsampling (retainment of only every p points) along the ω_1 and ω_3 axes is applied to reduce the size of the data matrices. The appropriate degree of downsampling depends on the data set; for data with relatively broad features ~ 40 points along each energy axis is sufficient, however data with fine or narrow features would benefit from retaining a higher resolution in ω_1 and ω_3.

To further reduce the computational load, SVD is performed on the reshaped matrix $\mathbf{Y}$. SVD expresses $\mathbf{Y}$ as $\mathbf{Y} = \mathbf{U}\mathbf{\Sigma}\mathbf{V}^*$, where $\mathbf{U}$ and $\mathbf{V}$ are unitary and $\mathbf{\Sigma}$ is diagonal. If $\mathbf{Y}$ has dimensions $a \times b$, then $\mathbf{U}$ is $a \times a$, $\mathbf{\Sigma}$ is $a \times b$ and $\mathbf{V}$ is $b \times b$. The diagonal entries of $\mathbf{\Sigma}$ are the singular values of $\mathbf{Y}$, and the columns of $\mathbf{U}$ and $\mathbf{V}$ are the left- and right-singular vectors of $\mathbf{Y}$, respectively. SVD has many uses in linear algebra, but in this case it is used to reduce the size of the matrix $\mathbf{Y}$ and remove experimental noise. In the vector of singular values, typically only the first few are significant; the magnitude of the singular values drops quickly as the vector index increases, and will rapidly plateau at zero for noiseless data or some small non-zero value for noisy data. Only the few larger singular values at the start are considered significant. If

$\mathbf{Y}$ has r significant singular values, it can be re-expressed as $\mathbf{Y'} = \mathbf{U'\Sigma'V'^*}$, where the insignificant singular values and their corresponding singular vectors have been removed such that $\mathbf{U'}$ is $a \times r$, $\mathbf{\Sigma'}$ is $r \times r$ and $\mathbf{V'}$ is $b \times r$. The number of significant singular values is also a good estimate of the number of components required in the model.

Now that the data matrix $\mathbf{Y}$ has been prepared, we consider construction of the model matrix $\mathbf{M}$. $\mathbf{M}$ is decomposed into a matrix $\mathbf{E}$ which contains the model components, and a matrix $\mathbf{A}$ which contains the amplitude of each component of the model (equations 1.6 and 1.7).

$$\mathbf{M} = \mathbf{EA} \tag{1.6}$$

$$\mathrm{M}_{ih} = \sum_{n=1}^{N} \mathrm{E}_{ni}\mathrm{A}_{nh} \tag{1.7}$$

Each column of $\mathbf{E}$ contains a single component of the model. For a kinetic model this may be the concentration curve of a single species, or for an exponential model this would be a single exponential rise or decay. The elements of $\mathbf{A}$ are the amplitudes of each of the N components of the model at each point on the ω_1, ω_3 grid, represented by frequency index h.

The model matrix $\mathbf{M}$ depends on a large number of parameters; for 40 points per energy axis and a 10-component model $10 \times 40^2 + 10 = 16010$ parameters would need to be fitted. However, structuring $\mathbf{M}$ as in equation 1.6 allows for a reduction of the number of parameters that need to be explicitly fitted by the minimisation routine. The parameters have now been separated into N non-linear parameters that are used to generate $\mathbf{E}$ and $N \times h$ linear parameters which are the elements of $\mathbf{A}$. When $\mathbf{E}$ is fixed, the minimisation problem can be solved for $\mathbf{A}$ analytically using equation 1.8, making use of the Moore-Penrose pseudoinverse of $\mathbf{E}$,[46] denoted $\mathbf{E}^+$.

$$\mathbf{A} = \mathbf{E}^+\mathbf{Y'} \tag{1.8}$$

As $\mathbf{A}$ can be computed analytically, the fitting routine needs only to operate on the small set of non-linear parameters which generate $\mathbf{E}$. This method drastically reduces the number of parameters that need to be fit, decreases the number of iterations required for the fitting routine to converge, and increases the probability of converging to the global minimum. After the convergence of the fitting routine, $\mathbf{E}$ is defined, and the final amplitudes can be calculated using equation 1.8 with the original data matrix $\mathbf{Y}$ in the place of the smaller matrix $\mathbf{Y'}$. The model matrix $\mathbf{M}$ can be calculated using equation 1.6. Using this algorithm, the fitting routine converges in minutes on a standard laptop computer.

1.2.5.1 Multi-exponential Models

The most established implementation of this global fitting algorithm is to model the data as a sum of exponentials. This method has been commonly used for transient absorption and time-resolved fluorescence spectroscopy,[41] and has also found widespread use in 2DES data analysis.[11,28,47] In this method each column of $\mathbf{E}$ now corresponds to a single exponential trace with rate parameter $b_n = -1/\tau_n$, where τ_n is the lifetime of the nth component.

$$\mathrm{E}_{ni} = e^{b_n T_i} = e^{-\frac{T_i}{\tau_n}} \tag{1.9}$$

The primary output of this model fitting method are a set of DAS. DAS are the amplitude of each exponential component as a function of ω_1 and ω_3, which are are generated by splitting the matrix $\mathbf{A}$ into its R and NR components ($\mathbf{A}^{\mathrm{R}}$ and $\mathbf{A}^{\mathrm{N}}$) and reshaping them back to the original three dimensions: $\mathrm{A}_{ih} = [\mathrm{A}^{\mathrm{R}}_{ih}\ \mathrm{A}^{\mathrm{N}}_{ih}] \rightarrow \mathrm{A}_{ijk} = [\mathrm{A}^{\mathrm{R}}_{ijk}\ \mathrm{A}^{\mathrm{N}}_{ijk}]$. Absorptive DAS can be calculated as usual by adding the real parts of the R and NR DAS.

Parallel multi-exponential models such as this are suitable for simple systems where the kinetic behaviour can be described by exponential decays. However, in all but the simplest kinetic systems, the DAS do not necessarily correspond to real species or states in the system. More physically meaningful conclusions could be made by fitting the data to a more general kinetic model, however this is not yet a widely used technique in the field.

1.2.5.2 Models Incorporating Coherence

The multi-exponential model described in Section 1.2.5.1 has been extended by Volpato et al. to model coherence with the incorporation of oscillating components.[25] Here, oscillating behaviour is modelled by a sum of exponentials where the b_n parameter is allowed to take complex values. Thus, b_n takes the form $b_n = -1/\tau_n + 2\pi i\omega_n$, where τ_n remains a lifetime parameter and an oscillation frequency ω_n is introduced. The elements of $\mathbf{E}$ are now given by equation 1.10.

$$\mathrm{E}_{nk} = e^{-\frac{T_k}{\tau_n}} e^{2\pi i\omega_n T_k} \tag{1.10}$$

Fitting using this model produces coherence-associated spectra (CAS) for the oscillating components, as well as dephasing rates and coherence frequencies. An important distinction between this model and the real multi-exponential is that the real part of $\mathbf{A}$ is no longer the amplitude for the real part of $\mathbf{M}$. Rather, the CAS are best split into two maps, generated from the amplitude and phase of $\mathbf{A}$. This form of the CAS is advantageous, as the amplitude CAS are directly comparable to the beating maps generated by FTs. The phase CAS also provide additional information not generated by any of the analysis methods discussed so far. Phase maps are known to be difficult to interpret, but theoretical studies have found that they can be useful when distinguishing vibrational from electronic coherences.[31,48] Real systems rarely display coherence in the absence of non-oscillating kinetic behaviour, so in general a model needs to incorporate both oscillating and non-oscillating components. This can be done simply by combining a suitable number of oscillating components (equation 1.10) with multi-exponential model components (equation 1.9).

1.3 Singlet Fission and TIPS-Pn

In this thesis, we use 2DES to investigate the properties of the model chromophore 6,13-bis(triisopropylsilylethynyl)pentacene (TIPS-Pn). TIPS-Pn (Figure 1.6) is a substituted acene which has been extensively studied in solutions,[49] amorphous and crystalline nanoparticles (NPs),[50–55] and polycrystalline thin films.[28,56–61] In concentrated solutions and solids, TIPS-Pn undergoes singlet fission (SF),[62,63] an exciton multiplication process that has been proposed as a way to circumvent the Shockley-Quiesser limit[64] and increase the efficiency of photovoltaic cells.[65]

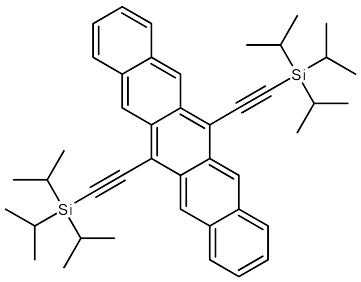

Figure 1.6: The chemical structure of TIPS-Pn.

During SF, a singlet exciton (S_1) on a chromophore couples to a neighbouring ground state (S_0) chromophore, resulting in two triplet excitons (T_1), localised on a pair of neighbouring chromophores (equation 1.11). The process is commonly thought to occur though an intermediate species known as the triplet pair ^{1}(TT), where the two triplet excitons are strongly coupled into a species with overall singlet character.

$$S_0 + S_1 \leftrightharpoons {}^1(TT) \leftrightharpoons T_1 + T_1 \tag{1.11}$$

For efficient SF, S_1 should have at least twice the energy of T_1. The inverse process, triplet fusion, is also possible depending on the energies of S_1 and T_1. Although SF was first observed in the 1960s,[66,67] the mechanism is still under debate, particularly with regards to the strength of the coupling between the singlet and triplet pair states and the involvement of charge transfer states. The SF mechanisms commonly discussed can be split into three classes: direct SF where the singlet proceeds to the triplet pair directly without the involvement of charge transfer states; SF where the singlet to triplet pair conversion is mediated by virtual charge transfer states; and a sequential two-step mechanism where charge transfer states are real intermediates between the singlet and triplet pair.[68] Photovoltaics produced with SF-capable molecules are yet to achieve high efficiencies,[69–73] indicating a need to better understand the SF mechanism, which will help design more efficient SF-based photovoltaics.

For TIPS-Pn in particular, the dynamics of SF vary between the three primary systems: concentration solutions, amorphous solids, and crystalline solids. In solutions, TIPS-Pn SF is concentration dependent, with triplet yields increasing to near 200% with increasing concentration.[49] The triplets are generated at a rate approaching the diffusion limit, and the triplet lifetime is long (6.5 µs).[49] Aggregation through π–π interactions was not observed for TIPS-Pn in chlorinated solvents,[49] leading to the theory that SF occurs through transient collisional interactions in solution, however more recent work[74] suggests that SF in solution occurs when molecules are aggregated through interactions between their side chains. In amorphous TIPS-Pn NPs, SF occurs on the order of a few ps[51,53,55] and the yield of free triplets is decreased to just over 100% due to poor separation of triplet pairs.[51] Finally, in crystalline films and NPs, TIPS-Pn has been observed to undergo SF with high triplet yield and within 100 fs of excitation.[28,53,56,75,76] In all three systems, SF is fast compared to the natural singlet lifetime in the absence of SF: 12 ns in amorphous NPs diluted with inert polymer[51] and 13 ns in dilute solutions.[49] Additionally, studies have found that in crystalline thin films of TIPS-Pn, the vibronic modes of S_1, ^{1}(TT), and T_1 are involved in SF.[28,56] The ultrafast nature of SF in TIPS-Pn and the potential involvement of vibronic states makes this system an ideal candidate for study using 2DES.

1.4 Research Questions

This thesis aims to address two key problems in the existing literature. Firstly, there is a great variety of analysis techniques presently in use for interpreting 2DES data. In the Sections above we have discussed FTs, TFTs and global analysis, however research groups have also made use of centre-line slope analysis[77–80] and compared their 2DES data to simulated data based on quantum mechanical models. We aim to present a unified framework for the analysis of 2DES data. We hope this will lead to greater consistency between research groups and improved accessibility in the literature. As part of this framework, we aim to develop a method for using global analysis algorithms to fit 2DES data to general kinetic models. Global fitting to a kinetic scheme is an analysis method that is under-utilised in the current literature. We plan for this new method to be based on the complex multi-exponential model introduced by Volpato and Collini,[25] but with the added ability to fit to kinetic concentration curves alongside the complex multi-exponential coherence components. Chapter 3 demonstrates this proposed framework using a thorough analysis of 2DES data for cresyl violet, which serves as a model two-level system with a single vibrational mode.

The data analysis framework described in Chapter 3 will then be used to analyse 2DES data for TIPS-Pn in dilute solutions, amorphous NPs, and crystalline NPs. TIPS-Pn has been broadly studied by various time-resolved spectroscopic techniques, but in the literature there are only two studies that investigate TIPS-Pn with sufficiently high time resolution to resolve vibrational coherence. Musser et al.[56] and Bakulin et al.[28] used broadband PP spectroscopy and 2DES, respectively, to study the coherence of the singlet and triplet states of polycrystalline TIPS-Pn thin films. Both studies found rich vibronic structure in the singlet and triplet states. However, the coherence of TIPS-Pn in solutions and amorphous solids has not yet been thoroughly investigated. The role of molecular vibration in SF in amorphous TIPS-Pn is unknown, and studies of the coherence of the singlet states of TIPS-Pn have been complicated by the fast formation of triplets in crystalline TIPS-Pn.

Here, we study TIPS-Pn in dilute solutions where SF is absent[49] in order to characterise the coherence of the singlet states of TIPS-Pn. Additionally, we study TIPS-Pn in amorphous NPs, where the chromophores are weakly coupled and SF is slow.[51] We will complete this study by investigating SF and coherence in crystalline TIPS-Pn, using a recently developed procedure for preparing crystalline TIPS-Pn NPs.[50] Although crystalline thin films of TIPS-Pn have been previously studied by 2DES,[28] our 2D electronic spectrometer operates at a higher photon energy range than that in the existing work,[28] and hence is capable of detecting the strong triplet ESA at higher ω_3. Taken together, these three studies aim to provide an overview of how the coherence of TIPS-Pn depends on inter-chromophore coupling, and to clearly distinguish the vibronic structure of the singlet and triplet states of TIPS-Pn.

CHAPTER 2
Methods

2.1 Materials

TIPS-Pn (99.9%) was used as-purchased from Ossila. HPLC grade tetrahydrofuran (THF) was purchased from RCI Labscan and freshly distilled prior to use. Toluene and acetone were purchased from Chem-Supply. All water was purified by an 18 MΩ Millipore Milli-Q Reagent Water System fitted with a 0.45–µm filter. Cresyl violet perchlorate and poly(vinyl alcohol) (PVA) with an average molecular weight of 130 kg mol^{-1} were purchased from Sigma-Aldrich.

2.2 Sample Preparation

2.2.1 Preparation of Solutions

For 2DES and broadband PP studies of TIPS-Pn in solution, solutions of TIPS-Pn in acetone, toluene and THF were prepared under ultrasonication to a concentration of 0.125 g L^{-1}. Solutions were filtered into a 1–mm path length quartz cuvette (Starna Cells 21-Q-1) through a 0.22–µm syringe filter with a polytetrafluoroethylene membrane (Adelab Scientific). Solutions of TIPS-Pn were protected from light when not in use and monitored for photodegradation during 2DES and PP experiments by steady-state UV–visible absorption spectroscopy. No significant photodegradation was observed during the experiments. For solvent-only sample preparation, solvents were filtered through the same 0.22–µm filters into 1–mm path length quartz cuvettes. A solution of cresyl violet perchlorate was prepared in ethanol in a similar manner.

2.2.2 Preparation of TIPS-Pn Nanoparticles

It has been well established that NP suspensions of TIPS-Pn can be formed by re-precipitation from THF into water.[50,51,53,54] As prepared, these NPs are known to be amorphous in morphology, with the TIPS-Pn molecules packed randomly throughout the NP with no long-range ordering. It has also been reported that amorphous NPs of TIPS-Pn undergo a morphological transition in the presence of chemical additives. Tayebjee et al. reported a slow transition from the amorphous morphology to a more strongly coupled morphology resembling crystalline TIPS-Pn.[52] Pensack et al. found that this morphological transition was triggered by either the use of a syringe containing an uncharacterised syringe lubricant, or by re-precipitation into an aqueous PVA solution.[53] Recently, we have found that amorphous NPs of TIPS-Pn can be reliably converted to a highly ordered, crystalline morphology by the addition of small amounts of PVA.[50]

Amorphous and crystalline TIPS-Pn NPs were prepared by a re-precipitation procedure based on the references in the above discussion. TIPS-Pn in THF (3 mL,

$0.02\,\mathrm{g\,L^{-1}}$) was injected using a glass syringe into 15mL of rapidly stirring water, and stirred for a further 5 minutes. This process was repeated 5–10 times to produce the desired volume of NPs and the fractions were combined. For amorphous NPs, the fractions were concentrated under reduced pressure to a final concentration of $\approx 200\,\mathrm{ppm}$ (maximum absorbance of ≈ 0.5 in a 1–mm path-length cuvette), and filtered through a 0.2–µm syringe filter (Sartorius Minisart NML). The amorphous morphology was confirmed by steady-state UV–visible characterisation, discussed further in Chapter 5, Section 5.1.

To prepare crystalline TIPS-Pn NPs, addition of PVA was used to induce crystallisation of amorphous NPs, as previously reported.[50,52] An aqueous PVA solution was prepared ($10\,\mathrm{g\,L^{-1}}$) by heating to $80\,^{\circ}\mathrm{C}$ for 2 hr. Aqueous PVA was then added to amorphous TIPS-Pn NPs (prepared as described above, 30 ppm) at a mass ratio of 1:1 PVA:TIPS-Pn. The NPs were left to undergo complete crystallisation for a period of approximately one week, monitored by UV–visible absorption spectroscopy. Once the UV–visible absorption spectrum had stabilised to the known spectrum of polycrystalline TIPS-Pn, the NPs were further concentrated to $\approx 200\,\mathrm{ppm}$ (maximum absorbance of ≈ 0.2 in a 1–mm path-length cuvette) and filtered through a 0.2–µm syringe filter.

Samples of amorphous and crystalline TIPS-Pn NPs, water, and 200–ppm aqueous PVA were prepared for 2DES and PP experiments by filtering through a 0.2–µm filter into a quartz cuvette with path length of 1 mm. NP samples were monitored for photodegradation before and after experiments by UV–visible spectroscopy. No significant degradation was observed during the experiments for NPs of either morphology.

2.2.2.1 Optimisation of Re-precipitation Procedure

Cleaner spectroscopic data are achieved with small NPs as light scattering is reduced. Additionally, small NPs are less prone to aggregation, which increases their long-term stability. Hence, the re-precipitation procedure outlined above was optimised to minimise the size and polydispersity of the NPs. A number of parameters were explored: concentration of the injected stock of TIPS-Pn in THF (c_{Pn}), syringe needle size, volume of TIPS-Pn stock injected (v_{Pn}), and volume of water that the TIPS-Pn stock was injected into ($v_{\mathrm{H_2O}}$). The size and polydispersity of the NP dispersions was measured by dynamic light scattering (DLS), using a Malvern Zetasizer Nano ZSP and disposable plastic cuvettes with a 10–mm cell length. The parameters used to measure size and polydispersity were Z-average diameter (D_Z) and polydispersity index (PDI), both of which were obtained by cumulants analysis, which fits a third-degree polynomial to the logarithm of the correlation function.[81] The D_Z and PDI of NPs prepared by various re-precipitation procedures are listed in Table 2.1. For reference, a larger PDI indicates a wider size distribution, with typical values ranging from 0.7 (highly polydisperse) to 0.05 (highly monodisperse).[82]

Initial experimental parameters were chosen to match re-precipitation procedures reported in the literature, listed in methods 1[50] and 5[51] of Table 2.1. Parameters were then varied until suitably small and monodisperse NPs were achieved. Overall, it was found that NP size is primarily controlled by c_{Pn}, where lower concentrations produced smaller NPs. Polydispersity is influenced by a number of factors. In general, lowering v_{Pn} such that the injection of the entire volume takes place in under 5 seconds decreases polydispersity. Syringe aperture size was found to have a weak effect on size and polydispersity. An exhaustive study of all parameters was not undertaken as method 6

Table 2.1: Z-average diameter (D_Z) and PDI of amorphous TIPS-Pn NPs prepared by re-precipitation.

Method No.	c_{Pn} ($\mathrm{g\,L^{-1}}$)	v_{Pn} (mL)	$v_{\mathrm{H_2O}}$ (mL)	Needle size	D_Z (nm)	PDI
1	0.51	0.4	10	large	68.8	0.140
2	0.10	3	20	large	47.5	0.267
3	0.02	15	75	large	44.0	0.240
4	0.51	0.4	10	small	68.8	0.248
5	0.02	15	75	small	32.5	0.264
6	0.02	3	15	small	36.7	0.067

was found to produce near-monodisperse NPs with a small D_Z of approximately 37 nm, suitable for all further experiments.

2.3 Steady-state Spectroscopy

Steady-state UV–visible absorption spectra were collected using a Cary Varian 1E UV–visible spectrophotometer, using a quartz cuvette with a 1–mm or 10–mm path length. Steady-state emission spectra were collected using a Perkin Elmer LS 55 fluorescence spectrophotometer using a 10–mm quartz cuvette (Starna Cells 3-Q-10). Sample absorbances were kept below 0.1 for fluorescence experiments.

2.4 Two-dimensional Electronic Spectroscopy

The 2D electronic spectrometer used in this work has been discussed in detail in the literature.[19] A simplified schematic of the instrument is shown in Figure 2.1. The spectrometer used the output of a Ti:sapphire regenerative amplifier (Spitfire Pro XP 100F, Spectra-Physics), consisting of 100–fs pulses centered at 800 nm with a repetition rate of 1 kHz. This output was directed to a home-built non-collinear optical parametric amplifier (NOPA) pumped at 400 nm to produce broadband pulses with tunable energy. Laser pulses in two energy ranges were used in this project: a lower photon energy range centred at 600 nm, and a higher photon energy range centred at 560 nm. The pulses were compressed by a single-grating and single-prism compressor. Frequency-resolved optical gating (FROG) traces for the two photon energy ranges are shown in Figure 2.2. Pulse durations were 12 fs and 22 fs for the low and high photon energy ranges, respectively, with bandwidths of 66 nm (low photon energy) and 31 nm (high photon energy).

A diffractive optic was used to spilt the compressed output into four beams which were then collimated by a concave mirror into the BOXCARS geometry, where the four beams are positioned at the corners of a square. Two of the beams, $\boldsymbol{k}_1$ and $\boldsymbol{k}_2$, were each individually passed through a pair of ROFs. $\boldsymbol{k}_3$ was passed though a glass flat that provided a constant time delay. Rotation of the two pairs of ROFs changed the thickness of glass that $\boldsymbol{k}_1$ and $\boldsymbol{k}_2$ passed through, and hence controlled the delay times between $\boldsymbol{k}_1$, $\boldsymbol{k}_2$ and $\boldsymbol{k}_3$. The fourth beam passed though a neutral density filter and was used as a LO. The four beams were then focused onto the sample by another concave mirror. The third order signal was emitted from the sample collinearly with

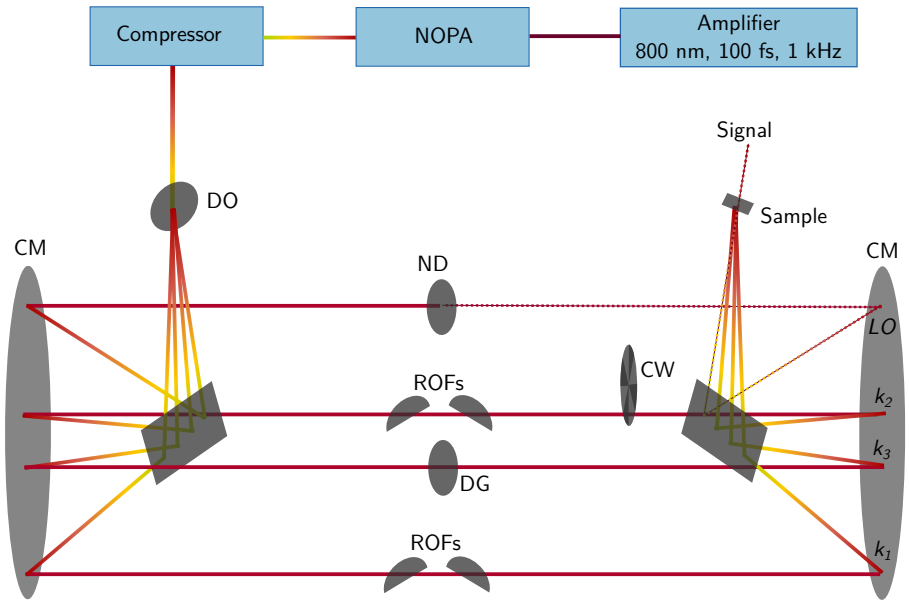

Figure 2.1: Simplified 2DES schematic. The LO, $\boldsymbol{k_1}$, $\boldsymbol{k_2}$, and $\boldsymbol{k_3}$ are labelled. Abbreviations for various optics are: DO, diffractive optic; DG, delay glass; CM, concave mirror; ND, neutral density filter; ROFs, rotating optical flats; and CW, chopper wheel.

the LO, and was detected by a imaging spectrograph and camera (Shamrock SR303-i and Newton 970, Andor). This mixing with the LO allowed the detection energy (ω_3) axis to be generated by heterodyne detection. The excitation energy (ω_1) axis was produced by scanning the time delay τ between $\boldsymbol{k}_1$ and $\boldsymbol{k}_2$, then Fourier transforming along that axis to convert to the frequency domain. Waiting time resolution was built up by scanning the time delay T between $\boldsymbol{k}_2$ and $\boldsymbol{k}_3$.

For the experiments in the high photon energy range, the pulse energy was 85 nJ per pulse with a full-width-at-half-maximum spot size of 30 µm (excitation density $\approx 4.2\,\mathrm{mJ/cm^2}$) at the position of the sample. For the low photon energy experiments, the pulse energy was 60 nJ with a 28 µm spot size (excitation density $\approx 3.4\,\mathrm{mJ/cm^2}$). Both R and NR data were collected, corresponding to signal wavevectors of $\boldsymbol{k}_s = -\boldsymbol{k}_1 + \boldsymbol{k}_2 + \boldsymbol{k}_3$ and $\boldsymbol{k}_s = +\boldsymbol{k}_1 - \boldsymbol{k}_2 + \boldsymbol{k}_3$ respectively. The NR component was obtained by swapping the roles of the first two pulses such that $\boldsymbol{k}_2$ arrived before $\boldsymbol{k}_1$. Data acquisition took approximately 12 hr for population time T ranging from 0 to 500 fs in T-steps of 5 fs. To obtain a well sampled T axis while minimising the data acquisition time for each scan, multiple scans were collected with large T-steps and offset start Ts, then interleaved to create a composite dataset with a small T-step. For example, a dataset with a T-step of 3 fs could be created by interleaving three datasets with T-steps of 9 fs and starting Ts of 0 fs, 3 fs and 6 fs. Experimental noise due to light scattering was removed by applying Savitzky-Golay filters.

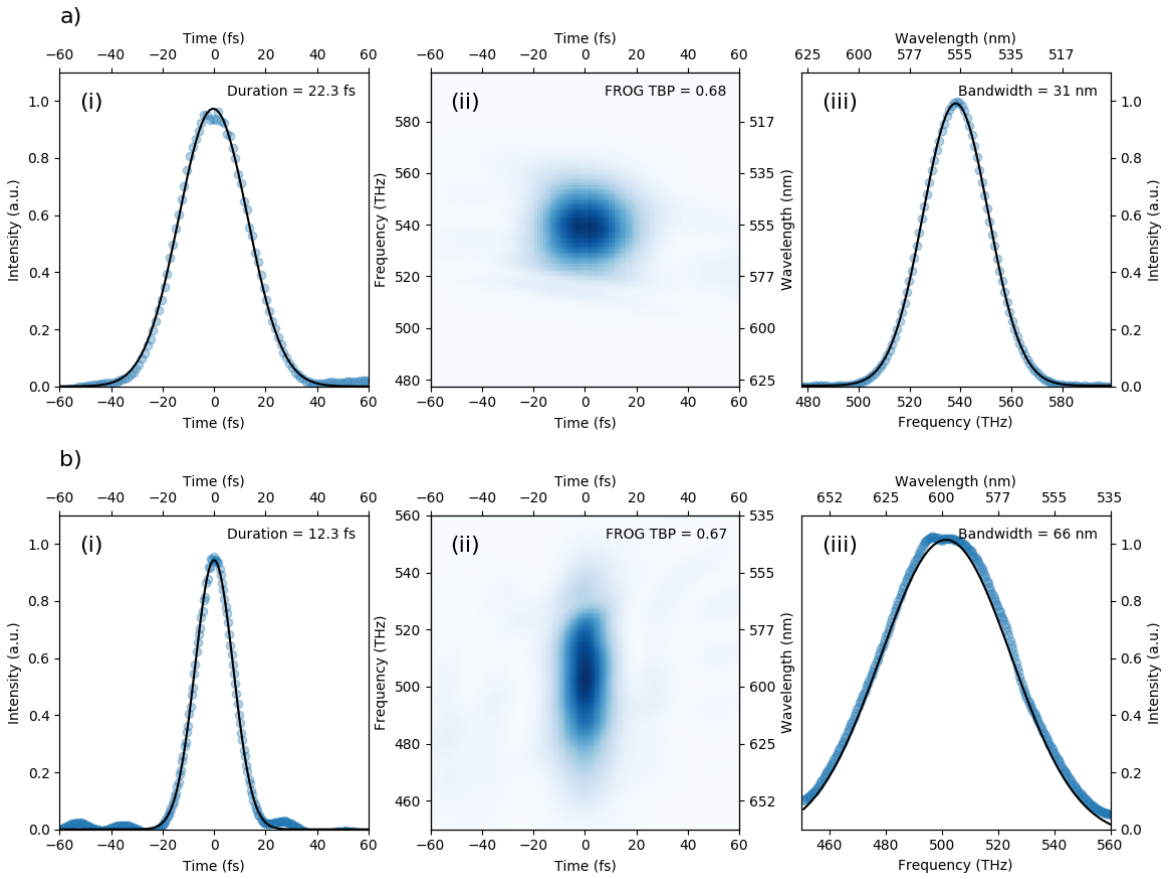

Figure 2.2: FROG traces for the (a) high and (b) low photon energy pulses. Black solid lines are Gaussian fits to the data. Full-width-at-half-maximum duration and bandwidth are given in the upper right corner of (i) and (iii). The time-bandwidth product (TBP) given in the upper right corner of (ii) indicates how the pulse duration and bandwidth compare to that of an ideal transform-limited pulse (0.441 for Gaussian pulses).

2.4.1 Removal of Systematic Error from Ambient Temperature Fluctuation

It was found that a major source of error in the 2DES data was fluctuations in ambient temperature caused by the air-conditioning system. Installation of temperature sensors revealed that that when undisturbed the ambient temperature fluctuation was on the order of 0.8 °C per hour (Figure 2.3). The period of oscillation varied somewhat depending on the external weather conditions. This slow variation in temperature manifested as slight oscillations in the intensity and spectral shape of the laser pulses used in the spectrometer. Figure 2.4a plots the variation of the LO as a function of acquisition time, where data were collected sequentially along the T axis. As it took approximately 10 minutes to collect data for one T point, a temperature oscillation with a period of approximately an hour translated to an experimental oscillation with period on the order of 50 fs, depending on the T-step of the scan. The example chosen in Figure 2.4a is a particularly obvious case of high sensitivity to temperature fluctuations for 2DES data collected using high photon energy pulses, where the pulses were found to be particularly sensitive to temperature fluctuations. However, even subtle LO fluctuations were found to have an impact on the 2DES data.

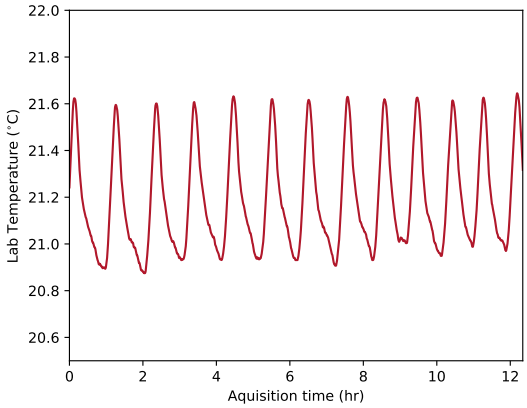

Figure 2.3: A representative trace of the ambient temperature over a 12 hr period.

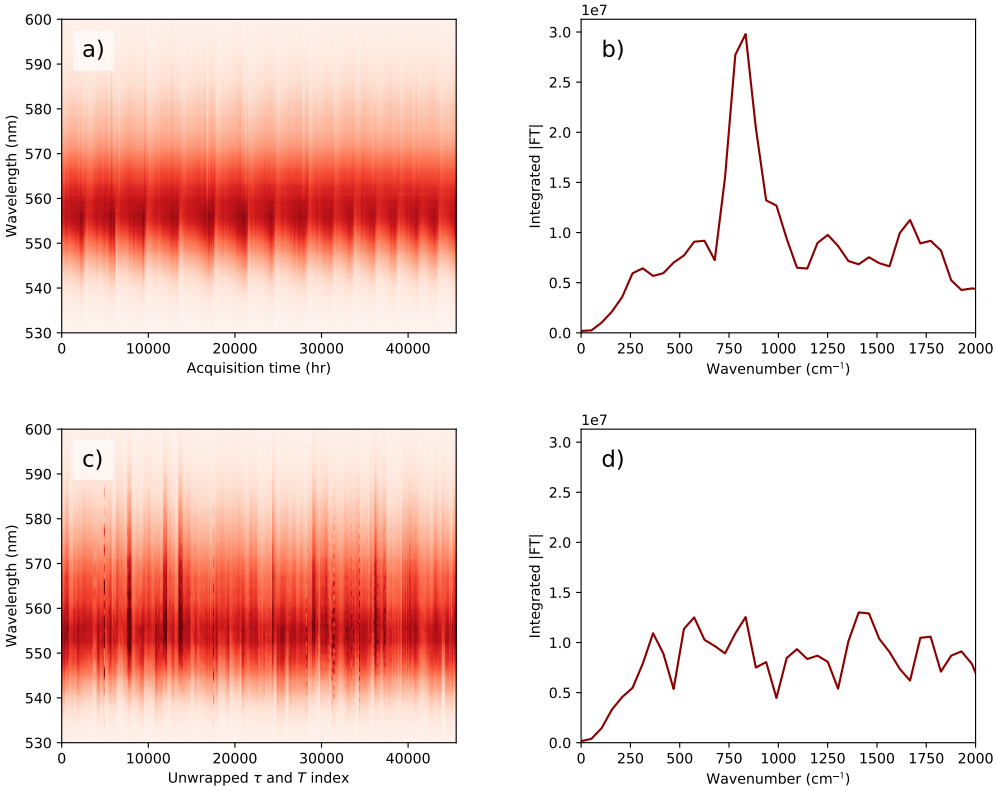

Figure 2.4: (a) LO as a function of 2DES acquisition time, for a sequentially collected T-axis. (b) FT along the T axis of the LO in (a), integrated over the remaining two axes. (c) LO as a function of unwrapped τ and T indices for data collected in a random order along the T axis. (d) FT along the T axis of the LO in (b), integrated over the remaining two axes. In (b) and (d) a Butterworth 8th order, $200\,\mathrm{cm}^{-1}$ highpass filter and Hann windowing was applied before taking the FT.

The frequency of the introduced oscillation can be identified by FT of the LO along the T axis, followed by integration over the other two axes. The introduced signal in Figure 2.4a appears around $800\,\mathrm{cm}^{-1}$, as shown in Figure 2.4b. This frequency matches the frequency of anomalous oscillations observed in the 2DES data. These oscillations are present across the entire ω_1, ω_3 map in a manner that reflects the amplitude of the 2DES signal. This systematic error can be identified but not easily removed once the

data have been collected. However, this systematic error can be effectively removed by randomising the order in which 2DES data are collected over T. Using this method, the oscillating signal is removed from the LO and the 2DES data, accompanied by a slight increase in the noise floor. Figure 2.4c shows the LO intensity for an acquisition where the dataset was collected randomly along the T axis, unwrapped along the τ and T axes such that it is analogous to Figure 2.4a. The integrated FT of this LO contains no anomalous frequencies (Figure 2.3d). This randomisation method was effective in removing the anomalous frequencies from the 2DES data and reduced the impact of ambient temperature fluctuation. In cases where the noise floor was significantly increased, multiple scans were collected and averaged to improve data quality.

2.5 Broadband Pump-probe Spectroscopy

By blocking $\boldsymbol{k}_1$ and $\boldsymbol{k}_3$, the 2D electronic spectrometer was converted to a broadband PP spectrometer, using $\boldsymbol{k}_2$ as the pump, the LO as the probe and a single pair of ROFs as the pump-probe delay line. PP spectroscopy did not have access to the fully resolved excitation energy axis, but removing this axis significantly reduced the data acquisition time, allowing a greater degree of averaging and often higher quality data compared to the full 2DES experiment. Additionally, the PP experiment using a 2D electronic spectrometer retained other key strengths of 2DES, particularly the broadband excitation pulse and the high time resolution. PP was performed as a standalone experiment, and was also required to correctly phase the 2DES data.[19] For these reasons PP experiments are used alongside 2DES in this thesis. As with 2DES, Savitzky-Golay filters along the waiting time and detection wavelength axes were used to reduce the effect of scattering and experimental noise.

CHAPTER 3
Analysis of a Model System using a Flexible Data Analysis Framework

In this chapter, cresyl violet is investigated as a model two-level system with a single vibrational mode. We analyse 2DES data for cresyl violet using a framework that moves from model-independent to model-dependent techniques. In the case of 2DES data containing coherence, preliminary analysis can be done using FTs. If required, dephasing lifetimes can then be estimated using TFTs. Further, the frequencies and lifetimes obtained by FTs and TFTs can be used to create a suitable model for global analysis. Such a model can be created with components to fit both the kinetics and coherence of the system simultaneously. Successful global analysis will then give the most complete and physically reasonable description of the system, returning kinetic rate constants and concentrations, species-associated spectra (SAS) or DAS, coherence frequencies and lifetimes, and amplitude and phase CAS. The advantages of using these techniques in this sequence are that: a) progressively more information is obtained with each new technique, and b) the model-dependent results from the global analysis can be verified against the model-independent results from FTs and TFTs. This framework is used to fully describe the frequency, dephasing rate, amplitude and phase of the cresyl violet coherence. The coherence of cresyl violet is found to be dominated by a single mode at $612\,\mathrm{cm}^{-1}$ with a decoherence lifetime of 600 fs. The amplitude and phase CAS of this coherence is found to agree well with theoretical predictions based on a two-level system with a single vibrational mode in both ground and excited states. Additionally, rapid relaxation processes attributed to dynamic Stokes shift and spectral diffusion were observed, with a rate constant of approximately $1/k = 100\,\mathrm{fs}$.

3.1 Steady-state Characterisation of Cresyl Violet

Cresyl violet (Figure 3.1b) is a typical organic dye molecule, commonly used as a tissue stain[83] and laser dye.[84,85] In an ethanol solution, it displays a strong visible absorption band with a maximum absorbance of 600 nm (Figure 3.1a). Under excitation at 550 nm, it then emits at 620 nm (Figure 3.1a). It has been studied by 2DES previously,[19,86–91] both as a model chromophore for the validation of new experimental designs and in the context of understanding the photophysics of the dye itself. It is known to display strong vibrational coherence due to a ring mode at 590 cm^{-1},[92] and has been observed to undergo rapid relaxation processes associated with spectral diffusion and dynamic Stokes shift.[91] Hence, cresyl violet is a good candidate for demonstration of the proposed 2DES data analysis framework.

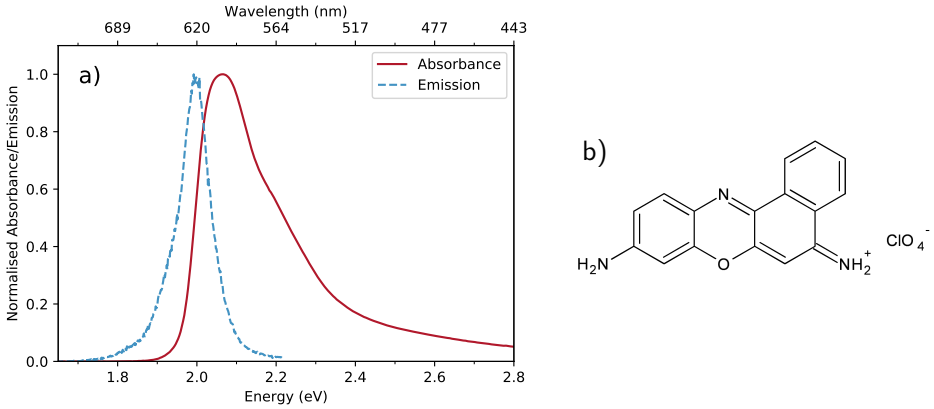

Figure 3.1: (a) Normalised steady-state absorption and fluorescence of cresyl violet perchlorate in ethanol. (b) Structure of cresyl violet perchlorate.

3.2 2DES of Cresyl Violet

2DES data were collected for a solution of cresyl violet in ethanol, using the 12–fs low photon energy pulses characterised in the Methods, Section 2.4. We begin by assigning the main signals observed in the absorptive 2DES data. A representative slice at $T = 110$ fs is shown in Figure 3.2b. There is a broad positive signal along the line at $\omega_1 = 2.07$ eV. This ω_1 value results from the broad absorption of the dye and the shape of the laser pulse. Along the ω_3 axis, the signal intensity is broad and covers a range from 1.95 eV to 2.15 eV. This broad signal arises from the strong overlap between GSB and SE, where the GSB is expected to resemble the broad absorption band from 2.00 eV to 2.20 eV and SE is expected at lower ω_3 around 1.97 eV to 2.00 eV. Taking a T-slice at high, intermediate, and low ω_3 (Figure 3.2c) shows that the data contain strong long-lived coherence, particularly at intermediate and low ω_3.

In addition to the strong coherence, the T-traces in Figure 3.2c also show ultrafast kinetic behaviour. Over the first 100 fs the signal amplitude increases in the lower ω_3 region; this appears to be correlated with a ultrafast decay in the high and intermediate ω_3 region. Over the same time scale there is a distinct shape change in the absorptive map. At early times (25 fs, Figure 3.2a) the signal is diagonal at an energy around the absorption maximum, and is elongated along the diagonal. As T increases, this elongated diagonal peak rapidly transitions to a symmetric ellipsoid, with increased

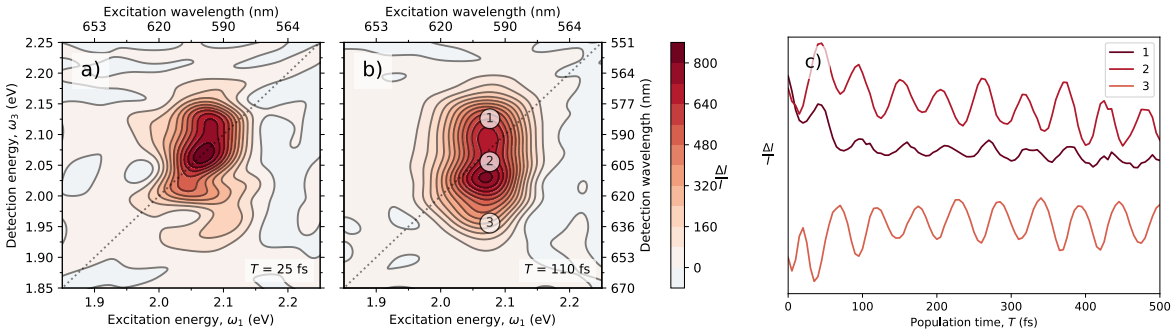

Figure 3.2: Representative absorptive 2DES slice for cresyl violet in ethanol at (a) $T = 25\,\text{fs}$ and (b) $T = 110\,\text{fs}$. (c) T-slice of the absorptive 2DES data at the three signals numbered 1–3 in (b). Points 1–3 have energy coordinates (in eV) $(\omega_1, \omega_3) = (2.07, 2.12)$, (2.07, 2.05), and (2.07, 1.95), respectively. In (c), traces have been vertically offset for clarity.

intensity at lower ω_3, where the steady-state fluorescence is observed (Figure 3.2b). These rapid changes in shape can be explained by two relaxation processes.

Since cresyl violet has a ns-scale excited-state lifetime,[88] any kinetics observed in the first 500 fs following excitation are likely to be due to the faster relaxation processes that occur prior to fluorescence, as fluorescence is orders of magnitude slower than the T window observed here. We observe two key shape changes within the first 100 fs following excitation: a transition from a diagonally elongated peak shape to a symmetric peak shape, and a downward elongation that increases the intensity at lower ω_3. The first type of shape change is commonly observed in 2DES data and often analysed using centre line slope techniques, a method which has been well described by Šanda et al.[77] The origin of this phenomenon is spectral diffusion: the slight differences in transition energy between molecules due to environmental factors such as interactions with the solvent. At early times after excitation, the molecule has very little time to relax, so ω_3 is highly correlated with ω_1, resulting in the diagonally elongated peak shape. As T progresses, the molecule relaxes and samples multiple environment configurations, and ω_1 and ω_3 become increasingly decorrelated until a circular peak shape is observed. The second shape change, where the signal increases at lower ω_3, is attributed to the dynamic Stokes shift.[93] Stokes shift is often observed in SE signals, where ω_3 is lower than ω_1 due to rapid vibrational relaxation and solvent reorganisation following excitation. However, at early times this relaxation process is incomplete, and hence we observe a dynamic Stokes shift where the energy of SE signal decreases over T, progressing from the steady-state absorption maximum to the steady-state fluorescence maximum. These rapid relaxation processes will be investigated in more detail using kinetic modelling later in the discussion.

3.2.1 Fourier Transforms

We begin analysis of the data by considering the strong coherence observed in Figure 3.2c, beginning with FT along the T-axis, as described in the Introduction, Section 1.2.3. Although 2DES data are typically presented as absorptive ($\text{Re}\{R + NR\}$), the complete R and NR 2DES data are complex, containing both real and imaginary components. For the generation of beating maps by FT, the R and NR data are kept in their complex form to produce double-sided FTs. The coherence in the cresyl violet data is dominated by a single mode around $600\,\text{cm}^{-1}$. The beating maps for this

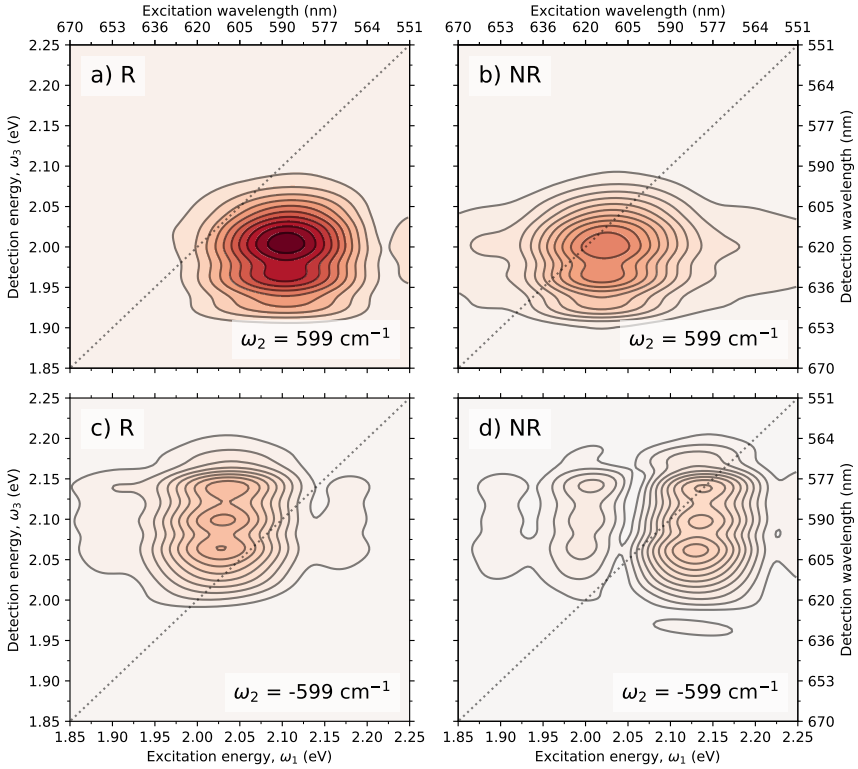

Figure 3.3: Beating maps at $\omega_2 = \pm 599\,\mathrm{cm}^{-1}$ generated from FT of 2DES data of cresyl violet, separated into (a) positive R, (b) positive NR, (c) negative R, and (d) negative NR components. Removal of data before $T = 60\,\mathrm{fs}$, a Butterworth 8th order, $200\,\mathrm{cm}^{-1}$ highpass filter, Hann windowing and zero padding to $n = 512$ were applied before taking the FT. Colour scale corresponds to $|FT|$.

mode are given in Figure 3.3. At this point, preliminary assignment of coherence could be undertaken using double-sided Feynman diagrams as described in Section 1.2.2. However, assignment is simpler and more reliable when the dephasing time and phase maps are known, so we refrain from assigning the coherences fully until the data have been fit to a suitable model using global analysis.

3.2.2 Time-frequency Transforms

To prepare for global analysis, we use TFTs to investigate the lifetime of the coherences. As with FT analysis, during time-frequency analysis it is advisable to leave the data in their original complex form in order to separate positive and negative frequency components. Typically, TFT algorithms are designed for purely real data and although they may tolerate complex data they usually return only a single-sided positive frequency axis. To address this, we split the data into its analytic and antianalytic components prior to the TFT. For a real-valued signal $s(T)$ containing both positive and negative frequencies, the analytic component $s_\mathrm{a}(T)$ contains only the positive frequencies and the antianalytic component $s_\mathrm{aa}(T)$ contains the negative frequencies.[94] The analytic component $s_\mathrm{a}(T)$ can be found using the Hilbert transform $H(s)(T) = \hat{s}(T)$ (equation 3.1 and 3.2).

$$\hat{s}(T) = \frac{1}{\pi} \int_{-\infty}^{\infty} \frac{s(T')}{T - T'}\, dT' \tag{3.1}$$

$$s_\mathrm{a}(T) = s(T) + i\hat{s}(T) \tag{3.2}$$

Since $s(T)$ can be written $s(T) = \frac{1}{2}(s_{\mathrm{a}}(T) + s_{\mathrm{aa}}(T))$, the antianalytic component can be found using equation 3.3.

$$s_{\mathrm{aa}}(T) = 2s(T) - s_{\mathrm{a}}(T) \tag{3.3}$$

This procedure can be extended to a complex signal $s(T) = x(T) + iy(T)$ using the analytic and antianalytic components of $x(T)$ and $y(T)$ to generate the complex Hilbert-transformed signal $\hat{s}(T) = \hat{x}(T) + i\hat{y}(T)$. Once $s_{\mathrm{a}}(T)$ and $s_{\mathrm{aa}}(T)$ have been generated, the TFT can be applied to each separately and then combined, noting that $s_{\mathrm{aa}}(T)$ will have a negative frequency axis.

The method described above is used to generate double-sided SPWVTs at points selected based on the beating maps (Figure 3.3) to show strong coherence at $\pm 600\,\mathrm{cm}^{-1}$. As shown in Figure 3.4, this mode is long-lived, with a near-constant amplitude over the entire available T window, regardless of sign. This example also emphasises some

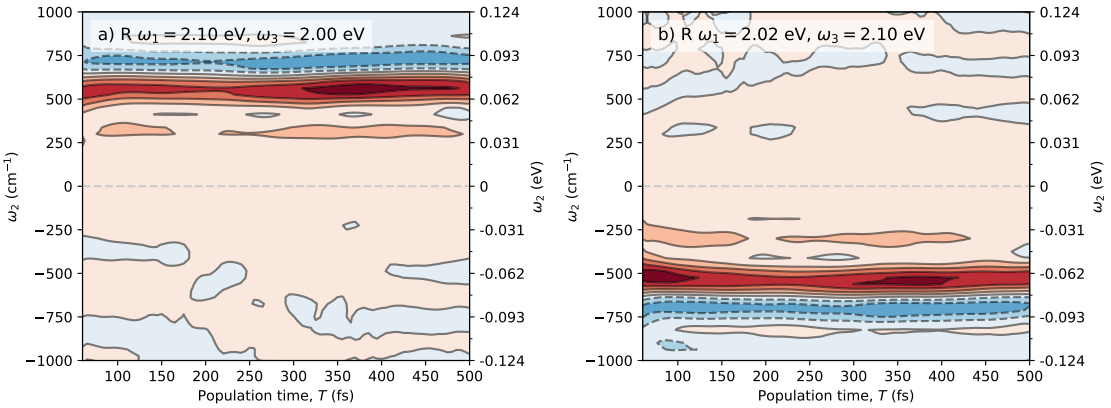

Figure 3.4: SPWVT of total (R + NR) T slices of 2DES data of cresyl violet at (a) $\omega_1 = 2.10\,\mathrm{eV}$, $\omega_3 = 2.00\,\mathrm{eV}$, and (b) $\omega_1 = 2.02\,\mathrm{eV}$, $\omega_3 = 2.10\,\mathrm{eV}$. These points correspond to the locations of strong positive and negative $600\,\mathrm{cm}^{-1}$ coherence, as identified by the beating maps (Figure 3.3). Positive signal is indicated by red in the colour scheme, while negative signal is indicated by blue and is known to be an artefact of the SPWVT. The SPWVT used Gaussian windows along the T and wavenumber axes, with $\sigma = 100\,\mathrm{fs}$ for both. Data from $T = 60\,\mathrm{fs}$ onwards was used and a Butterworth 8th order, $200\,\mathrm{cm}^{-1}$ highpass filter was applied prior to taking the SPWVT.

of the risks associated with TFTs: the frequency and T resolution are poor due to the limited T range, and the SPWVT produces negative artefacts (in blue in Figure 3.4) that can be difficult to remove. In this case the information gained from the TFT is limited, however TFTs can be more powerful for data collected from 2D electronic spectrometers that are able to collect data over longer T ranges.

3.2.3 Global Analysis

We start global analysis by considering the kinetics of the system, beginning with a multi-exponential model of the type described in the Introduction, Section 1.2.5.1. Two exponential components were required to adequately describe the kinetics of the system. The first component was fitted to a short lifetime of $(72 \pm 2)\,\mathrm{fs}$ and the second component to a long ps-scale lifetime. The model was used to fit the data from $T = 30\,\mathrm{fs}$ onwards to minimise the effect of early-time coherent artefacts. The absorptive DAS

of these two components are shown in Figures 3.5a and b. Selected T-traces are shown in Figure 3.5c. These results show that the bi-exponential model captures the general kinetic behaviour of the system, but the quality of the fit is difficult to determine given the large amplitude of the coherence.

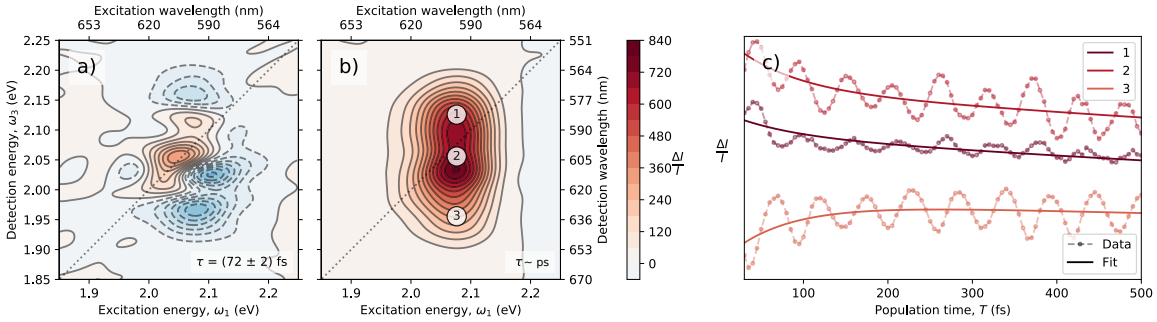

Figure 3.5: (a)–(b) Absorptive DAS of the two multi-exponential components resulting from global analysis of 2DES data of cresyl violet, with exponential lifetimes τ_n in the lower right corner. Colour scale corresponds to $\Delta I/I$. (c) Selected T-traces of the experimental data and model. Legend corresponds to peaks marked in (b). Points 1–3 have energy coordinates (in eV) $(\omega_1, \omega_3) = (2.07, 2.12)$, $(2.07, 2.05)$, and $(2.07, 1.95)$, respectively. In (c), traces have been vertically offset for clarity.

Multi-exponential models are a typical starting point in kinetic analysis, however there are a number of reasons to move on to a more sophisticated model. The DAS in Figures 3.5a and b are unlikely to have reliable physical meaning since the parallel bi-exponential model is unlikely to reflect the true kinetics of the rapid shape changes observed in this data set. In this case a strong indicator of unphysical DAS is the negative signals in Figure 3.5a, as cresyl violet is known to have no ESA in this energy region.[19,86–91] These negative signals appear because the fitting routine is attempting to account for the increase in intensity over time in the low ω_3 region. Additionally, the model excludes coherence, which may introduce error in the fitted lifetimes. This example illustrates the difficulty of attempting to fit the kinetic behaviour of a system with strong coherence without accounting for such coherence in the model.

3.2.4 Global Target Analysis

To introduce physically meaningful kinetics, we extend the algorithm reported by Volpato et al.[25] to fit to general kinetic models, making use of a matrix formalism to automate the formation of a system of ordinary differential equations (ODEs) from a series of general kinetic equations of the form $\sum_n c_n A_n \rightarrow \sum_n d_n A_n$.[95,96] For a system containing N species and M equations, the system can be described as

$$\sum_n^N c_{mn} A_n \rightarrow \sum_n^N d_{mn} A_n \qquad \text{for } m = 1, ..., M \tag{3.4}$$

where c_{mn} and d_{mn} are the stoichiometric coefficients on the reactants and products side respectively, for species A_n in the mth equation. The stoichiometric coefficients for the reactant and product sides of the system of equations (equation 3.4) are used to create matrices $\mathbf{X_r}$ and $\mathbf{X_p}$ (equations 3.5 and 3.6). For example, $X_{\mathrm{r},mn}$ is the coefficient of species A_n on the reactants side of the mth equation. $\mathbf{X_r}$ and $\mathbf{X_p}$ have

size $M \times N$.

$$X_{\mathrm{r},mn} = c_{mn} \tag{3.5}$$

$$X_{\mathrm{p},mn} = d_{mn} \tag{3.6}$$

We then define a vector of rate constants for each reaction $\boldsymbol{k} = [k_1, ..., k_M]$, and a vector of initial relative concentrations for each species $\boldsymbol{C} = [C_1, ..., C_N]$. The system of ODEs (equation 3.7) is now generated using these two vectors and the matrix $\mathbf{X} = \mathbf{X_p} - \mathbf{X_r}$. $c_n(T)$ is the concentration of species n as a function of T, and $c'_n(T)$ is the rate of change in concentration.

$$c'_n(T) = \sum_m^M X_{mn} v_m \tag{3.7}$$

$$v_m = k_m \prod_n^N c_n^{X_{\mathrm{r},mn}} \tag{3.8}$$

This system of ODEs can be solved using a numerical ODE solver for a given $\boldsymbol{k}$ and $\boldsymbol{C}$. The model matrix $\mathbf{M} = \mathbf{EA}$ can now be constructed from $\mathbf{E}$ and $\mathbf{A}$ in a similar way as for the multi-exponential model described in the Introduction, Section 1.2.5.1, where the nth column of $\mathbf{E}$ is given by $c_n(T)$ and the elements of $\mathbf{A}$ are the amplitudes of each of the n components as a function of ω_1 and ω_3. The minimisation routine proceeds as described in Section 1.2.5, and the outputs of such a model are the optimised rate constants $\boldsymbol{k}$, initial relative concentrations $\boldsymbol{C}$, and SAS derived from matrix $\mathbf{A}$ using the same method as for DAS in Section 1.2.5.1. Provided that the kinetic model is physically reasonable, the SAS are likely to directly correspond to real species or states of the system. As these models can contain a large amount of flexibility, care should be taken that the best-fit $\boldsymbol{k}$, $\boldsymbol{C}$ and SAS are physically reasonable and if possible the initial values of $\boldsymbol{k}$ and $\boldsymbol{C}$ should be constrained based on known properties of the system, such as excited-state lifetimes.

A general kinetic model of the type described above is combined with complex multi-exponential components to create a hybrid model, where the kinetics of the system are described by a general kinetic model and the coherence is described by a complex multi-exponential model. For the cresyl violet data, the coherence is described by a pair of complex exponential components with equal lifetimes and initial frequencies of $\pm 600\,\mathrm{cm}^{-1}$, chosen to match the coherence observed in the beating maps (Figure 3.3). For the kinetics we use a simple scheme designed to capture the rapid shape change observed in the data, given by equation 3.9.

$$\mathrm{A} \xrightarrow{k_1} \mathrm{B} \tag{3.9}$$

In this kinetic scheme, A represents cresyl violet at early times, where ω_1 and ω_3 are strongly correlated, and B represents cresyl violet after relaxation, when ω_1 and ω_3 are decorrelated and energy of the SE signal has decreased to match the steady-state fluorescence. The matrices $\mathbf{X_r}$, $\mathbf{X_p}$ and $\mathbf{X}$ for this kinetic model are given by equation 3.10. The vector of initial relative concentrations is fixed to $\boldsymbol{C} = [C_\mathrm{A}, C_\mathrm{B}] = [1, 0]$.

$$\mathbf{X_r} = \begin{pmatrix} 1 & 0 \end{pmatrix} \qquad \mathbf{X_p} = \begin{pmatrix} 0 & 1 \end{pmatrix} \qquad \mathbf{X} = \mathbf{X_p} - \mathbf{X_r} = \begin{pmatrix} -1 & 1 \end{pmatrix} \tag{3.10}$$

This system of equations is used to generate the system of ODEs (equations 3.11 and 3.12), which is then solved numerically to generate the concentration curves $c_\mathrm{A}(T)$ and

$c_{\mathrm{B}}(T)$.

$$c'_{\mathrm{A}} = -k_1 c_{\mathrm{A}} \tag{3.11}$$

$$c'_{\mathrm{B}} = k_1 c_{\mathrm{A}} \tag{3.12}$$

In this case the kinetic model used is very simple and the system of ODEs is easily generated without the matrix formalism described above. However, this formalism allows the same fitting routine to be used for arbitrarily large and complex kinetic schemes.

These concentration curves are concatenated with the two coherence components and fit to the 2DES data for cresyl violet from $T = 25\,\mathrm{fs}$ onwards. The agreement between the experimental data and the model is improved compared to the multi-exponential fit (Figure 3.5c), as shown by the selected T-traces in Figure 3.6c. The

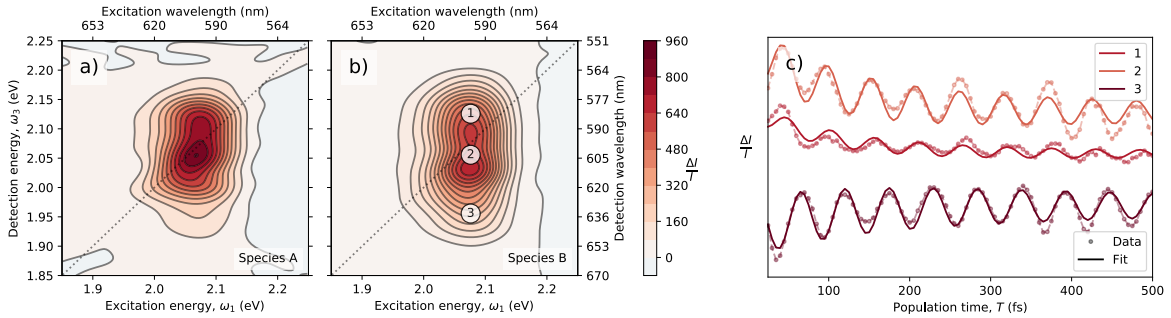

Figure 3.6: (a)–(b) Absorptive SAS resulting from global fitting of a kinetic model with complex multi-exponential components to 2DES data of cresyl violet. (c) Selected absorptive T-traces of experimental data compared to the model. Legend corresponds to peaks labelled in (b). Points 1–3 have energy coordinates (in eV) $(\omega_1, \omega_3) = (2.07, 2.12)$, (2.07, 2.05), and (2.07, 1.95), respectively. In (c), traces have been vertically offset for clarity.

fitted rate constant is $k_1 = (0.010 \pm 0.003)\,\mathrm{fs}^{-1}$, corresponding to a decay time constant of $\tau_1 \approx 100\,\mathrm{fs}$. The two SAS are shown in Figures 3.6a and b. The shape of the two SAS are consistent with the prior discussion; the species A SAS displays elongation along the diagonal and a lack of intensity at lower ω_3, while the species B SAS has no diagonal elongation and higher intensity at lower ω_3, indicating complete Stokes shift and decorrelated ω_1 and ω_3. The relaxation rate of around 100 fs agrees with a recent study of the dynamic Stokes shift in cresyl violet, which found that the time constant for dynamic Stokes shift varies from 36 fs to 98 fs, depending on ω_1.[91] We emphasise that in this simple kinetic scheme two relaxation processes are accounted for by a single rate constant, whereas in reality the two processes may not necessarily have the same rate constant. It may be possible to disentangle the rate constants of the two relaxation processes using a more complex kinetic scheme.

The oscillating components were fitted to frequencies of $(\pm 611.5 \pm 0.2)\,\mathrm{cm}^{-1}$ with dephasing lifetimes of $(600 \pm 100)\,\mathrm{fs}$. This long lifetime is consistent with vibrational or vibronic coherence, and the high uncertainty is expected due to the relatively short T range available to this instrument. A longer T axis would be required to characterise the dephasing rate with higher accuracy. The frequency is approximately consistent with that of the previously observed Raman mode of cresyl violet at $591\,\mathrm{cm}^{-1}$.[92] Amplitude and phase CAS for the coherence components are shown in Figures 3.7a–h.

Comparing Figures 3.3 and 3.7, it is evident that the amplitude CAS are nearly identical to the beating maps generated from FTs. However, global analysis provides

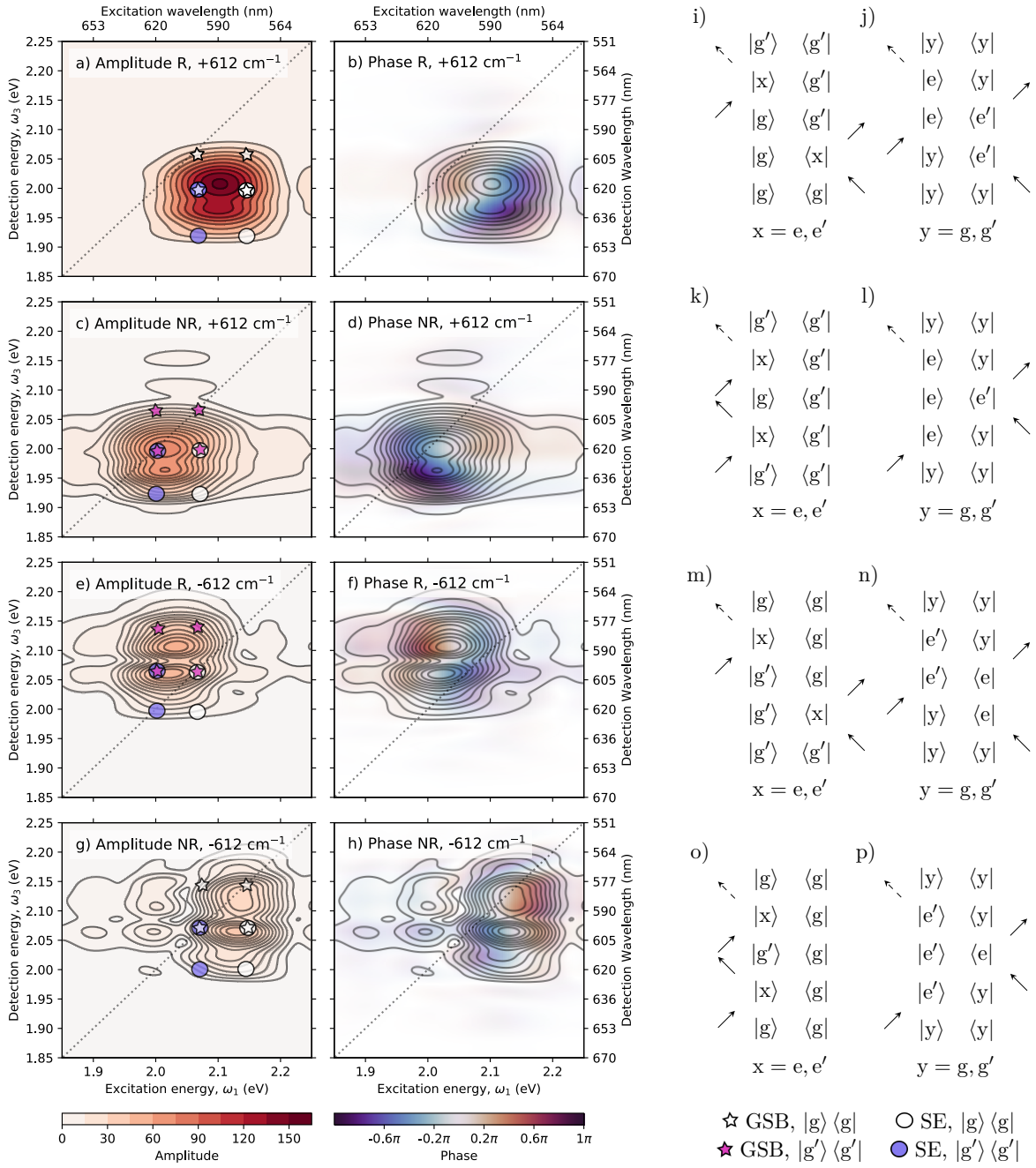

Figure 3.7: (a)–(h) Amplitude and phase CAS generated from global fitting of a hybrid kinetic/complex multi-exponential model to the 2DES data for cresyl violet. CAS are split into R and NR components and by sign of frequency as indicated by the legends in the top left. Predicted coherence locations based on a simple theoretical model are marked on the amplitude CAS, with stars representing GSB pathways and circles representing SE pathways. Pathways that start in the ground state are coloured white, while those that start in the vibrationally-excited ground state are coloured pink/purple (GSB/SE). (i)–(p) Double-sided Feynman diagrams for the GSB and SE pathways marked on the amplitude CAS. $|g\rangle$ and $|e\rangle$ represent the ground and excited electronic states respectively, while primed states represent vibrational excitation of the 612 cm^{-1} (0.076 eV) mode.

additional information in the form of the phase CAS and the dephasing rate. In Figure 3.7, the CAS are compared to the predicted coherence locations based on a simple model, where the $612\,\mathrm{cm}^{-1}$ mode is assumed to be present in both the ground and excited states, with a similar frequency in both manifolds. This assumption is supported by previous work on this system[87,97] and by the fact that the lower ω_3 edge of each peak in the CAS cannot be explained without including these SE pathways. The transition energy is taken to be the maximum absorbance at 2.066 eV, and SE is assumed to occur following relaxation by 0.07 eV, corresponding to the observed Stokes shift. The ω_1- and ω_3-dependence of the CAS is in good agreement with the locations predicted by double-sided Feynman diagrams. The diagrams predict a characteristic pattern of 4 signals arranged in a square formation for both SE and GSB pathways.[27] For a single map, the predicted SE coherence has the same ω_1 as the GSB coherence, but the ω_3 is lowered by energy corresponding to the Stokes shift. In this example, the Stokes shift is coincidentally very similar in energy to the $612\,\mathrm{cm}^{-1}$ (0.076 eV) vibrational mode, resulting in the overlap between GSB and SE pathways seen in Figure 3.7. As the Stokes shift occurs over a finite time, we expect that the SE pathways shift from $\omega_3 = 2.066\,\mathrm{eV}$ to $\omega_3 = 1.99\,\mathrm{eV}$ as T progresses, blurring the SE coherence signal along the ω_3 axis. The phase CAS are complex, with each signal showing large phase evolution across the peaks. The phase evolution also occurs in different directions in the R and NR maps. In the two R phase CAS, the phase decreases from the upper left to the lower right of the peak, with lines of approximately equal phase running along the diagonal of the peak. Conversely, in the two NR phase CAS the phase decreases from the upper right to the lower left of the peak, with lines of approximately equal phase along the anti-diagonal. This behaviour has been predicted theoretically for a vibronic coherence from a model displaced oscillator system.[31]

In general, the intensity of a coherence pathway is influenced by all four interactions involved,[27] and hence predicting the relative intensity of coherence pathways is somewhat complicated. However, pathways that require the system to start in the lowest-energy ground state $|\mathrm{g}\rangle$ (white symbols) are generally stronger than those that start in an excited ground state level $|\mathrm{g}'\rangle$ (pink/purple symbols), especially for high frequency vibrational modes. This behaviour is reflected in the amplitude CAS, where the positive NR coherence has a higher contribution from pathways starting in $|\mathrm{g}'\rangle$, and is hence less intense than the positive R CAS, which arises predominantly from pathways starting in $|\mathrm{g}\rangle$. The negative NR map contains contributions from pathways starting in $|\mathrm{g}\rangle$, however it has an unexpectedly low amplitude. This can be explained by its location at the high-energy limit of the excitation spectrum, where there is minimal excitation intensity available to probe these coherence pathways.

The cresyl violet example illustrates the complexity inherent in analysing 2DES data. The data obtained from this system are rich and complex and require sophisticated global analysis algorithms to describe fully, even though the two-level, single-mode system is one of the simplest possible systems that can display significant coherence. This work demonstrates the importance of using reliable and well-understood analytical techniques to reach meaningful conclusions.

3.3 Conclusions

In this chapter, a scaffold of techniques for the analysis of 2DES data were presented and used to analyse 2DES data for cresyl violet, a model system with a single vibrational

mode. First, the absorptive 2DES data were assigned, supported by the steady-state absorption and emission of the system. The use of FTs to create beating maps was then presented. It was recommended that the R and NR components are separated and the complex form of the data is retained in order to reduce the number of pathways per map. FTs were not found to be the ideal technique for analysis of coherence due to lack of access to dephasing times and phase as well as removal of the kinetic behaviour of the system. TFTs were presented as an additional model-independent technique that can be used to simultaneously investigate the ω_2- and T-dependence of coherence, however for our instrument this technique was found to be severely limited by time-frequency uncertainty. Finally, global analysis algorithms capable of simultaneously fitting the kinetics and coherence of the 2DES data were presented. As far as the author is aware this is the first example of the use of a global analysis algorithm capable of fitting to a kinetic model while incorporating coherence using complex exponentials.

It was found that the kinetics of cresyl violet are dominated by fast relaxation processes associated with spectral diffusion and Stokes shift. These two processes were found to occur on similar timescales and were fit with a single rate constant of approximately $1/k = 100\,\mathrm{fs}$. The coherence is dominated by a single vibronic mode at $612\,\mathrm{cm}^{-1}$, located in both the ground and excited state manifolds, with a dephasing rate of 600 fs. The ω_1- and ω_3-dependence of the coherence was consistent with a simple theoretical model incorporating contributions from both GSB and SE pathways.

CHAPTER 4
Coherence of TIPS-Pn in Solution

In Chapter 3, a variety of methods were used to analyse 2DES data of cresyl violet, a model system. In this Chapter, these methods will now be used to analyse 2DES and broadband PP data from TIPS-Pn in dilute solutions, with particular focus on coherence. In PP data for TIPS-Pn in solutions of THF, toluene, and acetone, coherence is observed originating from both TIPS-Pn and the solvents. To separate the coherence of TIPS-Pn from the solvents, PP data are also presented for samples of the three solvents in the absence of TIPS-Pn. 2DES is then used to further characterise the coherence of THF and TIPS-Pn in THF. It is found that THF exhibits non-resonant coherence around $934\,\mathrm{cm}^{-1}$ with a lifetime of 0.86 ps. This non-resonant coherence is also found to have highly non-trivial ω_1- and ω_3-dependence, which is rationalised by a Raman-like mechanism. In 2DES data for TIPS-Pn in THF, vibrational and vibronic coherence is observed at frequencies of $295\,\mathrm{cm}^{-1}$, $520\,\mathrm{cm}^{-1}$, $781\,\mathrm{cm}^{-1}$, $1159\,\mathrm{cm}^{-1}$ and $1341\,\mathrm{cm}^{-1}$, with dephasing lifetimes from 0.5 ps to 1.5 ps. Where possible, these modes are assigned using double-sided Feynman diagrams. This assignment, combined with the high-quality PP data, indicates that the vibronic structure of the first excited singlet state of TIPS-Pn is similar to the ground state.

4.1 Steady-state Characterisation of TIPS-Pn Solutions

The steady-state UV–visible absorption spectra of TIPS-Pn in toluene, THF and acetone are shown in Figure 4.1. TIPS-Pn has a number of well-understood vibronic transitions in the visible region.[98] The lower energy peaks at 1.93 eV, 2.10 eV and 2.25 eV have been assigned to the transitions from $|S_0\rangle$ to the vibronic manifold of $|S_1\rangle$ (the 0–0, 0–1 and 0–2 transitions, respectively). The low intensity peaks at 2.81 eV and 2.89 eV have been assigned as transitions to $|S_3\rangle$ and $|S_4\rangle$, respectively. We note that the vibronic structure within the $|S_1\rangle$ manifold may be more complex than it first appears, as indicated by the broadening of the 0–1 and 0–2 peaks relative to the 0–0 peak, and noted by Pensack et al.[54] The spectrum is similar for all three solvents, with slight differences in peak position due to solvatochromism, consistent with the findings of Pensack et al. where redshifting is associated with an increase in the aromaticity and polarisability of the solvent.[54]

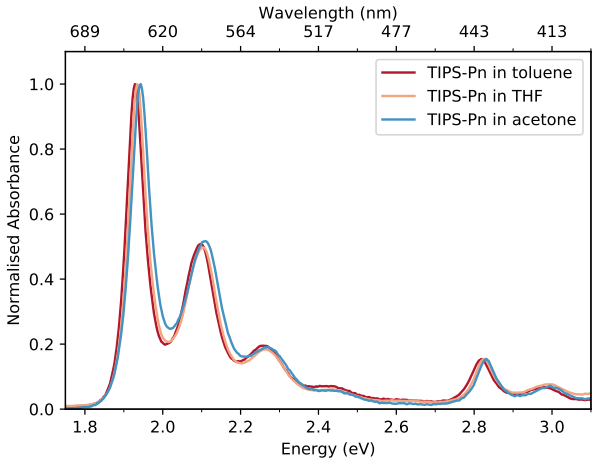

Figure 4.1: Normalised steady-state UV–visible absorption spectra of TIPS-Pn in toluene, THF and acetone.

4.2 Pump-probe of TIPS-Pn in Three Solvents

PP data for TIPS-Pn in toluene, THF and acetone are shown in Figures 4.2a–c. The broad features of these spectra are consistent with previous reports of transient absorption of TIPS-Pn in solution.[49,51] A positive signal is observed at 595 nm, corresponding to bleaching of $|S_{(1,1)}\rangle$. Another positive signal is observed at lower energies corresponding to bleaching of $|S_{(1,0)}\rangle$, however it is overwhelmed by background fluorescence at wavelengths greater than 640 nm, and hence wavelengths above 640 nm are not shown. In addition, there is a strong ESA feature around 575 nm, corresponding to absorption from $|S_1\rangle$ to a higher excited singlet state. The intensity of the GSB and ESA signals is constant over the time window measured, consistent with the previously reported singlet lifetime ($\sim$ 12 ns) of TIPS-Pn.[49,51] The high-amplitude features at waiting times less than 90 fs are considered to be coherent artefacts resulting from pulse overlap and have no physical meaning.

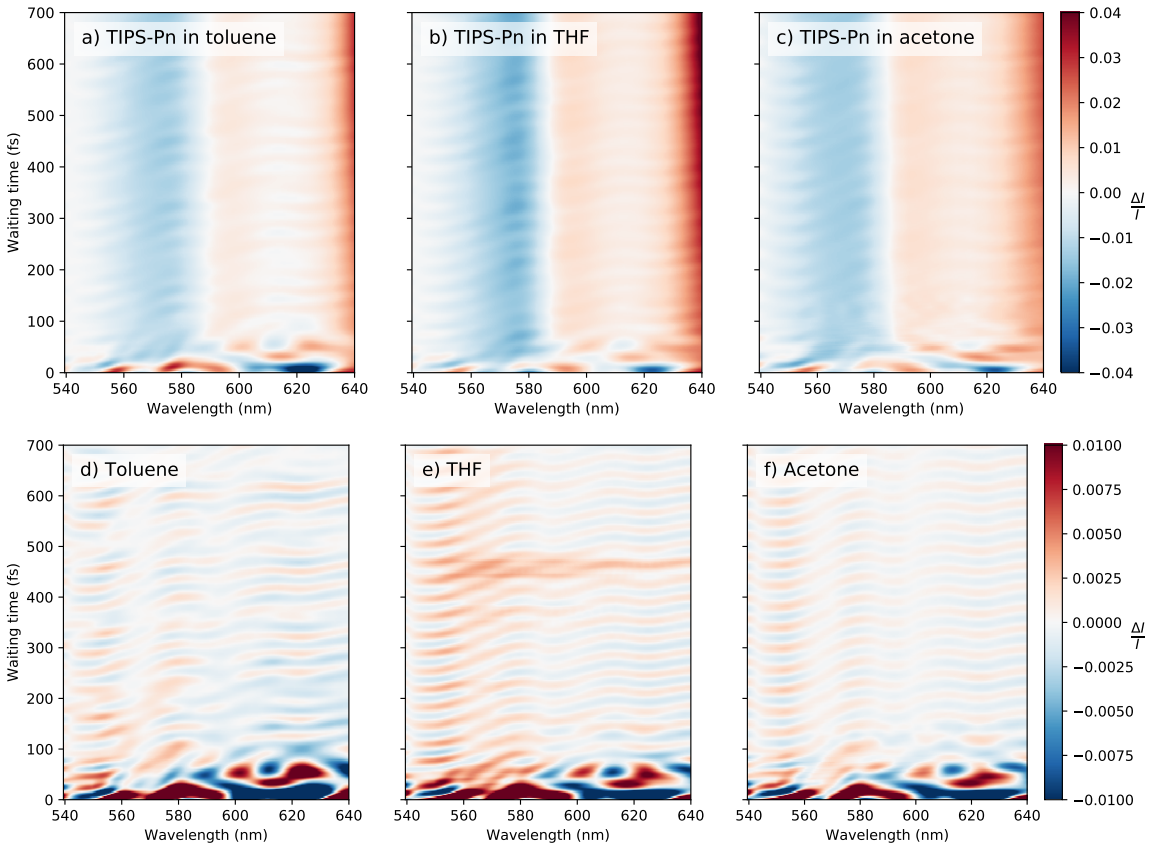

Figure 4.2: PP data for (a) TIPS-Pn in toluene, (b) TIPS-Pn in THF, (c) TIPS-Pn in acetone, (d) toluene, (e) THF, and (f) acetone. Note the change in colour scale for (d)–(f) compared to (a)–(c), indicated by the colour bars to the right of each row of frames.

In all three solvents, the PP data shown for TIPS-Pn in Figures 4.2a–c also contain prominent oscillatory signals across the entire wavelength and waiting time ranges measured. At first, these signals appear similar in all three solvents, however close inspection reveals distinct differences between data sets. In acetone the frequency is comparatively lower than in the other two solvents, while in toluene there is a low-frequency envelope indicative of interference between multiple modes. A FT is applied along the waiting time axis to identify these oscillatory modes (Figures 4.3a–c). In acetone, the strongest oscillation is at $800\,\mathrm{cm}^{-1}$, with weaker signals observed around $1200\,\mathrm{cm}^{-1}$ and $250\,\mathrm{cm}^{-1}$. In THF, the strongest signal is observed around $900\,\mathrm{cm}^{-1}$, with additional signals at $1200\,\mathrm{cm}^{-1}$, $800\,\mathrm{cm}^{-1}$ and $250\,\mathrm{cm}^{-1}$. Finally, in toluene there are two strong signals at $1030\,\mathrm{cm}^{-1}$ and $800\,\mathrm{cm}^{-1}$, with additional signals at $550\,\mathrm{cm}^{-1}$ and $250\,\mathrm{cm}^{-1}$.

Clearly, the most prominent oscillation frequencies have a strong solvent dependence. To identify the origin of these prominent modes, PP data were collected for samples of the three solvents in the absence of TIPS-Pn (Figures 4.3d–f). For samples containing only solvent, the average signal after 100 fs is zero. This result is expected since all the solvents are non-resonant with the laser pulse. However, in all solvents the signal oscillates over the entire wavelength and waiting time range measured. As before, we take the FT along the wavelength axis to reveal the frequency components of these oscillations (Figures 4.3d–f). The Fourier transformed solvent-only PP data shows that the solvent accounts for the strongest oscillatory signals in the PP data

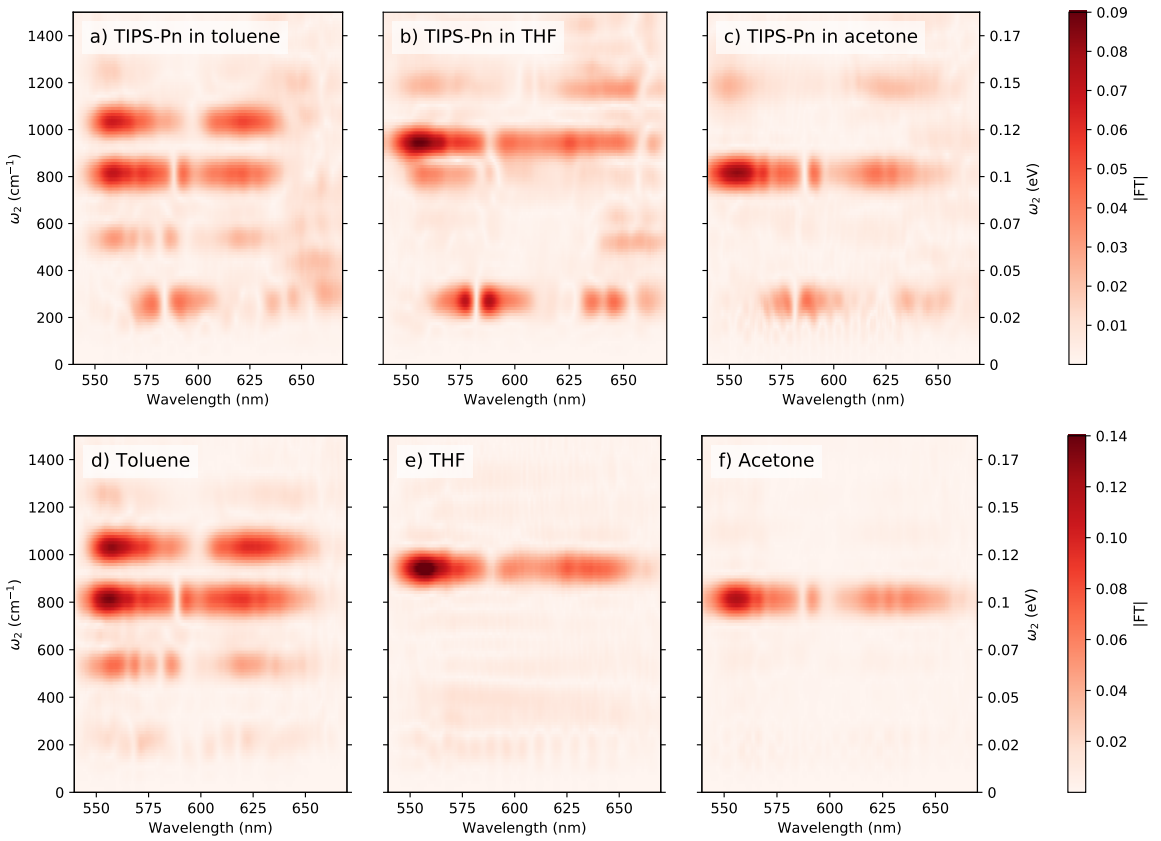

Figure 4.3: Fourier transformed PP data for (a) TIPS-Pn in toluene, (b) TIPS-Pn in THF, (c) TIPS-Pn in acetone, (d) toluene, (e) THF, and (f) acetone. Data before 100 fs was removed due to the presence of coherence artefacts, and the remaining time window was pre-processed by applying a Butterworth 8th order, 200 cm^{-1} highpass filter, Hann windowing and zero padding to $n = 1024$ before taking the FT. Note the change in colour scale for (d)–(f) compared to (a)–(c), indicated by the colour bars to the right of each row of frames.

for TIPS-Pn in solution. The data sets for acetone and THF show a single strong oscillation around 810 cm^{-1} and 930 cm^{-1}, respectively, while in toluene the spectrum is more complex, with relatively strong signals at 1030 cm^{-1} and 810 cm^{-1}, and weaker signals at 1250 cm^{-1}, 560 cm^{-1} and 220 cm^{-1}. The wavelength-dependence of these solvent-associated modes is the same in the presence and absence of TIPS-Pn. The intensity of these solvent modes is slightly lower when TIPS-Pn is present, consistent with preferential absorption of the laser pulses by TIPS-Pn.

Oscillatory signatures resulting from the solvent have been reported in 2DES experiments previously.[25,99–101] These signatures are usually assigned as molecular vibrations of the solvent by matching the anomalous frequencies with the Raman-active modes of the solvent. In the frequency range of interest, the known Raman modes of toluene are 1211 cm^{-1} (weak), 1031 cm^{-1} (weak), 1004 cm^{-1} (strong), 787 cm^{-1} (strong), 522 cm^{-1} (weak) and 218 cm^{-1} (weak).[102] THF and acetone have only a single Raman-active mode at 915 cm^{-1} and 790 cm^{-1}, respectively.[103,104] These frequencies and intensities are summarised in Table 4.1 and are consistent with those in Figures 4.3d–f within our frequency uncertainty, which is quite high due to the low frequency resolution of the FT. Hence, Raman-active modes of the solvent account for a significant amount of the coherences observed in solutions of TIPS-Pn.

Table 4.1: Observed PP coherence frequencies for toluene, THF and acetone, compared to their prominent Raman modes in this frequency region.

Sample	PP freq. (cm^{-1})	Raman freq. (cm^{-1})
Toluene	220	218
	560	522
	810	787
	1030	1004, 1031
	1250	1211
THF	930	915
Acetone	810	790

In the samples containing TIPS-Pn, there remain a number of weaker modes that are unaccounted for by solvent coherences. When not masked by the solvent coherence, these modes are common between multiple solvents, so it is likely that they are associated with TIPS-Pn. Figure 4.4 shows the intensity of the Fourier transformed PP data integrated over the wavelength axis. In all three solvents, a low frequency mode around 250 cm^{-1} is common. For TIPS-Pn in THF, there is a peak at 800 cm^{-1} that is absent in THF alone, however in the other two solvents the strong solvent vibration near this frequency masks this signal. Finally, there are some weak high frequency modes around 1150 cm^{-1} to 1200 cm^{-1} present in both TIPS-Pn in acetone and TIPS-Pn in THF. These four modes are consistent with known Raman-active modes of TIPS-Pn at 265 cm^{-1}, 788 cm^{-1}, 1158 cm^{-1} and 1195 cm^{-1},[28,56] and are hence attributed to molecular vibration of TIPS-Pn.

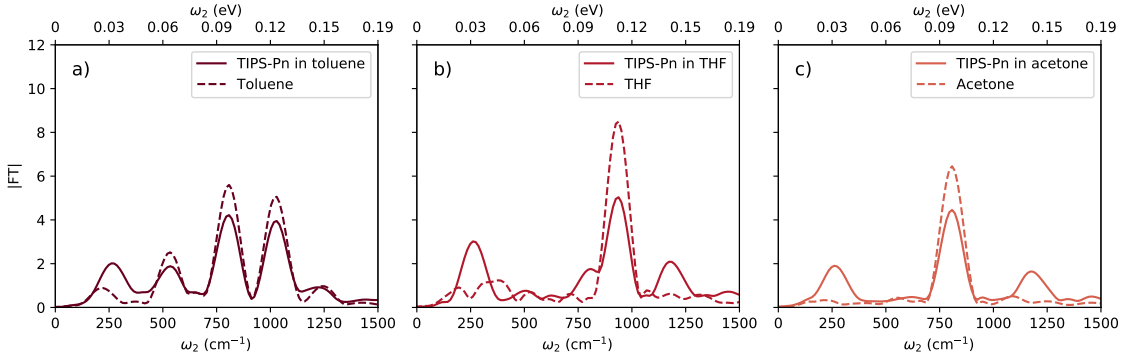

Figure 4.4: Integrated FT of PP data for three solvents, with and without TIPS-Pn. Data pre-processing and filtering were applied as for Figure 4.3.

The observed wavelength-dependence of the solvent- and TIPS-Pn-attributed modes is non-trivial. All observed modes have regions of intensity at both low and high wavelengths, and nodes of zero intensity at intermediate wavelengths. For modes attributed to TIPS-Pn, the appearance of the oscillatory signals in both the ESA and GSB regions (540 nm to 590 nm and 590 nm to 660 nm, respectively) indicates that the vibration is occurring in both the ground and first singlet excited states. For modes attributed to the solvent, it still unclear how a non-resonant interaction should have such a complex and structured wavelength-dependence. To fully understand the origin of the wavelength-dependence of the observed coherence, we use 2DES to probe both the ω_1-

and ω_3-dependence of these signals.

4.3 2DES of THF

Out of the three solvents for TIPS-Pn considered here, the coherence of THF at $915\,\mathrm{cm}^{-1}$ overlaps the least with the observed vibrational modes of TIPS-Pn. Hence, the 2DES study of TIPS-Pn in solution will be focussed on TIPS-Pn in THF solution. As a control study, 2DES data were first collected for a sample of THF without TIPS-Pn. Similarly to the PP data for solvent-only samples, after the first 100 fs the average 2DES absorptive signal is very low as THF is non-resonant with the laser pulses. However, a single oscillatory mode at $912\,\mathrm{cm}^{-1}$ is observed. As for the PP data, this frequency agrees closely with the known Raman mode of THF at $915\,\mathrm{cm}^{-1}$. To further investigate this coherence, the 2DES data are Fourier transformed along the T axis to generate beating maps. These beating maps are shown for the R and NR data at $-912\,\mathrm{cm}^{-1}$ and $+912\,\mathrm{cm}^{-1}$ in Figure 4.5. Interestingly, the ω_1- and ω_3-dependence of the solvent coherence observed in Figure 4.5 is non-trivial. This result is in contrast to previous reports that beating maps associated with solvent coherence tends to be broad and featureless[25] or reflect only the shape of the laser pulse.[99]

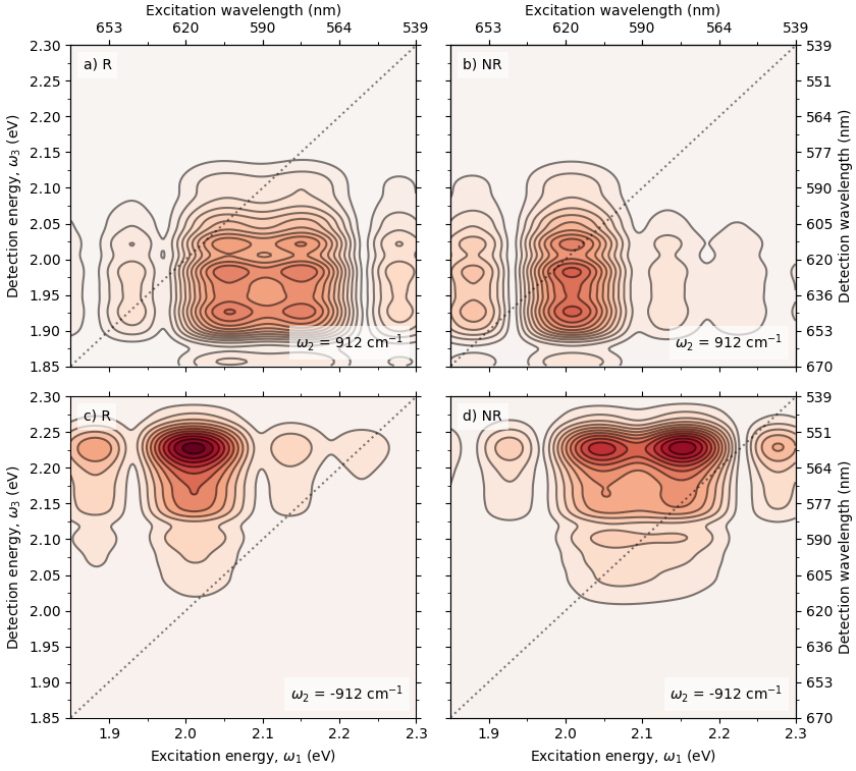

Figure 4.5: Beating maps generated from 2DES data of THF, separated into positive and negative frequency components of the R and NR data. Removal of data before a waiting time of 90 fs, a Butterworth 8th order, $200\,\mathrm{cm}^{-1}$ highpass filter, Hann windowing and zero padding to $n = 512$ were applied before taking the FT. Colour scale corresponds to $|FT|$.

To investigate how this coherence is generated, we draw inspiration from Raman spectroscopy, where coherence can be generated using a laser pulse that is resonant or non-resonant with the sample. In the case of non-resonant Raman scattering, a

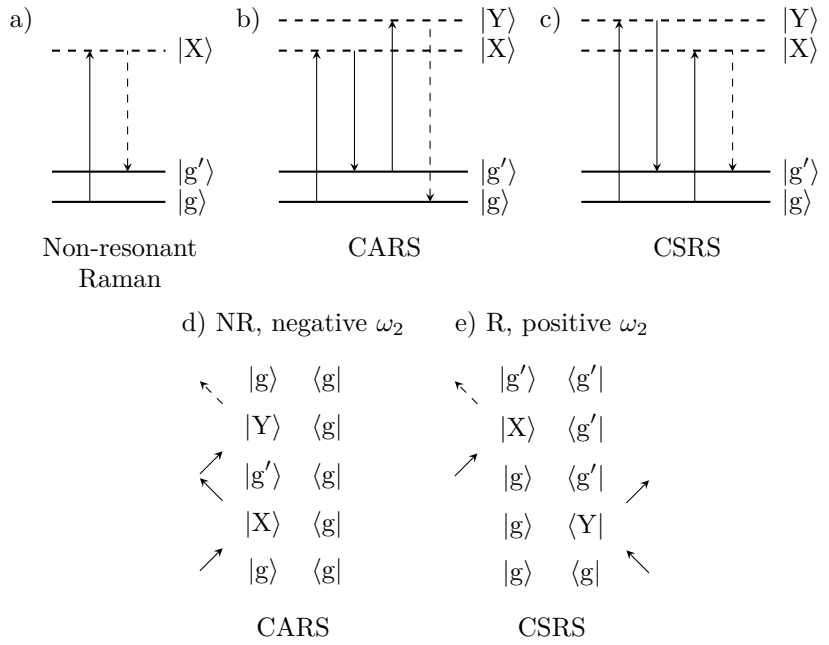

Figure 4.6: Energy level diagrams showing the interaction of light with the sample during (a) non-resonant Raman scattering, (b) CARS, and (c) CSRS. Solid horizontal lines indicate real states of the system, while dashed lines indicate virtual states. Solid arrows indicate the interaction of the three laser pulses and dashed arrows represent the signal. (d)–(e) Double-sided Feynman diagrams corresponding to (b) and (c) and consistent with literature.[108] In all diagrams $|g\rangle$ represents the ground state of the system and $|g'\rangle$ represents an excited vibrational level of the ground state, while $|X\rangle$ and $|Y\rangle$ represent virtual states.

virtual state mediates the transition between the ground state and an excited vibrational state. Conventional Raman spectroscopic measurements typically use a single continuous-wave laser source, however there are forms of Raman spectroscopy that are more comparable to 2DES. Coherent anti-Stokes Raman spectroscopy (CARS)[105,106] and coherent Stokes Raman spectroscopy (CSRS)[107] are two such forms. Like 2DES, CARS and CSRS are third-order non-linear optical techniques that use pulsed laser beams to produce a coherent signal. Additionally, the signal in CARS and CSRS is generated by the interaction of three laser pulses with the sample, and the three beams are often arranged in the BOXCARS geometry. CARS and CSRS differ from 2DES in that the three pulses are usually non-equivalent in energy, there is no LO, and fine control of the time delays between the pulses is not necessary. However, the similarities between these techniques and 2DES imply that the non-resonant coherence observed here may originate from third-order pathways involving virtual states as in CARS and CSRS.

Energy-level diagrams showing the generalised mechanisms of conventional non-resonant Raman, CARS and CSRS are shown in Figure 4.6a–c. The CARS and CSRS energy-level diagrams in Figures 4.6b and c are GSB-type pathways. Converting these energy-level diagrams to double-sided Feynman diagrams shows that a CARS-type interaction contributes to negative frequency NR coherence, while the CSRS-type interaction contributes to the positive frequency R coherence (Figures 4.6d and e). At first inspection, 2DES seems capable of probing these CARS- and CSRS-like pathways, as well as the analogous negative frequency R and positive frequency NR pathways (Appendix, Figure 4.15). However, these pathways require populating a very short-lived

virtual state between the first and second pulses. CARS and CSRS overcome this by having the first and second pulses closely spaced in time, such that the time that the system spends in the virtual state is within the short lifetime of the excited state. However, in 2DES the time between the first and second pulses is scanned from −45 fs to 45 fs and hence the time between the first and second laser pulses is likely to be greater than the lifetime of the excited state.

Another potential mechanism is fifth-order pathways, where one or more of the laser pulses interacts multiple times with the sample for a total of five interactions. 5th-order pathways have been observed in 2DES previously[109] and from three-pulse 2D infra-red spectroscopy.[110,111] Interaction of one pulse multiple times may allow the excitation and de-exitation of the virtual state to occur almost instantenously from a single pulse, and hence may not require the virtual state to be unreasonably long-lived. To detect fifth-order pathways from 2DES, the phase-matching conditions ($\boldsymbol{k}_s = -\boldsymbol{k}_1 + \boldsymbol{k}_2 + \boldsymbol{k}_3$ for R and $\boldsymbol{k}_s = +\boldsymbol{k}_1 - \boldsymbol{k}_2 + \boldsymbol{k}_3$ for NR) must be fulfilled in order for the fifth-order signal to be emitted in the same direction as the third-order signal. For this to occur, the two extra interactions must be a pair of interactions with opposite sign ($+\boldsymbol{k}_i - \boldsymbol{k}_i$). For example, a potential R fifth-order pathway would correspond to $\boldsymbol{k}_s = -\boldsymbol{k}_1 + \boldsymbol{k}_1 - \boldsymbol{k}_1 + \boldsymbol{k}_2 + \boldsymbol{k}_3$. However, the double-sided Feynman diagrams for these phase-matching conditions reveal that these fifth-order pathways are practically equivalent to their third-order counterparts and again require that the virtual state is populated during τ (Appendix, Figure 4.16). It may be possible that there are fifth-order pathways emitted at different $\boldsymbol{k}_s$ that do not require such a long-lived virtual state, which may be observed if they are scattered into the detector. A more complete study on the origin of this non-resonant coherence is clearly required and would be an interesting avenue to pursue in future work.

Finally, to complete characterisation of the 2DES data for THF, we fit the data to a physically reasonable model using global analysis. For the coherence, we use the complex multi-exponential model described in the Introduction, Section 1.2.5.2, using two components with equal lifetimes and initial frequencies of $\pm 915\,\mathrm{cm}^{-1}$. This coherence model was combined with a multi-exponential model for the kinetics of the data, again with two components. This combined model was used to globally fit all data from $T = 90$ fs onwards. The optimised coherence parameters were: frequencies of $(\pm 934.1 \pm 0.2)\,\mathrm{cm}^{-1}$ with dephasing times of (860 ± 50) fs. This relatively long dephasing time is further confirmation that the coherence observed is vibrational in nature, as electronic coherence is typically shorter lived, particularly at room temperatures.[26] The two non-oscillating exponential decay components fit to lifetimes of (150 ± 10) fs and (23 ± 6) fs. The model describes the data well, as demonstrated in Figure 4.7, which shows representative T-traces of the absorptive part of the 2DES data compared to the model. The amplitude and phase CAS for the coherence components are shown in Figure 4.8. As expected, the amplitude CAS are equivalent to the beating maps in Figure 4.5. The phase maps are complex, and as this non-resonant coherence is already poorly characterised, their interpretation lies outside the scope of this work. This work demonstrates that the common organic solvent THF can produce significant and complex coherence in 2DES experiments, and hence further research into the non-resonant coherence of solvents is required to assist with the correct interpretation of coherence in solution-phase systems.

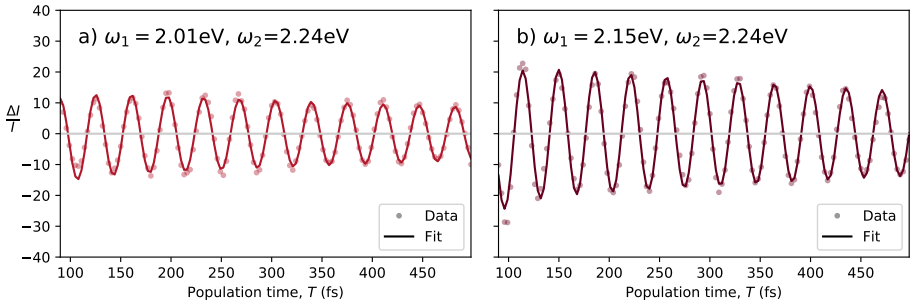

Figure 4.7: Selected T-traces of the absorptive 2DES data for THF compared with the globally fitted complex multi-exponential model described in the main text.

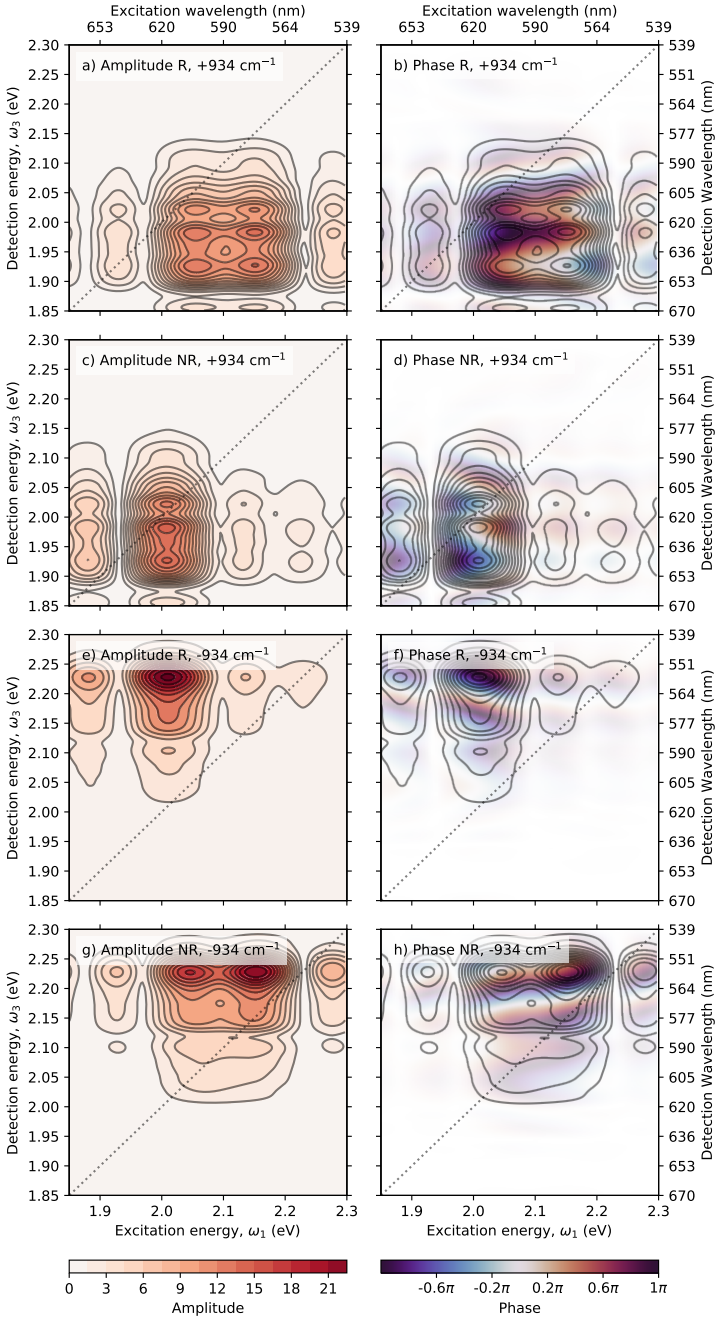

Figure 4.8: Amplitude and phase CAS for 2DES data of THF. CAS are separated into R and NR components and by sign of frequency, as indicated in the upper left of each map.

4.4 2DES of TIPS-Pn in THF

Having characterised the coherence of the solvent, we now move on to 2DES of TIPS-Pn in THF. As in the PP data, the 2DES data contain signals associated with the singlet states of TIPS-Pn. However, the additional ω_1 resolution spreads the data out over an extra dimension, and shows additional cross peaks unique to 2DES. A representative slice of the absorptive 2DES data is shown in Figure 4.9, accompanied by assignment of the 5 main signals by double-sided Feynman diagrams. The diagonal peaks 1 and 2 are assigned as GSB of $|S_{(1,0)}\rangle$ and $|S_{(1,1)}\rangle$. The cross peak labelled 3 is particularly strong, and hence likely contains contributions from both GSB and SE pathways, where SE occurs through excitation to $|S_{(1,1)}\rangle$ followed by rapid relaxation to and emission from $|S_{(1,0)}\rangle$. Peaks 4 and 5 are attributed to ESA from $|S_{(1,0)}\rangle$ and $|S_{(1,1)}\rangle$ to a higher excited singlet state.

The T-dependence of the signals is similar to that of the PP data, where the average intensity of the signals is unchanged over time, but distinct oscillatory signatures are observed (Figure 4.9b). Strong coherence is observed at 282 cm^{-1}, 550 cm^{-1}, 781 cm^{-1} and 912 cm^{-1}, with additional weaker high frequency signals around 1200 cm^{-1} and

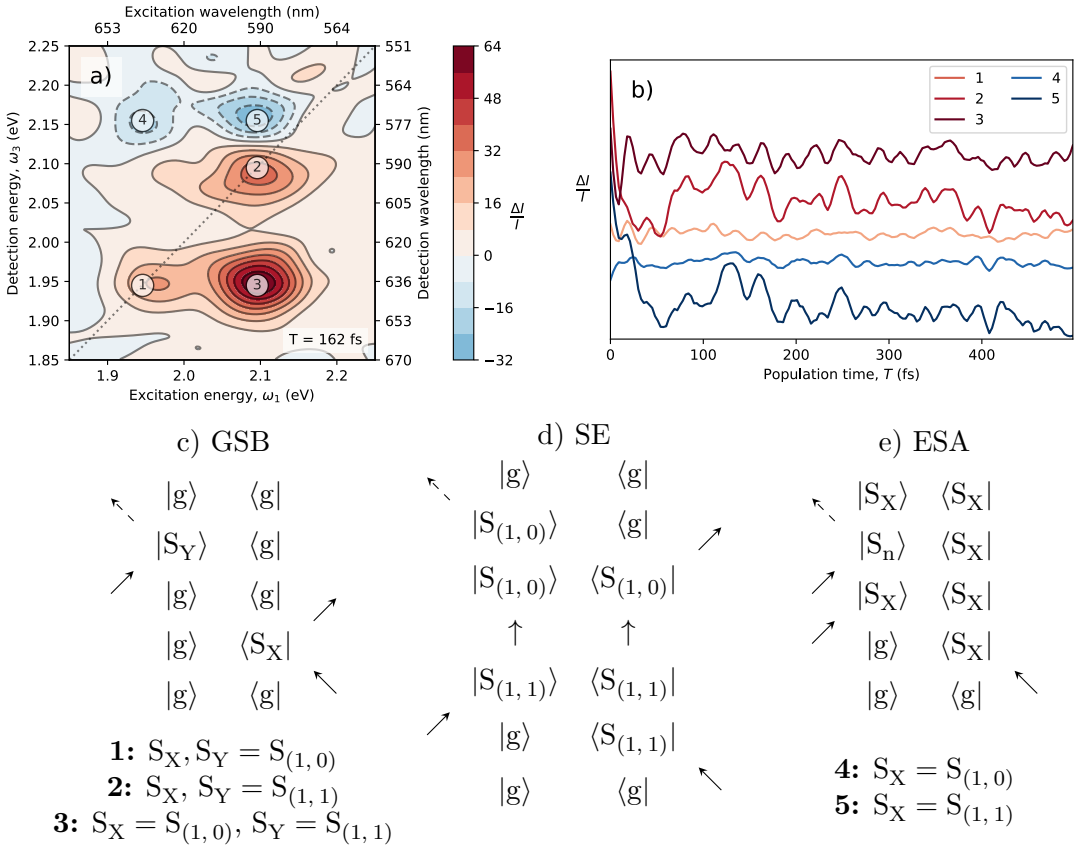

Figure 4.9: (a) Absorptive 2DES data at $T = 162\,\mathrm{fs}$ for TIPS-Pn in THF. (b) Selected T-traces of the absorptive 2DES data. Legend corresponds to the points marked in (a), and traces have been offset vertically for clarity. Energy coordinates (in eV) of peaks 1–5 are (ω_1, ω_3) = (1.94, 1.94), (2.09, 2.09), (2.09, 1.94), (1.94, 2.15), and (2.09, 2.15). Peaks numbered 1-5 are assigned by double-sided Feynman diagrams in (c)–(e). Only R diagrams are shown here for brevity, however NR diagrams are analogous and can be found in the Appendix, Figure 4.17.

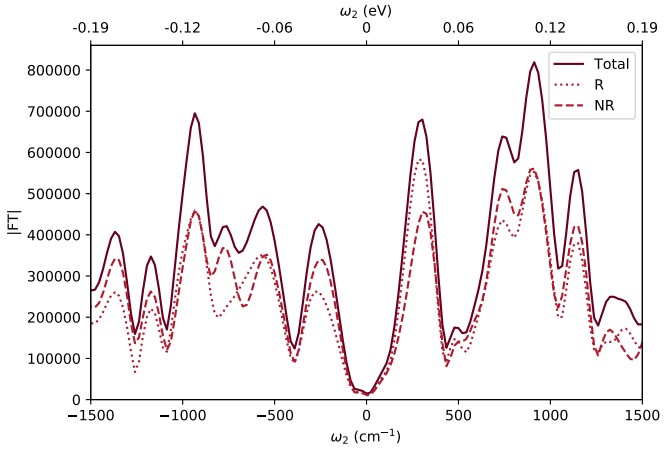

Figure 4.10: FT of the 2DES data for TIPS-Pn in THF, integrated over ω_1 and ω_3. Data were pre-processed as for Figure 4.5.

1330 cm^{-1} (Figure 4.10). These frequencies are consistent with those observed in the PP data, with the exception of 550 cm^{-1}, which is particularly weak in the Raman spectrum of TIPS-Pn.[28,56] The 912 cm^{-1} signal is attributed to the vibration of the solvent, and the beating maps for this signal are very similar to those in Figure 4.5. The remainder of the coherence is attributed to TIPS-Pn. To characterise and assign the coherence observed, we fit the data to a complex multi-exponential model, described in detail below. We do not present the beating maps for each component here as the amplitude CAS generated from the model fitting algorithm are equivalent to the beating maps.

The TIPS-Pn in THF data are fit using a similar model to that used for the THF-only data in Section 4.3; coherence is accounted for with complex exponentials, and non-oscillating kinetics are fit with a multi-exponential model. We anticipate no SF in such dilute solutions,[49] and hence a more complex kinetic model is not required as the only kinetic behaviour expected is the first-order decay of $|S_1\rangle$. For this analysis, we include two exponential decay components and six pairs of coherence frequencies to account for the six modes observed in the beating maps. The data were fit to the model from $T = 80$ fs onwards. The lifetimes of the coherence frequencies were estimated from time-frequency analysis, which showed that the coherence appears to be long-lived, with dephasing times on the order of ps at least. The model describes the data quite well, as illustrated for selected T-slices in 4.11c. The best-fit parameters for this model are summarised in Table 4.2. The lifetime of the second exponential decay component was fixed to 12 ns, the known singlet lifetime of TIPS-Pn.[51] Such a slow decay means that the singlet population is essentially constant over the time period investigated here. Five of the oscillating components have frequencies that are consistent with the known Raman modes of TIPS-Pn (components 3, 4, 5, 7 and 8 in Table 4.2), while the remaining component is close to the THF mode at 915 cm^{-1}. The dephasing time of the oscillating components are all relatively long (> 500 fs), supporting assignment as vibronic or vibrational coherence, as discussed previously. These dephasing times have relatively high uncertainties due to their length being greater than the T window available. A longer T window is required to more accurately characterise these dephasing rates.

The absorptive DAS of the two non-oscillating components are shown in Figures 4.11a and b. The short-lived DAS, Figure 4.11a, has little physical meaning, and simply

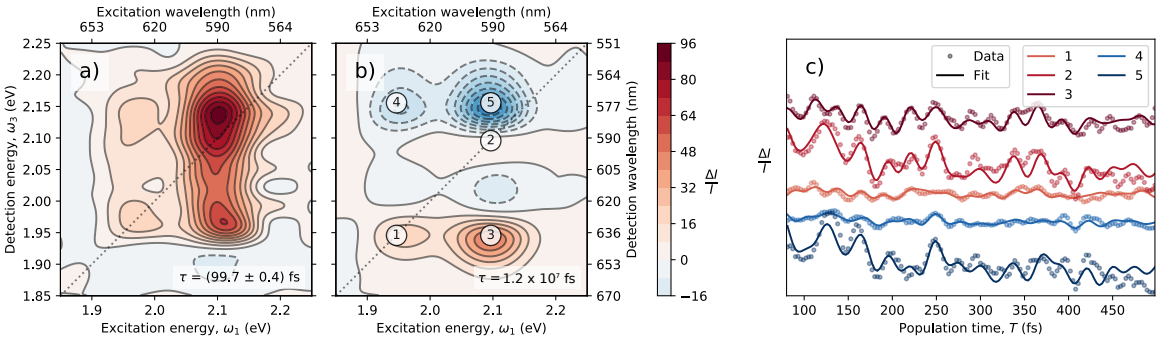

Figure 4.11: (a)–(b) Absorptive DAS from global analysis of 2DES data of TIPS-Pn in THF. Exponential lifetimes are given in the lower right corner of the maps. The 12–ns lifetime in map (b) was held constant during the fitting process. (c) Selected T-traces compared with the model. Legend corresponds to points marked in (b), and traces have been vertically offset for clarity. Energy coordinates (in eV) of peaks 1–5 are (ω_1, ω_3) = (1.94, 1.94), (2.09, 2.09), (2.09, 1.94), (1.94, 2.15), and (2.09, 2.15).

Table 4.2: Best-fit lifetimes (τ_n) and coherence frequencies (ω_n) resulting from global analysis of 2DES data of TIPS-Pn in THF.

n	τ_n (fs)	ω_n (cm^{-1})
1	99.7 ± 0.4	0^*
2	$1.2 \times 10^{7*}$	0^*
3	720 ± 20	$\pm\,(295 \pm 8)$
4	1470 ± 90	$\pm\,(520 \pm 10)$
5	504 ± 6	$\pm\,(781 \pm 2)$
6	640 ± 10	$\pm\,(940 \pm 10)$
7	1010 ± 40	$\pm\,(1159 \pm 4)$
8	860 ± 10	$\pm\,(1341 \pm 4)$

* indicates parameter was held constant during fitting

accounts for the residual effects of the early-time coherent artefacts. The long-lived map, Figure 4.11b, represents the singlet states of TIPS-Pn, and shows the 5 signals assigned to the singlet states of TIPS-Pn. The diagonal GSB at 2.10 eV is weak due to strong overlap with the ESA above it. When compared to the slice of experimental data in Figure 4.9, the peak shapes of the singlet DAS are rounded and less noisy, uncomplicated by the oscillating coherence signals. This illustrates that using a model that incorporates coherence as we have done assists with interpretation of results, by removing peak distortion due to coherence from the absorptive DAS.

The amplitude and phase CAS are shown in Figures 4.12–4.14, and in the Appendix, Figures 4.18–4.20. The CAS are complex and detailed, with distinct differences between the frequencies. The 295 cm^{-1} CAS contain multiple distinct signals per map, the 520 cm^{-1} and 781 cm^{-1} CAS are particularly weak and diffuse, and for the 1159 cm^{-1} and 1341 cm^{-1} CAS the coherence is most distinct in the positive R map. Complete diagrammatic assignment of these coherences is complicated by a number of factors. Firstly, the coherence is relatively weak and the data has a higher level of experimental noise than desired. Secondly, the presence of 6 vibrational modes makes predicting coherence locations based on double-sided Feynman diagrams significantly

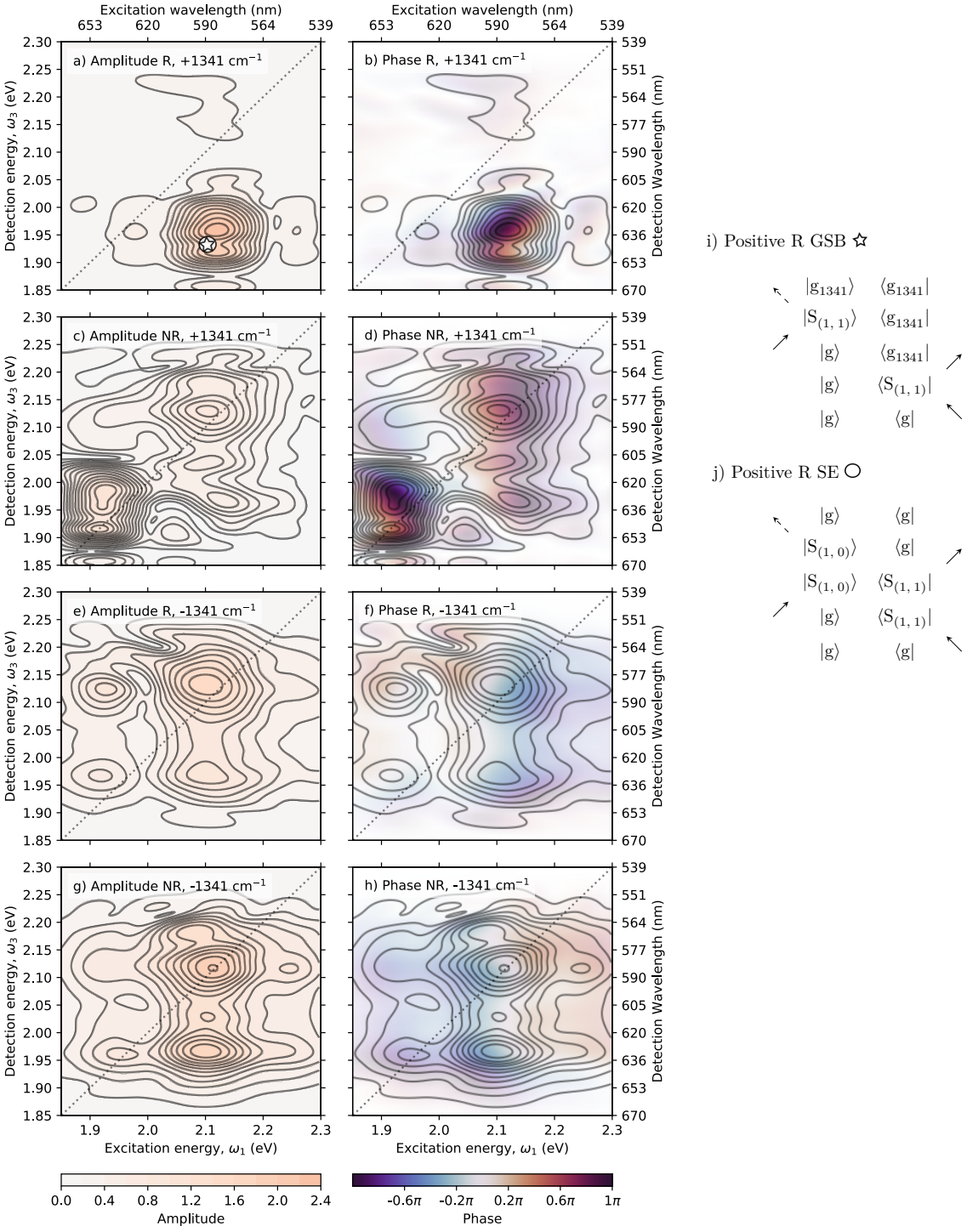

Figure 4.12: (a)–(h) Amplitude and phase CAS of component 8 (Table 4.2) from global analysis of TIPS-Pn in THF. Colour scale is consistent for Figures 4.12–4.14 and 4.18–4.20. (i)–(j) Double-sided Feynman diagrams for the pathways marked in (a).

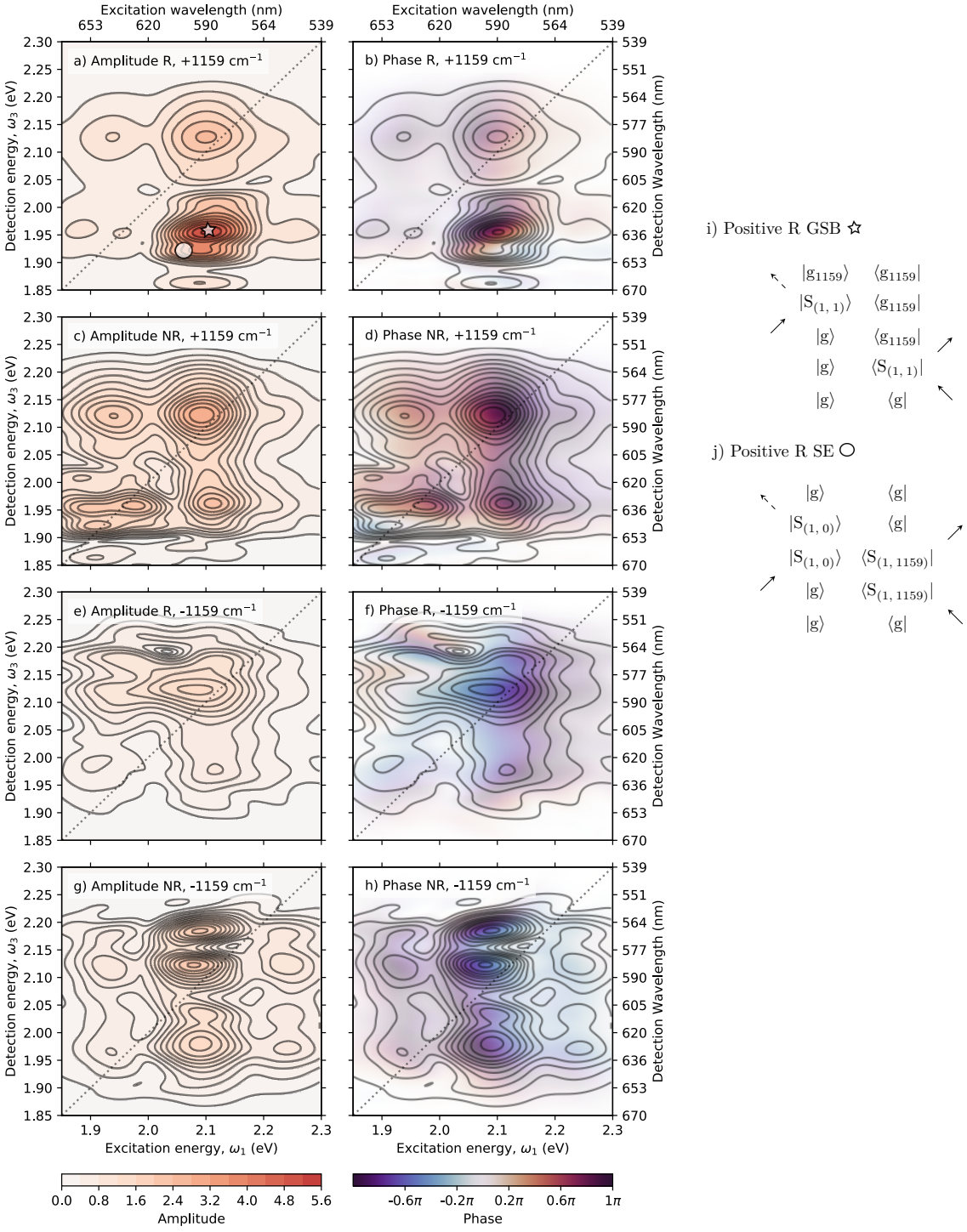

Figure 4.13: (a)–(h) Amplitude and phase CAS of component 7 (Table 4.2) from global analysis of TIPS-Pn in THF. Colour scale is consistent for Figures 4.12–4.14 and 4.18–4.20. (i)–(j) Double-sided Feynman diagrams for the pathways marked in (a).

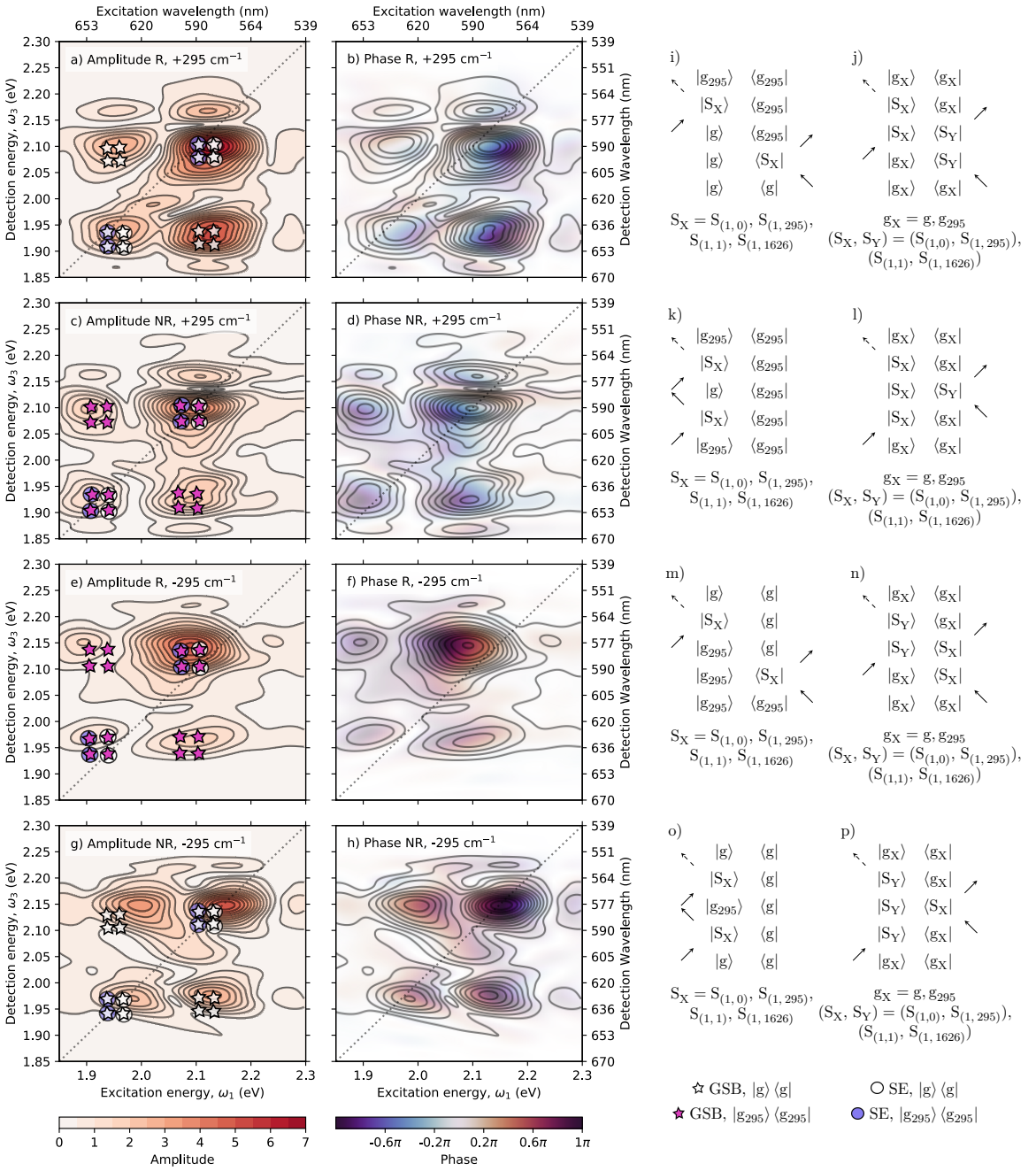

Figure 4.14: (a)–(h) Amplitude and phase CAS of component 3 (Table 4.2) from global analysis of TIPS-Pn in THF. Colour scale is consistent for Figures 4.12–4.14 and 4.18–4.20. (i)–(p) Double-sided Feynman diagrams for the theoretical coherence locations marked on the amplitude CAS. GSB pathways are marked by stars and SE by circles, with white symbols marking pathways beginning in $|g\rangle$ and coloured symbols marking pathways beginning in $|g_{295}\rangle$.

more complicated. One of the commonly quoted benefits of generating beating maps or CAS is that it is assumed that each map shows the contribution of only one mode. However, recent theoretical work predicts that multiple vibrational modes interfere with each other, generating weak combination bands and modulating the appearance of the beating maps.[112] While it is true that each beating map contains only contributions from pathways that result from coherence at a single frequency during T, during τ and t any and all of the vibrational modes of the system may be involved. Hence, we restrict assignment by double-sided Feynman diagrams to the strongest and most distinct CAS.

Consider first the two high frequency modes, 1159 cm^{-1} (0.143 eV) and 1341 cm^{-1} (0.166 eV) (Figures 4.13 and 4.12). In the following assignment we assume a minimal Stokes shift based on previous work on the fluorescence of TIPS-Pn.[113,114] The most prominent signal in both sets of CAS is in the positive R map. This signal can be accounted for by either a GSB or SE pathway, with double-sided Feynman diagrams for these pathways shown in Figures 4.13i–j and 4.12i–j. Although the other vibrational and vibronic states can be involved during τ and t, the two pathways shown are predicted to have the highest amplitude, involving transitions to and from $|\mathrm{g}\rangle$, $|\mathrm{S}_{(1,0)}\rangle$ and $|\mathrm{S}_{(1,1)}\rangle$ rather than alternative vibronic states. In Figures 4.12–4.14, vibronic states of the ground and singlet manifolds are denoted with their frequencies in subscripts, with the exception of $|\mathrm{S}_{(1,1)}\rangle$ (which is approximately 1341 cm^{-1} above $|\mathrm{S}_{(1,0)}\rangle$) as this state has established notation already. The possibility of coherence within both the ground and first excited singlet manifolds is supported by the PP data presented earlier, where the high frequency modes are found within both the GSB and ESA regions.

Moving to lower frequency, the 940 cm^{-1} mode is attributed to vibration of the solvent THF, and has similar CAS in the presence (Figure 4.18) and absence (Figure 4.8) of TIPS-Pn, with minute differences at low ω_3 that are likely to be due to slight changes in spectral shape of the laser pulses. The absorption of light around 1.95 eV and 2.09 eV by TIPS-Pn has no apparent effect on the solvent-attributed CAS. This indicates that using a solvent-only sample as a control is an effective method for determining the contributions of the solvent to the coherence of a solution. The two moderate frequency modes at 520 cm^{-1} and 781 cm^{-1} have CAS that are weak, noisy, and broad, which restricts our ability to assign these signals.

Finally, consider the low frequency mode at 295 cm^{-1} (0.037 eV). Unlike the high frequency modes, these maps are likely to have contributions from pathways starting in $|g_{295}\rangle$, as the energy of that mode is only slightly above $k_\mathrm{B}T$ at room temperatures. Hence, the number of accessible coherence pathways is increased. We find that the amplitude CAS are reasonably well predicted by GSB and SE pathways incorporating transitions from $|\mathrm{g}\rangle$ and $|\mathrm{g}_{295}\rangle$ to $|\mathrm{S}_{(1,0)}\rangle$, $|\mathrm{S}_{(1,295)}\rangle$, and $|\mathrm{S}_{(1,1)}\rangle$. However, predicted coherence locations using only these transitions fail to account for high frequency coherence signals around ω_1, $\omega_3 = 2.13$ eV. To account for these signals, we note that a high frequency TIPS-Pn Raman mode at 1626 cm^{-1} (0.202 eV) is 252 cm^{-1} above the strong 1374 cm^{-1} mode.[56] Although we are unable to measure the 1626 cm^{-1} mode directly due to its high frequency, coherence between these two high frequency modes would appear at the difference between their frequencies (252 cm^{-1}), which is similar in frequency to the 265 cm^{-1} mode, and hence will appear on the same CAS. Incorporating pathways that involve coherence between the 1374 cm^{-1} and 1626 cm^{-1} modes in the ground and excited states leads to better agreement with the observed CAS. There may also be some contribution from ESA pathways, indicated by the weak signals

around $\omega_3 = 2.15\,\text{eV}$, where the singlet ESA is observed in the absorptive map (Figure 4.9). The double-sided Feynman diagrams for the GSB and SE pathways discussed can be found in Figures 4.14i–p.

The coherence of TIPS-Pn in dilute solutions is complicated, involving at least 4 vibrational modes. We have found that for such a complex system, complete assignment using double-sided Feynman diagrams is more difficult than for the two-level, single-mode system presented in Chapter 3. We were able to partially assign the coherence, focusing on the strongest and clearest CAS. In most cases, coherence could be assigned using GSB and SE pathways, resulting in some ambiguity with respect to whether the observed vibrational modes are located in the excited singlet manifold as well as the ground state. However, in the higher quality PP data, all coherence frequencies were found in the ESA region as well as the GSB region, so it is likely that the vibronic structure of the first singlet excited state is similar to the ground state. For a more complete understanding of the origin of all coherence signals, the beating maps could be predicted using a quantum mechanical model of the system, as has been done in previous works on crystalline TIPS-Pn thin films.[28]

4.5 Conclusions

In this Chapter, PP and 2DES data for TIPS-Pn in dilute solutions were presented. In PP data for TIPS-Pn in toluene, THF and acetone, strong coherence with frequencies matching the known Raman modes of the solvents were observed, alongside weaker coherence matching the Raman modes of TIPS-Pn at $265\,\text{cm}^{-1}$, $788\,\text{cm}^{-1}$, $1158\,\text{cm}^{-1}$ and $1195\,\text{cm}^{-1}$.[28,56] A 2DES study of THF observed vibrational coherence at $912\,\text{cm}^{-1}$, matching the known Raman mode of THF in the frequency region of interest. FT and global analysis of the 2DES data for THF found that coherence in THF has a dephasing time of 800 fs and appears at distinct ω_1 and ω_3. The ω_1- and ω_3-dependence of this non-resonant coherence was rationalised by a Raman-like mechanism mediated by two virtual states, inspired by the coherent Raman spectroscopic techniques CARS and CSRS. Four GSB-type pathways were likely to contribute to the solvent coherence. CARS-type pathways contributed to the negative frequency NR map, and CSRS-type pathways contribute to the positive frequency R map. No known Raman technique was found to correspond to the positive NR and negative R pathways, which both required the system to be thermally excited to the vibrational state. This finding differs from previous reports of the energy-dependence of the coherence of solvents in solution-phase samples,[25,99] however a detailed study of solvent coherence in 2DES is still unavailable in the literature.

Coherence was also observed in 2DES data for TIPS-Pn in THF. The THF mode was present in similar locations to the coherence observed in THF without TIPS-Pn, indicating that the solvent-only sample was an effective control for deconvoluting the coherence of solutes and solvents. A number of vibrational modes of TIPS-Pn were also observed, at frequencies of $295\,\text{cm}^{-1}$, $520\,\text{cm}^{-1}$, $781\,\text{cm}^{-1}$, $1159\,\text{cm}^{-1}$ and $1341\,\text{cm}^{-1}$, with dephasing times in the 0.5 ps to 1.5 ps range. These modes were partially assigned using double-sided Feynman diagrams, however poor data quality and the presence of multiple vibrational modes made complete assignment difficult. However, the high quality PP data showed that the $265\,\text{cm}^{-1}$, $788\,\text{cm}^{-1}$, $1158\,\text{cm}^{-1}$ and $1195\,\text{cm}^{-1}$ modes are found in both the ESA and GSB regions, and thus must exist in both the ground and excited singlet state manifolds. Hence, we found that the vibronic structure of the

first excited singlet state is largely similar to that of the ground state.

4.6 Appendix

4.6.1 Additional Double-sided Feynman Diagrams

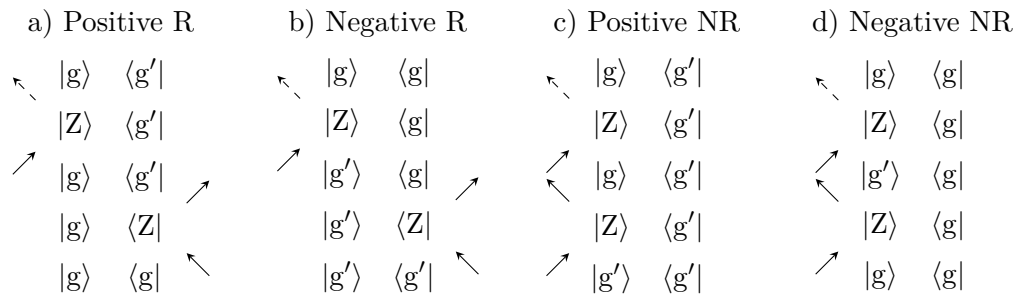

Figure 4.15: Third-order double-sided Feynman diagrams for non-resonant coherence, used to predict the theoretical coherence locations in Figure 4.5. In all diagrams $|\mathrm{g}\rangle$ represents the ground state, $|\mathrm{g}'\rangle$ is an excited vibrational level of the ground state, and $|\mathrm{Z}\rangle$ is a virtual state. In Figure 4.5, it is assumed that there are at least two non-degenerate virtual states involved in these pathways: $|\mathrm{Z}\rangle = |\mathrm{X}\rangle, |\mathrm{Y}\rangle$.

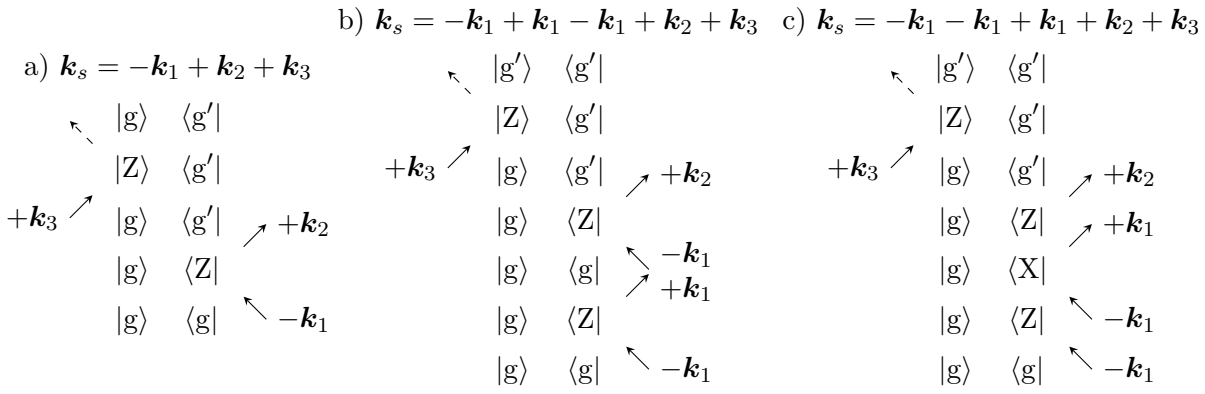

Figure 4.16: Double-sided Feynman diagrams for positive R (a) third-order and (b) – (c) selected fifth-order pathways, with phase-matching conditions as indicated. Note that all three pathways result in the same ω_1, ω_2 and ω_3. $|\mathrm{Z}\rangle$ and $|\mathrm{X}\rangle$ represent virtual states.

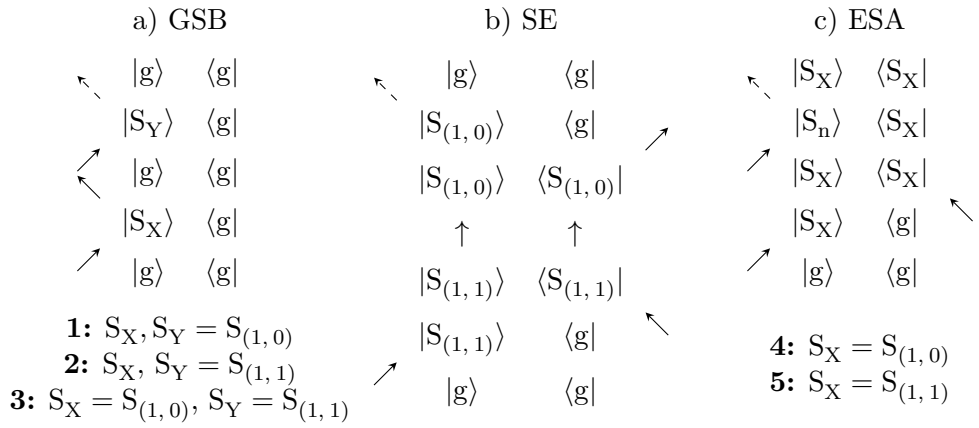

Figure 4.17: NR double-sided Feynman diagrams for Figure 4.9, assigning the 5 main signals observed in the absorptive 2DES data for TIPS-Pn in THF.

4.6.2 Additional CAS for TIPS-Pn in THF

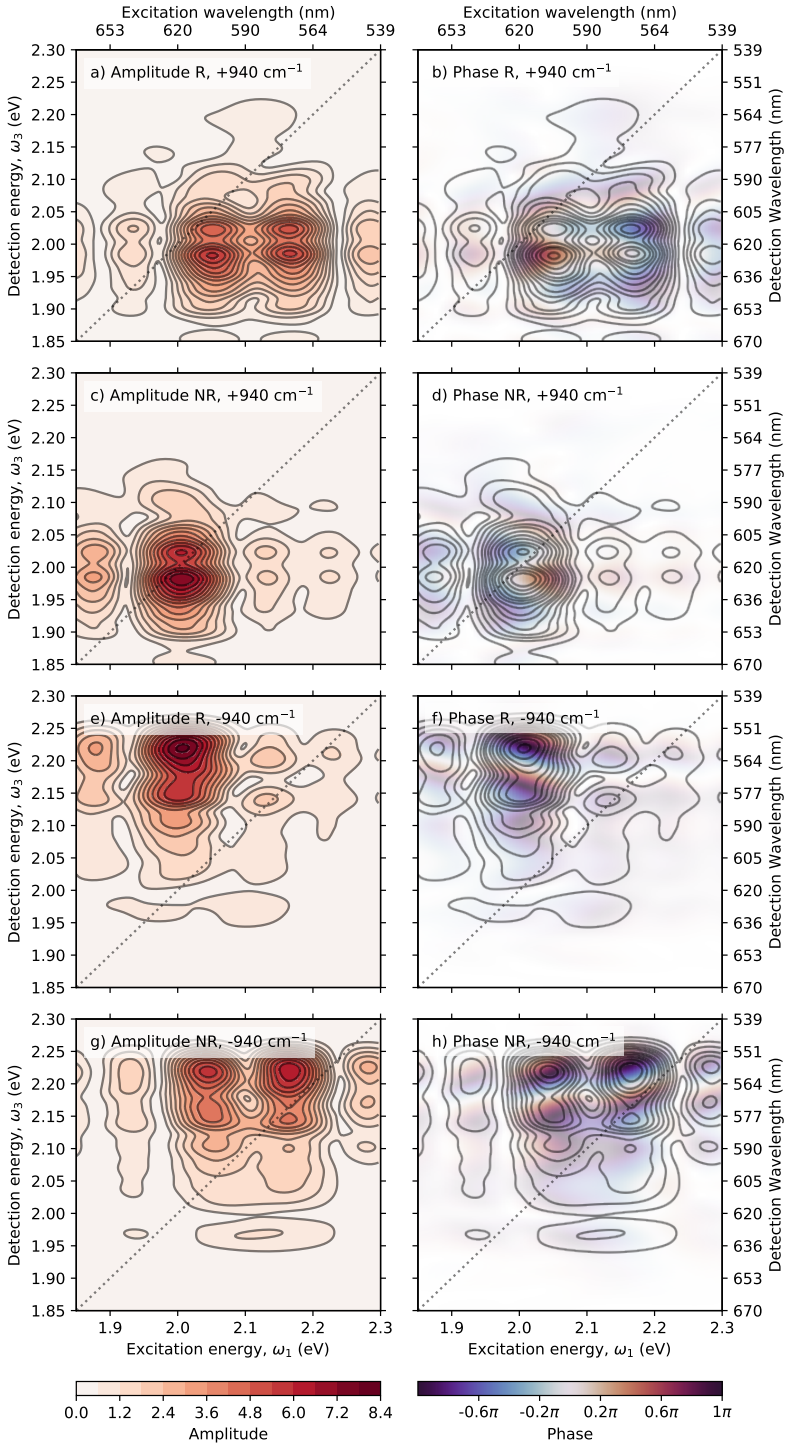

Figure 4.18: Amplitude and phase CAS of component 6 (Table 4.2) from global analysis of TIPS-Pn in THF. This mode is attributed to the non-resonant response of the solvent. Colour scale is consistent for 4.12–4.14 and 4.18–4.20.

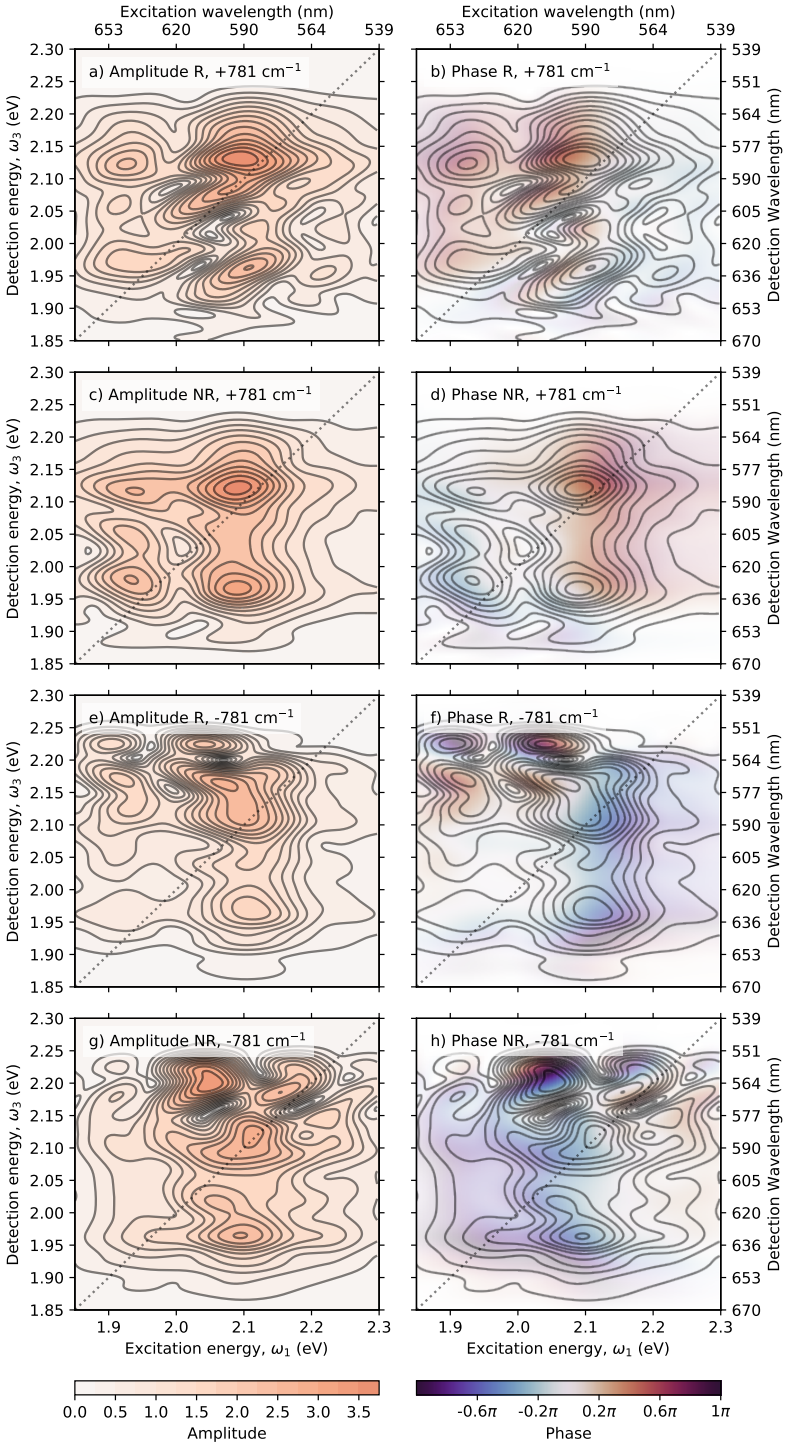

Figure 4.19: Amplitude and phase CAS of component 5 (Table 4.2) from global analysis of TIPS-Pn in THF. Colour scale is consistent for Figures 4.12–4.14 and 4.18–4.20.

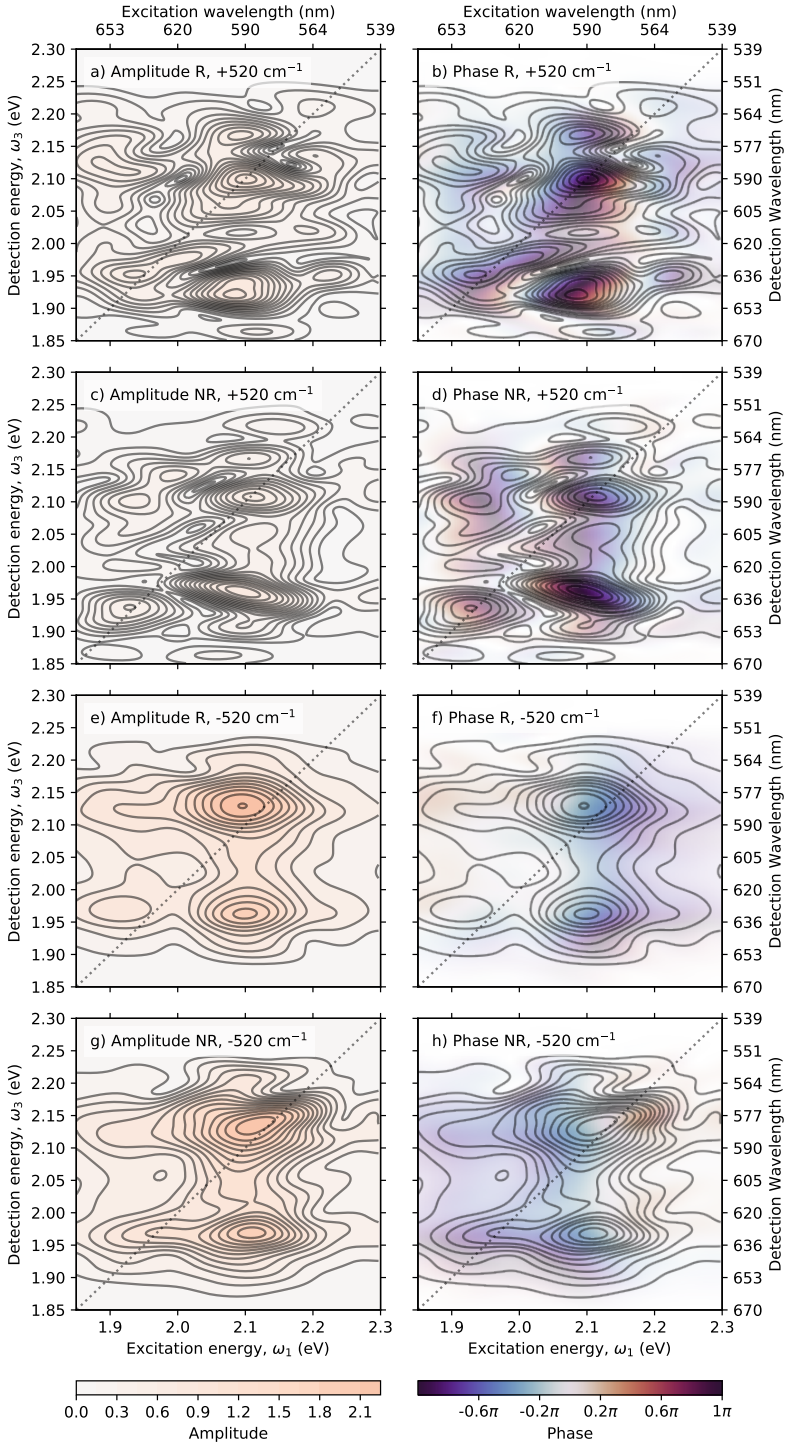

Figure 4.20: Amplitude and phase CAS of component 4 (Table 4.2) from global analysis of TIPS-Pn in THF. Colour scale is consistent for Figures 4.12–4.14 and 4.18–4.20.

CHAPTER 5
Singlet Fission and Coherence in Amorphous and Crystalline TIPS-Pn Nanoparticles

In Chapter 4, PP and 2DES experiments found that in dilute solutions of TIPS-Pn, coherence was observed within both the ground and excited singlet states, at frequencies corresponding to the Raman modes of TIPS-Pn. In this chapter, we extend the study to amorphous and crystalline NPs of TIPS-Pn, where SF occurs. In amorphous TIPS-Pn NPs we observe negligible SF, as it is slow compared to the available T window. However, we observe coherence at similar frequencies and with similar ω_1- and ω_3-dependence as for TIPS-Pn in dilute solutions, indicating that in the amorphous NPs the vibrations of TIPS-Pn in both the ground and excited singlet states are similar to those in isolated TIPS-Pn molecules. In crystalline TIPS-Pn NPs, the SF rate is significantly faster, and SF is observed through the rise of a triplet pair ESA signal. To gain a better understanding of the triplet pair state, 2DES experiments are performed using both low and high photon energy pulses. In the low photon energy experiments, coherence is observed, but it is weak and close to the noise floor. Using FT and TFTs we observe that a mode around $250\,\mathrm{cm}^{-1}$ increases in intensity over T in a region corresponding to triplet pair ESA. This indicates that this mode may be found in the triplet pair manifold, but it would be desirable to confirm this result with higher quality data. No significant or repeatable coherence was observed in the high photon energy experiments for crystalline TIPS-Pn NPs, which may be due to any coherence signals being below the noise floor of the instrument.

5.1 Steady-state Characterisation of TIPS-Pn Nanoparticles

The steady-state UV–visible absorption spectra of amorphous and crystalline TIPS-Pn NPs are shown in Figure 5.1. These NPs are aqueous colloidal suspensions prepared by re-precipitation, as described in the Methods, Section 2.2.2. The absorption spectrum of as-prepared NPs is very similar in shape to that of TIPS-Pn in solution, with only a small redshift relative to the solution spectrum observed. The strong similarities between the as-prepared TIPS-Pn NP and solution spectra indicates that within these NPs the TIPS-Pn molecules are arranged randomly and the intermolecular coupling is weak. We refer to these as-prepared NPs henceforth as amorphous NPs. As described in the Methods, Section 2.2.2, and previous work by Hudson et al. and Pensack et al.,[50,53] addition of PVA to amorphous TIPS-Pn NPs results in rapid conversion of the NPs to a crystalline morphology. These crystalline NPs show a distinct and characteristic spectral shape change compared to the amorphous NPs, where the peaks undergo considerable broadening and redshifting due to strong intermolecular coupling. The progression of peaks from 1.7 eV to 2.4 eV is often taken to be vibronic,[53,60] however a study of the polarisation-dependence of the crystalline TIPS-Pn absorption spectrum found that the peak at 1.92 eV contains electronic contributions distinct from the 1.78 eV peak, as well as vibronic contributions.[115]

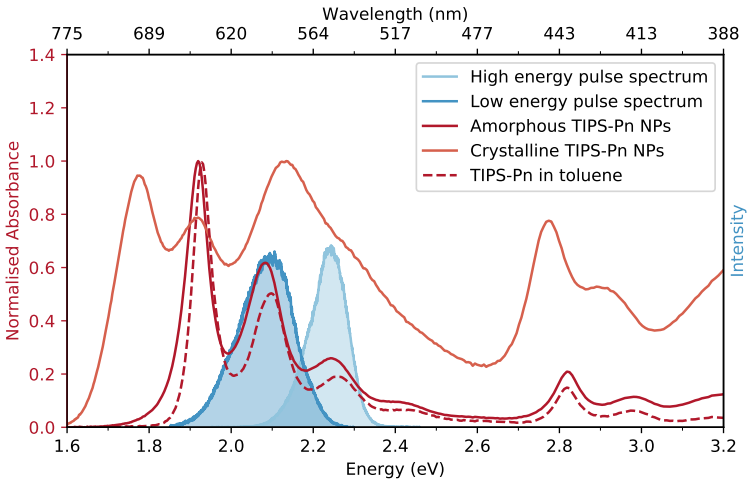

Figure 5.1: Normalised steady-state UV–visible absorption spectra of amorphous and crystalline TIPS-Pn NPs, and TIPS-Pn in toluene. NP concentration was 200 ppm and spectra were collected in a 1–mm path length cuvette. The spectrum of TIPS-Pn in toluene has been scaled to the maximum of the amorphous NP spectrum for ease of comparison. The spectra of the high and low photon energy laser pulses used in 2DES are shown for reference (blue, shaded).

5.2 2DES of Amorphous TIPS-Pn Nanoparticles

2DES data for amorphous TIPS-Pn NPs were collected using the low photon energy range pulses. A representative absorptive slice and selected T-slices of the 2DES data is shown in Figure 5.2. The absorptive map (Figure 5.2a) is similar to the data from TIPS-

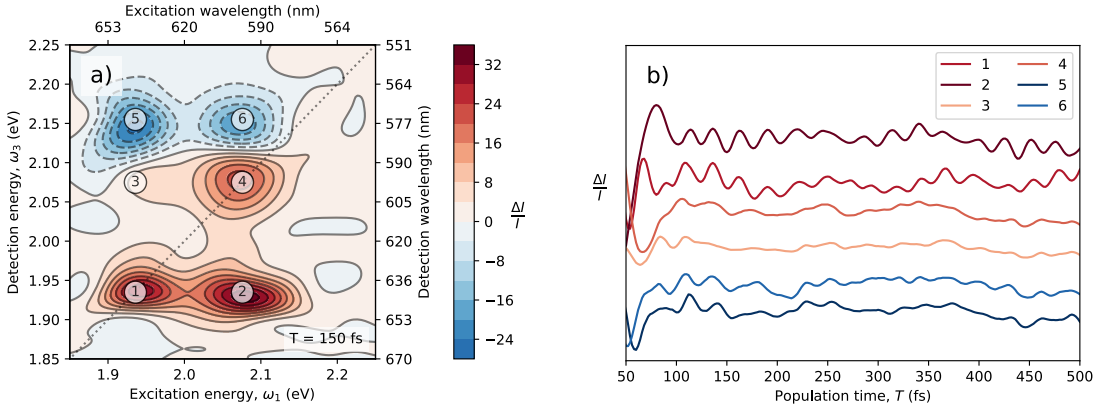

Figure 5.2: (a) Representative absorptive slice of 2DES data for amorphous TIPS-Pn NPs. (b) Selected T-slices of the data in (a). Legend corresponds to the peaks labelled in (a), and traces have been vertically offset for clarity. Energy coordinates of points 1–6 (in eV) are (1.93, 1.93), (2.07, 1.93), (1.93, 2.07), (2.07, 2.07), (1.93, 2.15) and (2.07, 2.15).

Pn in solution discussed in Chapter 4, with a slight redshift relative to the solution data reflecting the aforementioned changes in the steady-state absorption. Peaks 1 and 4 are assigned as ground-state bleaching of the $|S_{(1,0)}\rangle$ and $|S_{(1,1)}\rangle$ states, at energies of 1.93 eV and 2.07 eV. Peaks 2 and 3 are assigned as cross peaks resulting from the shared ground state of $|S_{(1,0)}\rangle$ and $|S_{(1,1)}\rangle$. Finally, peaks 5 and 6 are assigned as ESAs from the $|S_1\rangle$ manifold to a higher singlet state. Previous transient absorption measurements of amorphous TIPS-Pn NPs have identified strong overlap between the singlet and triplet ESA in the 2.76 eV to 2.14 eV energy range. However, at $\omega_3 = 2.15$ eV the ESA is considered to be primarily singlet in nature.[51] Additionally, we do not expect to observe triplet ESA at such early times, as the time constant of the initial step of SF (singlet to triplet pair) in these NPs has previously been measured to be 3.9 ps.[51]

Over T, there is very little change in the average intensity of the absorptive 2DES data for amorphous TIPS-Pn NPs, as shown in Figure 5.2b. This behaviour is expected, as SF in these amorphous NPs is known to be slow compared to the available T window.[50,51,54] Weak oscillations are observed, particularly in peaks 1 and 2. We analyse these data in more detail below using the analysis framework described in Chapter 3. Taking the FT of these data shows that the coherence frequencies of amorphous TIPS-Pn NPs are similar to those of TIPS-Pn in dilute THF solutions (Figure 5.3). In both systems, coherence is observed around 265 cm^{-1}, 520 cm^{-1}, 800 cm^{-1}, 1150 cm^{-1} and 1340 cm^{-1}. The additional mode at 915 cm^{-1} in the TIPS-Pn in solution data is due to the vibration of the solvent, THF, as discussed in Chapter 4, Section 4.4. As a control, 2DES data were also collected for a sample of water. The 2DES water control contained very low absorptive signal, and a weak oscillating signal around 550 cm^{-1} (Appendix, Figure 5.14). The origin of this oscillation are somewhat unclear; water has some weak Raman vibrations in this frequency region, but the stronger modes are at significantly higher frequencies.[116] No significant coherence was detected in the broadband PP water control. The FT amplitude of this oscillation ($|FT| \approx 6$) is over an order of magnitude lower than the FT amplitude of the oscillations observed in the amorphous TIPS-Pn NP sample ($|FT| \approx 100 - 300$). Hence, this oscillation is unlikely to contribute significantly to the coherence when TIPS-Pn in present, however some caution should be used when analysing coherence around 550 cm^{-1}.

Using the coherence frequencies extracted by the FT, we then fit these data to a

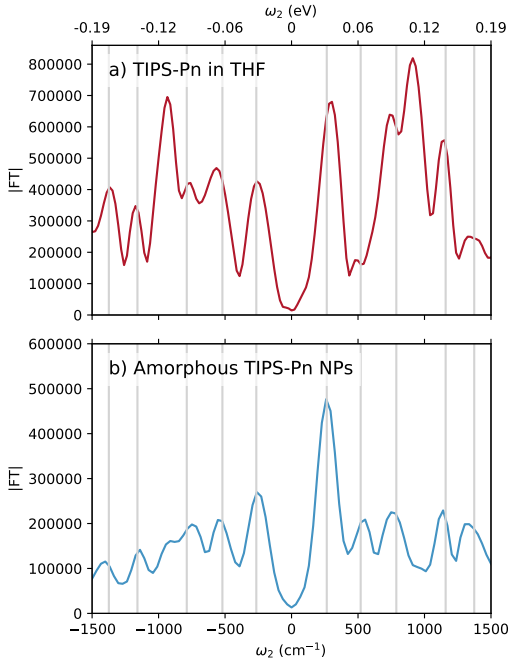

Figure 5.3: Total integrated FT for 2DES of (a) TIPS-Pn in a dilute solution of THF and (b) amorphous TIPS-Pn NPs. Removal of data before a waiting time of 90 fs, a Butterworth 8th order, 200 cm^{-1} highpass filter, Hann windowing and zero padding to $n = 512$ were applied before taking the FT. Vertical lines indicate positions of common modes, at frequencies of 265 cm^{-1}, 520 cm^{-1}, 788 cm^{-1}, 1159 cm^{-1} and 1374 cm^{-1}.

model using the global analysis method described in the Introduction, Section 1.2.5.2. As SF in these amorphous NPs is known to be slow compared to the T window available (500 fs), we expect to observe very little SF during this T window. Hence, a complex kinetic scheme describing the SF mechanism is not required to fit this data, and instead the kinetics are fit using a sum of exponentials. Five pairs of coherence frequencies are included to fit the oscillating components of the data. The data are fit from $T = 90$ fs onwards. The best-fit coherence frequencies, dephasing rates and exponential lifetimes are given in Table 5.1. The model fits the data reasonably well (Figure 5.4b), but the relative weakness and complexity of the coherence coupled with the short T window reduces the quality of this fit.

Two exponential components were required to fit the data. The first exponential component has a very short lifetime and was included to account for the residual effects of pulse-overlap at $T < 90$ fs; it is considered to have little physical meaning. The second exponential component has a lifetime on the order of picoseconds and a DAS (Figure 5.4a) that reflects the expected appearance of the TIPS-Pn singlet states. This is consistent with the observation that the 2DES data exhibit only minor changes (apart from oscillations) over the T window observed, due to the relatively slow SF. A time constant on this scale is consistent with the rate of decay of the singlet population due to SF in amorphous TIPS-Pn NPs,[51] although we note that accurately measuring such long time constants is difficult with such a short available T window.

The five oscillating components are in good agreement with the FT and the Raman spectrum of TIPS-Pn.[28,56] The fitted decoherence times are relatively long, indicating vibrational or vibronic coherence. The ps-scale decoherence times are also approximately consistent with the decoherence times of the coherence of TIPS-Pn in dilute

Table 5.1: Best-fit decoherence times (τ_n) and coherence frequencies (ω_n) resulting from global analysis of 2DES data of amorphous TIPS-Pn NPs.

n	τ_n (fs)	ω_n (cm^{-1})
1	20 ± 6	0^*
2	ps-scale	0^*
3	1300 ± 300	$\pm\,(261 \pm 8)$
4	890 ± 50	$\pm\,(520 \pm 40)$
5	900 ± 100	$\pm\,(800 \pm 40)$
6	1000 ± 100	$\pm\,(1160 \pm 20)$
7	ps-scale	$\pm\,(1340 \pm 30)$

* indicates parameter was held constant during fitting

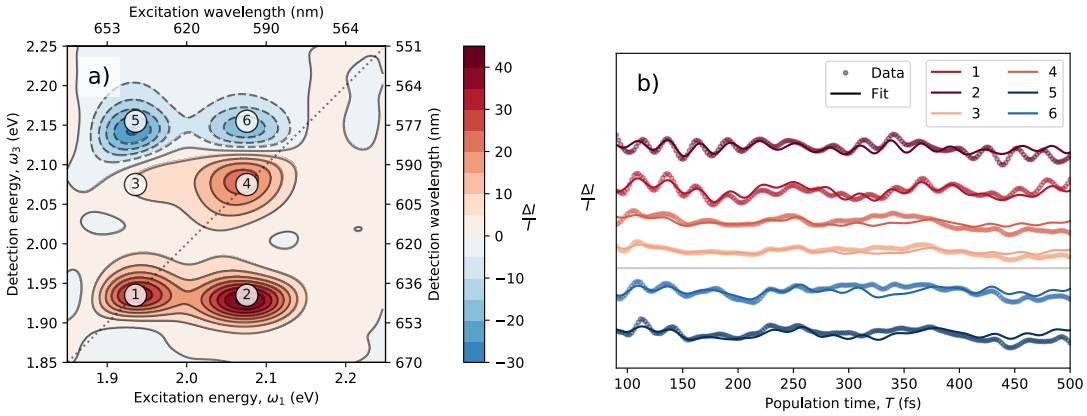

Figure 5.4: (a) Absorptive DAS for the long-lived exponential component ($n = 2$ in Table 5.1), obtained from global analysis of 2DES data of amorphous TIPS-Pn NPs. Exponential lifetime is marked in the bottom right. (b) T-slices of absorptive 2DES data at selected ω_1 and ω_3, with fits from the model presented in Table 5.1 overlaid. Traces have been offset vertically for clarity. Legend corresponds to locations marked in (a). Energy coordinates of points 1–6 (in eV) are (1.93, 1.93), (2.07, 1.93), (1.93, 2.07), (2.07, 2.07), (1.93, 2.15) and (2.07, 2.15).

solutions of THF. The agreement between the solution and amorphous NP lifetimes is not exact, likely due to errors introduced by these coherences persisting for significantly longer than the available T window. A longer T window would be required to characterise these time constants with higher accuracy.

The amplitude and phase CAS are shown in Figures 5.5–5.7 and in the Appendix, Figures 5.15 and 5.16. As previously discussed in Chapter 4 for TIPS-Pn in dilute solution, analysis of CAS in the presence of multiple vibrational modes is made complicated by the increasingly numerous potential coherence pathways. Hence, we restrict our assignment to the modes that show the clearest and strongest CAS. For the following discussion, we take the energies of the 0–0 and 0–1 transitions to be 1.92 eV and 2.00 eV, respectively, based on the steady-state absorption (Figure 5.1) and assume a minimal Stokes shift based on previous studies on the fluorescence of TIPS-Pn.[113,114]

We first consider the two high frequency modes at 1160 cm^{-1} (0.144 eV) and 1340 cm^{-1} (0.166 eV) (Figures 5.5 and 5.6). For both of these modes, the only maps with appreciable coherence intensity are the positive R and NR maps. For the positive NR maps,

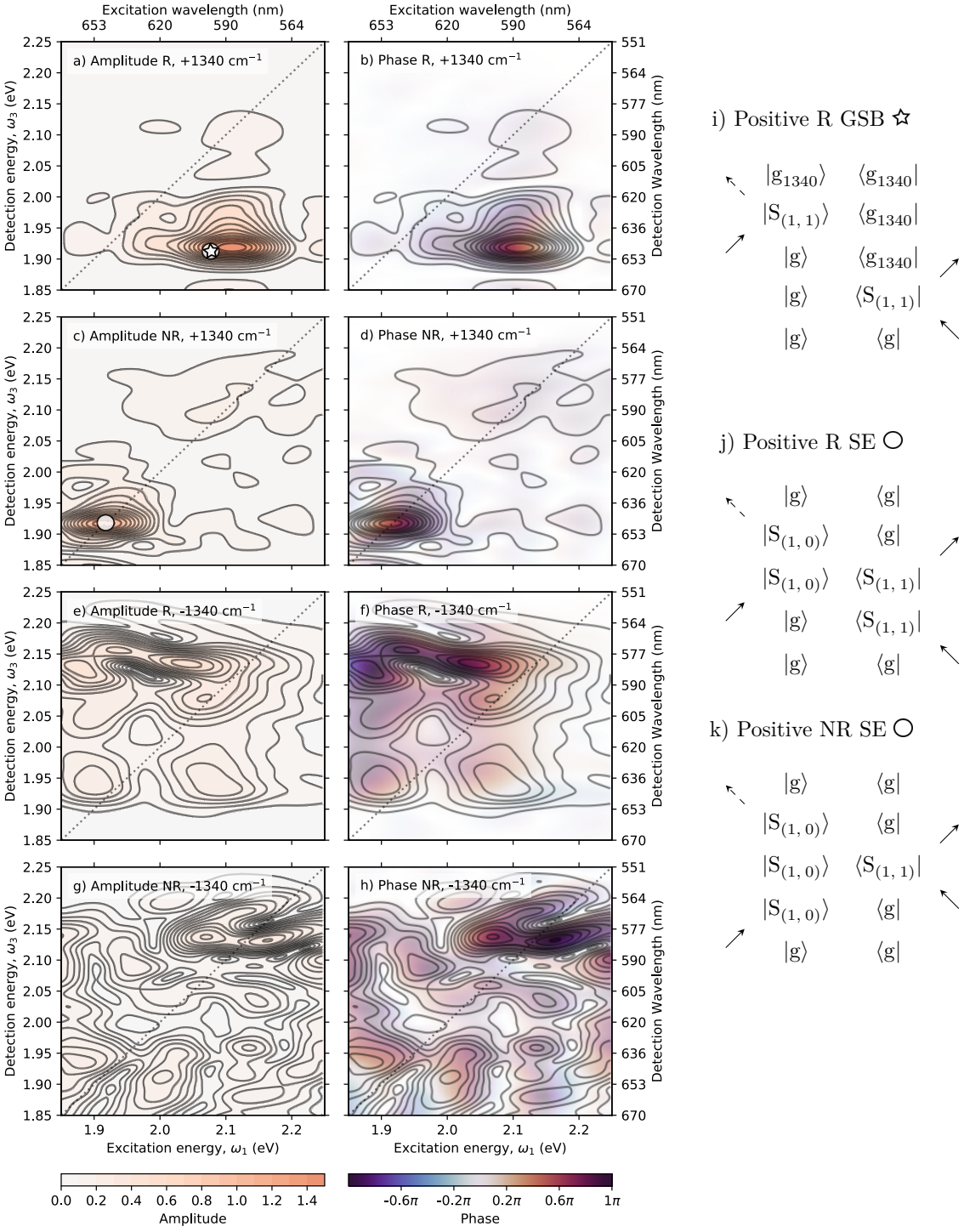

Figure 5.5: (a)–(h) Amplitude and phase CAS of component 7 (Table 5.1) from global analysis of amorphous TIPS-Pn NPs. Colour scale is consistent for Figures 5.5–5.7 and 5.15–5.16. (i)–(k) Double-sided Feynman diagrams for the GSB (white stars) and SE (white circles) pathways marked in maps (a) and (c).

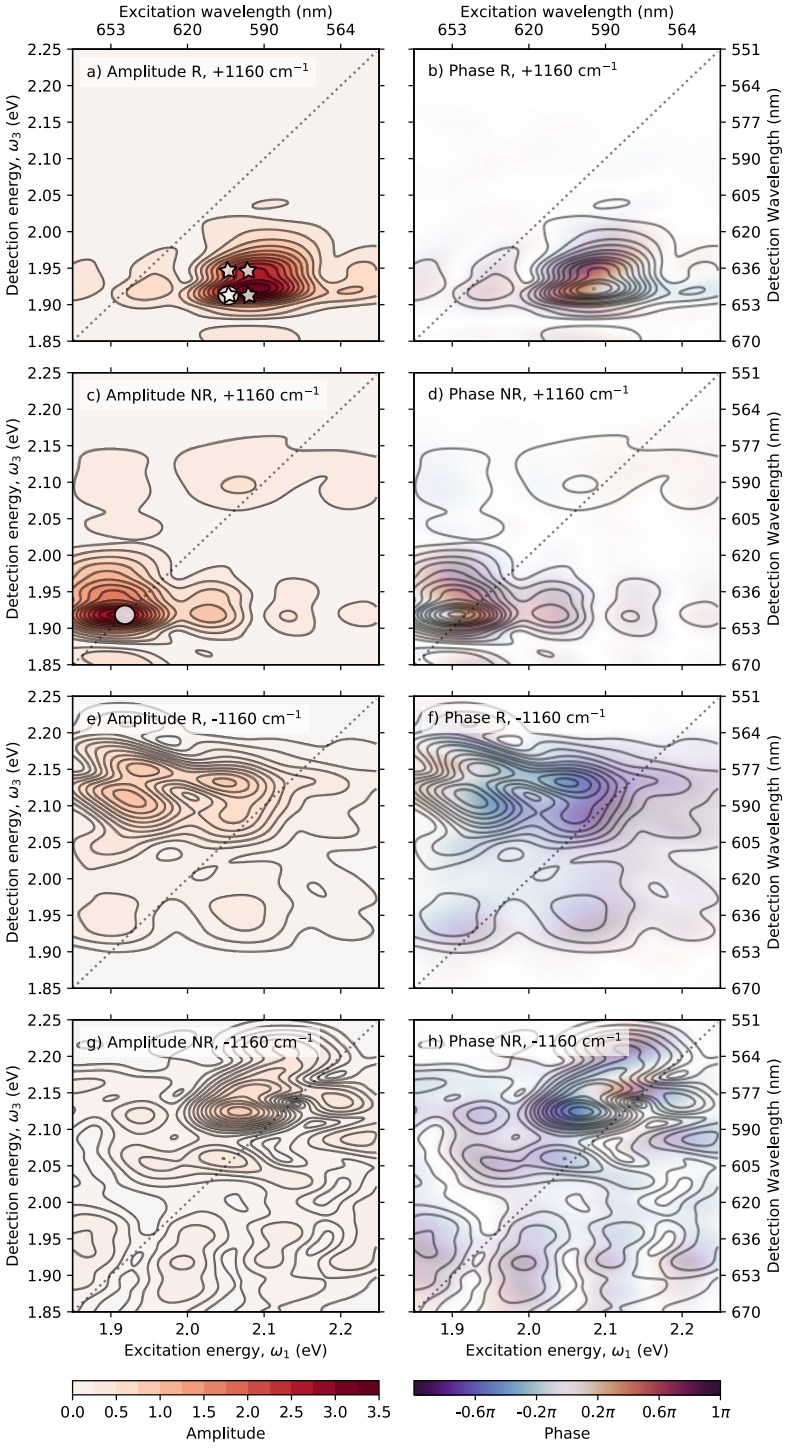

i) Positive R GSB ☆

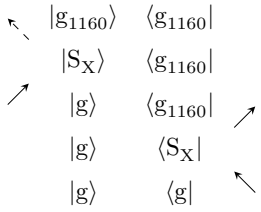

$S_X = S_{(1,\,1)}, S_{(1,1160)}$

j) Positive R SE ○

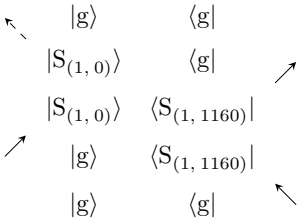

k) Positive NR SE ○

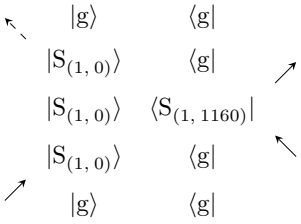

Figure 5.6: (a)–(h) Amplitude and phase CAS of component 6 (Table 5.1) from global analysis of amorphous TIPS-Pn NPs. Colour scale is consistent for Figures 5.5–5.7 and 5.15–5.16. (i)–(k) Double-sided Feynman diagrams for the GSB (white stars) and SE (white circles) pathways marked in maps (a) and (c).

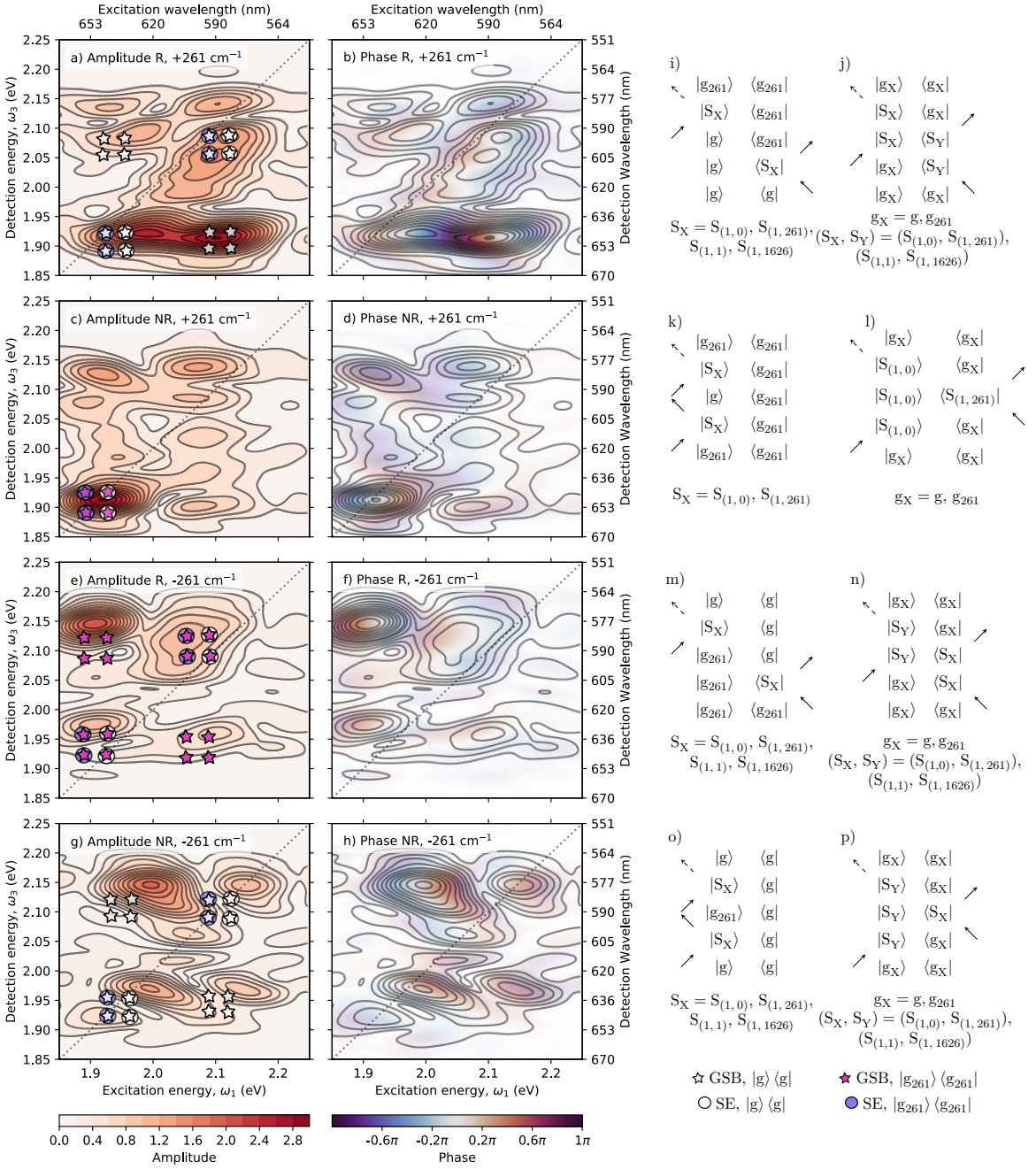

Figure 5.7: (a)–(h) Amplitude and phase CAS of component 3 (Table 5.1) from global analysis of amorphous TIPS-Pn NPs. Colour scale is consistent for Figures 5.5–5.7 and 5.15–5.16. (i)–(n) Double-sided Feynman diagrams for the pathways marked on the amplitude CAS. Stars, circles, and squares indicate GSB, SE, and ESA pathways respectively, with white symbols for pathways starting in $|g\rangle$ and coloured symbols for pathways starting in $|g_{261}\rangle$.

GSB pathways are unlikely to be contributing as they would require the system to start in the vibrationally excited ground state. We consider this to be unlikely at high frequencies, given the minimal thermal population of these states at ambient temperature. These maps are well described by a single SE pathway beginning in $|g\rangle$, which is predicted to occur diagonally at the energy of the 0–0 transition at 1.92 eV, independent of coherence frequency (Figures 5.6k and 5.5k). For the positive R maps, both GSB and SE pathways must be considered, and their double-sided Feynman diagrams are given in Figures 5.6i–j and 5.5i–j. For the GSB pathways, any and all vibronic states of the $|S_1\rangle$ could be involved during τ and t. However, we consider only the most probable transitions involving $|g\rangle$, $|S_{(1,0)}\rangle$, $|S_{(1,1)}\rangle$, and (for the 1160 cm^{-1} maps) $|S_{(1,1160)}\rangle$. The coherence energies predicted by this limited set of pathways are in good agreement with the observed positive R CAS. This assignment indicates that the 1160 cm^{-1} and 1340 cm^{-1} modes are present in both the ground and first excited singlet manifolds.

Similarly to the CAS for TIPS-Pn in solution from Chapter 4, for amorphous TIPS-Pn NPs the CAS of the two moderate frequency modes at 520 cm^{-1} and 800 cm^{-1} are particularly weak and noisy. Notably, the 520 cm^{-1} CAS has an ω_1- and $|omega_3$-dependence that is dissimilar to that observed for the potential non-resonant coherence at 550 cm^{-1} identified in the water control. Weak coherence at these frequencies is consistent with the Raman spectrum of TIPS-Pn,[28,56] where these two modes are weak compared to the 265 cm^{-1} mode and to those above 1100 cm^{-1}. Finally, the low frequency mode at 261 cm^{-1} (0.032 eV) is strong and shows complex structure in all four maps (Figure 5.7). As discussed in Chapter 4, Section 4.4 for TIPS-Pn in THF, the 261 cm^{-1} mode lies only just above k_BT at room temperature, so we expect a substantial population in the vibrationally excited ground state. The presence of this population increases the number of potential coherence pathways. We follow a similar assignment process for this CAS as for the 265 cm^{-1} CAS for TIPS-Pn in THF in Chapter 4 (Figure 4.14). We assign these signals to GSB and SE pathways where coherence is observed between $|g\rangle$ and $|g_{261}\rangle$, and between $|S_{(1,0)}\rangle$ and $|S_{(1,261)}\rangle$. Additionally, we include pathways where coherence occurs between the 1374 cm^{-1} and 1626 cm^{-1} modes (frequency difference of 252 $cm^{-1} \approx 265\,cm^{-1}$), as was done for TIPS-Pn in THF. We find that the CAS are in reasonable agreement with the assignment. There is some coherence signal at high ω_3 that could be accounted for by ESA pathways, occurring at the same ω_1 as the SE pathways shown in Figure 5.7 and with $\omega_3 \approx 2.15$ eV. The agreement between the CAS and both the SE and GSB pathways indicates that the 265 cm^{-1} mode is likely to be found in both the ground and excited states.

To summarise, within the first 500 fs of excitation, amorphous TIPS-Pn NPs behave similarly to isolated TIPS-Pn molecules. The concentration of the singlet state is essentially unchanged, and minimal SF is observed due to the weak intermolecular coupling of TIPS-Pn molecules in the amorphous morphology. Coherence is observed at 261 cm^{-1}, 520 cm^{-1}, 800 cm^{-1}, 1160 cm^{-1} and 1340 cm^{-1}, with lifetimes on the order of 1 ps to 3 ps. Assignment by double-sided Feynman diagrams reveals that modes at 261 cm^{-1}, 1160 cm^{-1} and 1340 cm^{-1} are found in the excited singlet manifold. Additionally, the amplitude and phase CAS for the amorphous TIPS-Pn NPs are quite similar to those observed for TIPS-Pn in THF, indicating that the coherence pathways for the singlet states of TIPS-Pn in an amorphous solid are similar to those for isolated TIPS-Pn molecules. To more completely characterise SF in this system using this technique, a longer T window is required. However, the shorter T window (500 fs) used in this thesis is adequate for systems where SF is much faster.

5.3 2DES of Crystalline TIPS-Pn Nanoparticles

2DES data were collected for crystalline TIPS-Pn NPs in both the high and low photon energy ranges. Representative maps for both energy ranges at $T = 243$ fs are shown in Figures 5.8a and c. In the low energy range, the 2DES spectra (Figure 5.8a) contains diagonal GSB signals (peaks 2 and 3) corresponding to bleaching of the broad steady-state absorption peaks at 1.92 eV and 2.14 eV and weak cross peaks at peaks 1 and 4. An ESA is also observed at 1.98 eV, which has been previously assigned as a predominantly singlet ESA.[50,53] In polycrystalline TIPS-Pn, rapid SF occurs within the first 100 fs following excitation.[28,53,56,75,76] Thus, we expect to observe rapid decay of singlet ESA signals, correlated with the rise of triplet ESA. We observe that the ESA at $\omega_3 = 1.98$ eV undergoes a rapid decrease in intensity, indicating predominantly singlet character. The persistence of this ESA at longer T indicates that it also has some triplet character. Over T, the GSB features are unchanged, with the exception of peak 2, which undergoes a slow decrease in intensity. In transient absorption and broadband PP studies, a triplet ESA has been shown to have strong overlap with this GSB feature,[28,53,56,75,76] and hence the observed decrease in intensity is likely due to an increasingly negative triplet ESA signal in this region.

2DES data in the higher energy range (Figure 5.8c) were collected as it is known

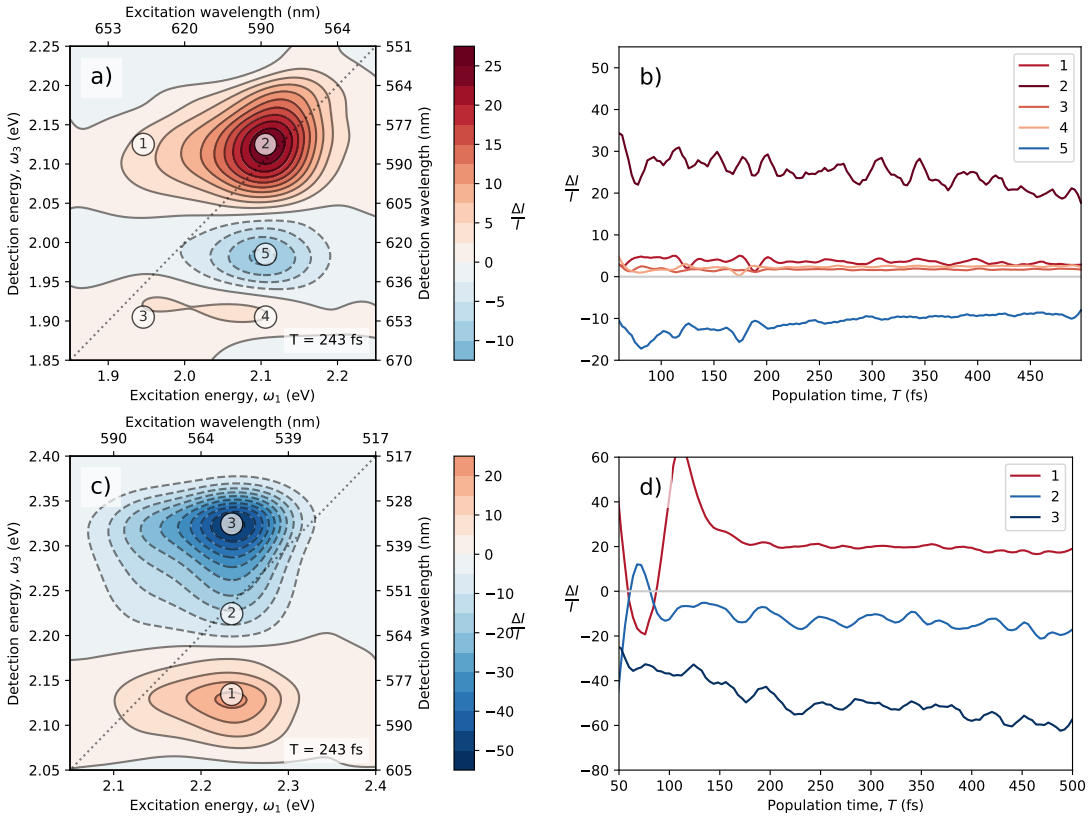

Figure 5.8: (a) Absorptive map of 2DES data for crystalline TIPS-Pn NPs in the low energy region at $T = 243$ fs. (b) Selected T-traces for the points marked in (a). Energies coordinates (in eV) of points 1–5 in (a) and (b) are: (ω_1, ω_3) = (1.94, 2.12), (2.10, 2.12), (1.94, 1.90), (2.10, 1.90), and (2.10, 1.98). (c) Absorptive map of 2DES data in the high energy region at $T = 243$ fs. (d) Selected T-traces for the points marked in (c). Energy coordinates (in eV) of points 1–3 in (c) and (d) are (ω_1, ω_3) = (2.23, 2.13), (2.23, 2.22) and (2.23, 2.32).

that the triplet ESA has strong signals around 450 nm to 550 nm.[53,56,75,76] Although we are not capable of probing the strongest triplet ESA region with our instrument, we are able to capture the lower energy edge of the signal, where there is also some contribution from singlet ESA. T-traces (Figure 5.8d) from this strong ESA confirm the assignment as a mixed triplet and singlet ESA. The ESA intensity is mostly stable at peak 2, which indicates mixed singlet and triplet character as the ultrafast decay of the singlet and rise of the triplet are overlapped and partially negate one another. At peak 3, an ultrafast increase in intensity is observed indicating primarily triplet character. The high energy map also shows a weak and broad GSB (peak 1), which is unchanged over T. Along ω_1, the broadness of this signal originates from the broad absorption in this region. We expect this GSB signal to be equally broad in ω_3, however it is negated by a significant overlap with the ESA at higher ω_3.

Control studies on aqueous solutions of PVA were also performed in both the low and high photon energy ranges. In both photon energy ranges, the absorptive 2DES signal is very weak ($\Delta I/I \sim \mathcal{O}(1)$), and a weak oscillation at around 550 cm^{-1} is observed (Appendix, Figure 5.17). This frequency is similar to the potential non-resonant coherence observed in a control sample of water, and in the low photon energy region the ω_1- and ω_3-dependence is similar in the water and aqueous PVA samples. This frequency does not correspond to a Raman mode of PVA films;[117,118] rather, it is likely to originate from water as the concentration of water is far in excess of the PVA concentration in this sample. The oscillation is very weak, with a maximum amplitude of $\Delta I/I < 1$, and was not detected in the broadband PP data. These background oscillations indicate that care should be taken when interpreting coherence around 550 cm^{-1} in the crystalline TIPS-Pn NP data.

Previous work on polycrystalline TIPS-Pn has found that the vibronic modes of the singlet and triplet manifolds of TIPS-Pn are involved in SF.[28,56] Musser et al. studied polycrystalline TIPS-Pn thin films with PP and pump-dump-probe spectroscopy. They found that vibrational wavepackets in the initially formed singlet state are transferred to the triplet state during SF, accompanied by some shifts in frequency.[56] Bakulin et al. studied polycrystalline TIPS-Pn thin films with 2DES, and were able to directly probe the vibration of a 265 cm^{-1} mode in the triplet pair manifold. They hypothesised that SF was promoted by resonance between the singlet and this vibronic triplet pair state.[28] In the high photon energy range, we expect to see coherence at frequencies matching those observed by Musser et al., but FT of this data set reveals no clear signs of coherence. The beating maps (Appendix, Figure 5.19) show some weak features, but they appear to be spread across the 2D map, reflecting primarily the amplitude of the signal, with little change in appearance as a function of ω_2 and complete insensitivity to the sign of ω_2. The data set presented here is comprised of two interleaved scans, as described in the Methods, Section 2.4. We compared the FT of these two scans (Appendix, Figure 5.20) and found no consistency between the two, indicating that the observed Fourier spectrum for both scans (and hence the composite data set) is primarily noise.

Previous studies have found that the triplet ESA signal of pentacene can be observed with increased intensity by tilting a thin polycrystalline film to 60°, due to the manner in which the crystalline films grow on the substrate, and that the transition dipole of the triplet ESA is oriented along the long axis of the molecule, perpendicular to the 0–0 transition.[75] In NP samples, we have no control over the orientation of the NPs, but we can instead modify the relative polarisation of the pump and probe pulses.

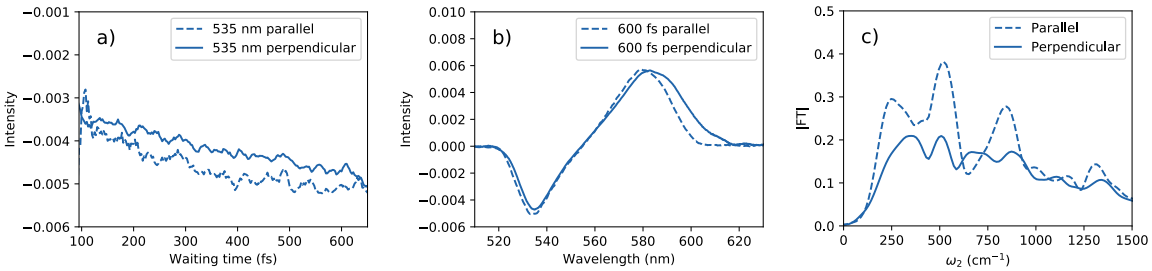

Figure 5.9: (a) Temporal slices at 535 nm, (b) spectral slices at 600 fs, and (c) integrated FT of PP data for crystalline TIPS-Pn NPs with parallel and perpendicular pump/probe polarisation. In (c), data before 165 fs were removed due to the presence of coherent artefacts, and the remaining time window was pre-processed by applying a Butterworth 8th order, 200 cm^{-1} highpass filter, Hann windowing and zero padding to $n = 1024$ before taking the FT.

To ensure that our lack of sensitivity to the proposed triplet coherence is not due to the difference in polarisation between the singlet and triplet transition dipoles, we perform broadband PP experiments with parallel and perpendicular pump and probe polarisations by inserting a half-wave plate at the appropriate angle of rotation into the probe line. We find minor change in the ESA time-dependence and spectral shape between the two pump polarisations, as shown in Figures 5.9a and b. Additionally, there is a lack of coherence in the integrated FT of either polarisation (Figure 5.9c). The decrease in intensity as the frequency increases is simply an artefact of the Savitzky-Golay filter used to smooth the data and decrease the effect of scattering. This result indicates that the observed lack of coherence is not due to the relative orientations of triplet and singlet transition dipoles reducing sensitivity towards triplet ESA.

The lack of observable coherence in the triplet ESA here may simply be a signal-to-noise problem. Crystalline TIPS-Pn NPs have lower extinction coefficients than either amorphous NPs or solutions of TIPS-Pn, so higher concentrations are required for high-quality data. However, increasing the concentration of NPs results in increased NP aggregation, which decreases the data quality as scattering increases with NP size. We attempted to stabilise the NPs at higher concentrations by increasing the relative amount of PVA, such that the PVA might act as a surfactant, however this resulted in no appreciable improvement in data quality. The use of higher amounts of PVA is particularly problematic as the PVA coating the surface of the NPs screens their zeta potentials,[50] which can decrease inter-NP repulsion and decrease colloidal stability. Addition of surfactant was also considered, but not tested due to concerns over interference with the PVA-induced crystallisation process, which is understood to occur on the surface of the NPs.[50] A concentration of 200 ppm in a 1–mm path-length cuvette results in manageable levels of scattering, however the signal is still relatively weak. This weak signal is easily influenced by other sources of noise, the most significant of which is fluctuations in the laser pulse intensity and spectral shape caused by ambient temperature fluctuations, as discussed in the Methods, Section 2.4.1. Additionally, for the high-energy data the 22–fs high-energy laser pulse is likely to be less sensitive to coherence compared to the shorter 12–fs low-energy pulses, due to the increase pulse duration. We therefore hypothesise that low signal-to-noise for oscillating signals may be the explanation for the lack of observable coherence in crystalline TIPS-Pn NPs in the high photon energy region, if such coherence is present.

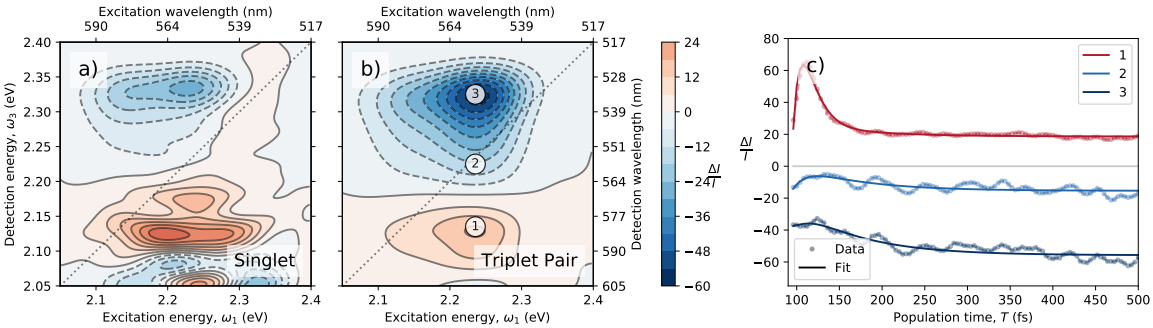

Figure 5.10: Absorptive (a) singlet and (b) triplet pair SAS obtained from global fitting of the 2DES data for crystalline TIPS-Pn NPs in the high photon energy region. (c) Selected T-traces comparing the experimental data to the fitted model. Legend corresponds to points 1–3 marked in (b), with energy coordinates (in eV) of $(\omega_1, \omega_3) = (2.23, 2.13)$, $(2.23, 2.22)$ and $(2.23, 2.32)$.

Despite the lack of observable coherence, we are still able to analyse the kinetics of the high photon energy 2DES data for crystalline TIPS-Pn NPs. To fit this data we use a simple kinetic model capturing the first step of SF, where the excited singlet state converts to the triplet pair intermediate, with rate constant k_{SF} (equation 5.1).

$$\mathrm{S}_1 \xrightarrow{k_{\mathrm{SF}}} {}^1(\mathrm{TT}) \tag{5.1}$$

Since the dissociation of the triplet pair into independent triplets in crystalline TIPS-Pn is known to occur with a time constant of around 5 ps,[53] we exclude triplet pair dissociation in this model. In the high energy range, the longer laser pulse results in strong coherent artefacts persisting up until ≈ 120 fs after excitation. To account for this, data were fit from 95 fs onward, and two additional exponential decay components were supplied to the model, with short lifetimes to account for the rapid evolution of the coherent artefacts. Without the inclusion of these extra components, the model must be fit from later times which may result in a poorly characterised SF rate.

The best-fit SF rate constant from this model is $k_{\mathrm{SF}} = (0.0133 \pm 0.0009)\,\mathrm{fs}^{-1}$ ($\tau_{\mathrm{SF}} = 75$ fs), which is in approximate agreement with previous studies.[28,53,56,75,76] The two exponential components are fit to decays with short time constants of (11.5 ± 0.1) fs and (11.6 ± 0.2) fs. These two rapid decays have DAS with opposite sign, and hence their superposition creates the rapid pulse-like signal observed around $T = 120$ fs at peak 3 of Figure 5.10, which is a remnant of the coherent artefacts observed at early times. As discussed above, these components have no physical significance except to account for coherent artefacts. The singlet and triplet pair SAS are shown in Figure 5.10a and b. The SAS are consistent with the expected appearance based on previous works and the previous assignment of the absorptive signal (Figure 5.8c). Both the singlet and triplet pair maps contain GSB and ESA features, but in the triplet pair map the ESA is stronger and broader. The features at low ω_1 in the singlet SAS are likely to be a residual effect of the coherent artefacts and thus are not physically meaningful. The model describes the data well, as shown in Figure 5.10c, and there is no evidence that a third component (such as independent triplets) is required.

In the low photon energy range, the data again suffer from the signal-to-noise issues discussed above, but the 12–fs pulses are likely to be more sensitive to coherence, if it is present. Indeed, in the low photon energy range, crystalline TIPS-Pn NPs display some weak coherence. The FT are somewhat noisy, however in the beating maps (Figure

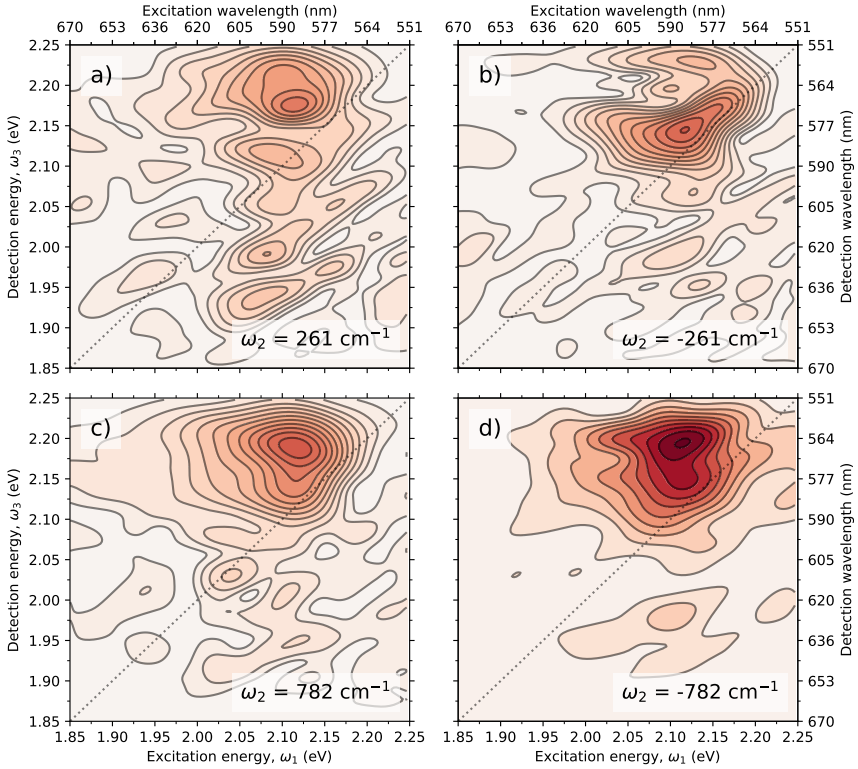

Figure 5.11: Total beating maps at (a)–(b) $\pm 261\,\mathrm{cm}^{-1}$ and (c)–(d) $\pm 782\,\mathrm{cm}^{-1}$ for 2DES of crystalline TIPS-Pn NPs in the low photon energy range. Data were pre-processed as for Figure 5.3. Colour scale corresponds to $|FT|$.

5.11) signals can be observed around $250\,\mathrm{cm}^{-1}$ and in the $600\,\mathrm{cm}^{-1}$ to $1000\,\mathrm{cm}^{-1}$ range around $\omega_1 = 2.10$, $\omega_3 = 2.15\,\mathrm{eV}$ to $2.25\,\mathrm{eV}$. The absorptive spectra in this region exhibit a strong, positive signal that is attributed to GSB (Figure 5.8a). However, in the above discussion on crystalline TIPS-Pn NPs in the high photon energy range, the triplet ESA was identified from $\omega_3 > 2.20\,\mathrm{eV}$ and hence these coherence signals could originate from both the ground state and the triplet pair. To further investigate this coherence, we take a TFT of the 2DES data in this region (Figure 5.12b). The TFT shows that the coherence has non-trivial T-dependence. The mode at approximately $250\,\mathrm{cm}^{-1}$ increases over T, and the coherence from $600\,\mathrm{cm}^{-1}$ to $1000\,\mathrm{cm}^{-1}$ changes frequency over T. The increase in the $250\,\mathrm{cm}^{-1}$ mode is consistent with previous work,[28] in which a mode at $265\,\mathrm{cm}^{-1}$ was identified in the triplet pair states of polycrystalline TIPS-Pn. The growth of this mode in a region where we expect some contribution from triplet-pair ESA indicates that this signal may be associated with the formation of the triplet pair. However, due to low data quality we are hesitant to draw conclusions with regards to the role of coherence in SF in this material based on this preliminary observation. To confirm this finding experimentally, a greater signal-to-noise ratio is required, which could potentially be achieved by moving to a thin film sample rather than the NP suspensions used here. Alternatively, the data could be compared to a quantum mechanical model as was done by Bakulin et al.[28]

Similar to crystalline TIPS-Pn NPs in the high energy region, in the low energy region the coherence is too weak and noisy to be effectively fit using global analysis. Additionally, the models presented so far in this thesis are unable to account for coherence that evolves kinetically, rather than undergoing simple exponential decay.

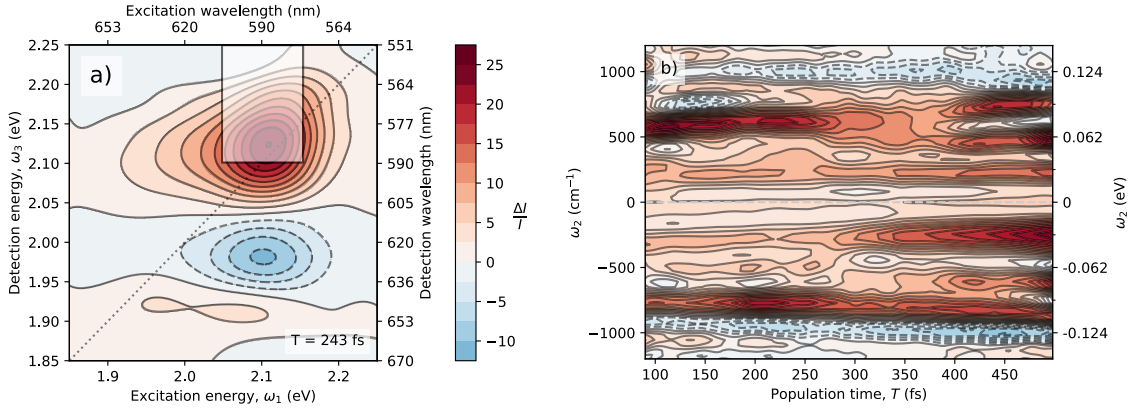

Figure 5.12: (a) Absorptive slice of the 2DES data for crystalline TIPS-Pn NPs at T = 243 fs. (b) Total SPWVT, taken for ω_1 from 2.05 eV to 2.15 eV and ω_3 from 2.10 eV to 2.25 eV and integrated over ω_1 and ω_3. The rectangle in (a) marks the region for the SPWVT in (b). In (b), the colour scheme runs from positive (red) to negative (blue), where negative value are artefacts from the SPWVT. The SPWVT used Gaussian windows along the T and wavenumber axes, with σ = 100 fs for both. Data from T = 90 fs onwards was used and a Butterworth 8th order, 200 cm^{-1} highpass filter were applied prior to taking the SPWVT.

However, we can still fit the non-oscillating data to a model and extract the SF rate and the singlet and triplet pair SAS. We fit to the same SF model as for the high energy region (equation 5.1), and introduce an additional short-lived exponential component to account for the residual effects of coherent artefacts. We fit the data to the model from T = 70 fs onward. The model fits the data reasonably well with a SF rate constant of $k_{\mathrm{SF}} = 0.008\,33\,\mathrm{fs}^{-1}$ ($\tau_{\mathrm{SF}} = 120$ fs), however this rate had to be strongly constrained ($\tau_{SF} \in (75, 120)$ fs) based on the SF rate constant obtained from fitting the same SF model to the high photon energy range data presented above. The SF rate constant fitted to the high photon energy range data is likely to be more reliable as in the high photon energy range there is less overlap between singlet and triplet ESA and hence the ultrafast growth of the triplet ESA is more distinct. The singlet and triplet pair SAS and selected T-traces are shown in Figure 5.13. The singlet and triplet pair SAS are consistent with the prior assignment. The ESA at ω_3 = 1.98 eV appears in both singlet and triplet pair SAS, but is stronger in the singlet SAS, indicating predominantly singlet character. Additionally, the strong diagonal bleach at 2.12 eV is weaker in the triplet pair SAS, reflecting the overlap between triplet pair ESA and GSB in this region of the map.

5.4 Conclusions

In general, over the first 500 fs amorphous TIPS-Pn NPs were found to behave similarly to the dilute solutions of TIPS-Pn discussed in Chapter 4. In the 2DES data, absorptive signals on the diagonals corresponding to bleaching of $|\mathrm{S}_{(1,0)}\rangle$ and $|\mathrm{S}_{(1,1)}\rangle$ were observed, as well as two off-diagonal cross peaks reflecting the shared ground state of these two transitions. An ESA with primarily singlet character was also observed at ω_3 = 2.15 eV. Over time, these signals were largely unchanged apart from weak oscillations, indicating that SF was negligible over the first 500 fs following excitation. FT and global analysis identified coherence associated with five vibrational or vibronic modes at 261 cm^{-1},

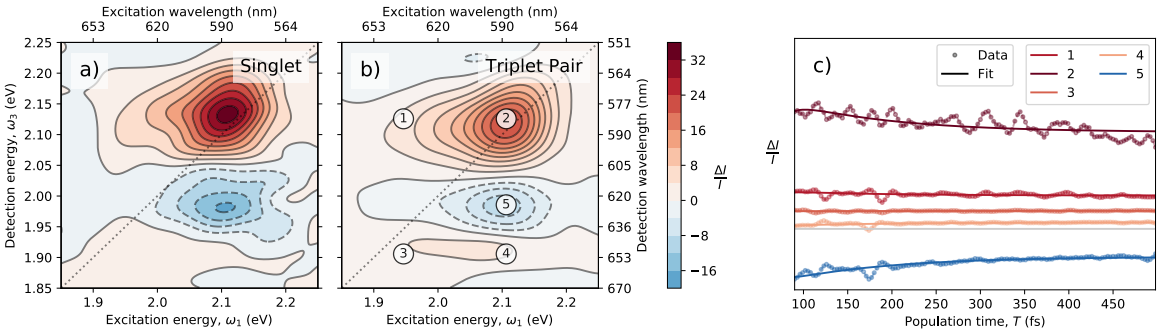

Figure 5.13: Absorptive (a) singlet and (b) triplet pair SAS from global fitting of the 2DES data for crystalline TIPS-Pn NPs in the low energy region to a kinetic model. (c) Selected T-traces comparing the data to the fit, legend corresponds to peaks labelled in (b), traces have been vertically offset for clarity. Energies coordinates (in eV) of points 1–5 in (a) and (b) are: $(\omega_1, \omega_3) = (1.94, 2.12)$, $(2.10, 2.12)$, $(1.94, 1.90)$, $(2.10, 1.90)$, and $(2.10, 1.98)$.

$520\,\mathrm{cm}^{-1}$, $800\,\mathrm{cm}^{-1}$, $1160\,\mathrm{cm}^{-1}$ and $1340\,\mathrm{cm}^{-1}$, with decoherence times in the range 0.89 ps to >2 ps. The relative weakness of the coherence and the large number of modes made assignment by double-sided Feynman diagrams difficult. Despite this, the most dominant signals were able to be assigned. The $1160\,\mathrm{cm}^{-1}$ and $1340\,\mathrm{cm}^{-1}$ CAS were assigned using one GSB and one SE pathway for the positive R map, and a single SE pathway for the positive NR map, indicating that these two modes were found in excited singlet manifold as well as the ground state. The $261\,\mathrm{cm}^{-1}$ mode CAS were partially assigned using GSB, SE and ESA pathways, indicating that this mode was also present in both the ground and singlet excited states. These results indicate that in amorphous NPs, TIPS-Pn has similar vibronic behaviour to isolated molecules in a dilute solution. To investigate the potential involvement of these vibrations in SF a wider T window is required.

2DES data for crystalline TIPS-Pn NPs were collected in both the low and high photon energy ranges. In the low energy range, diagonal GSB of the transitions at 1.92 eV and 2.14 eV was identified, as well as cross peaks indicating the shared ground state of these two transitions. An ESA at 1.98 eV of mixed singlet and triplet character was also observed. In the high photon energy range, a strong ESA was observed from $\omega_3 = 2.20\,\mathrm{eV}$ to 2.35 eV, which was assigned as predominantly triplet in character. Due to poor signal-to-noise, reliable coherence signals were absent in the high photon energy data. In the low photon energy range, coherence was observed around $250\,\mathrm{cm}^{-1}$ and in the $600\,\mathrm{cm}^{-1}$ to $1000\,\mathrm{cm}^{-1}$ region. A TFT of this coherence revealed that the mode around $250\,\mathrm{cm}^{-1}$ increased over T, indicating that it may be associated with the triplet states of TIPS-Pn, as observed in a previous study.[28] Further confirmation of this observation with higher quality data are required, and could potentially be obtained by moving to a thin film sample, which would reduce the signal-to-noise issues associated with scattering from aggregated NPs and the low extinction coefficient of crystalline NPs. In the absence of strong coherence, the high and low energy data sets were both fit to simple SF kinetic models ($S_1 \xrightarrow{k_{SF}} {}^1(TT)$). The resulting singlet and triplet pair SAS were consistent with the assignment above. The rate of SF was found to be $k_{SF} = (0.0133 \pm 0.0009)\,\mathrm{fs}^{-1}$ ($\tau_{SF} = 75\,\mathrm{fs}$) in the high photon energy data set.

5.5 Appendix

5.5.1 Water Control Study

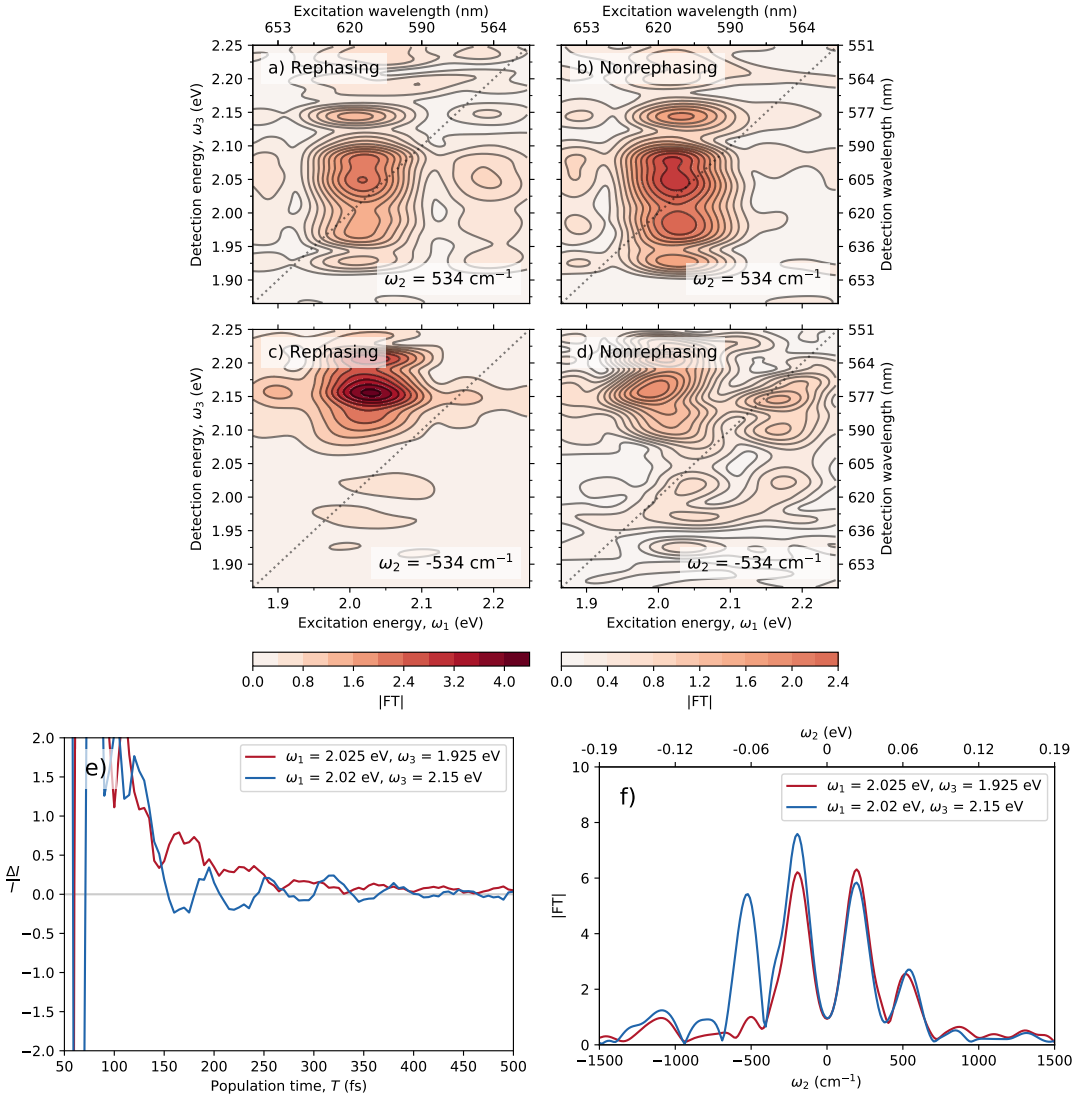

Figure 5.14: Beating maps for water at (a) – (b) $\omega_2 = 534\,\mathrm{cm}^{-1}$ and (c) – (d) $\omega_2 = -534\,\mathrm{cm}^{-1}$ in the low photon energy region. (e) Absorptive T-traces at selected ω_1 and ω_3 and (f) FT of those traces. Removal of data before $T = 90\,\mathrm{fs}$, a Butterworth 8th order, $200\,\mathrm{cm}^{-1}$ highpass filter, Hann windowing and zero padding to $n = 512$ was applied before taking FTs.

5.5.2 Extra CAS for Amorphous TIPS-Pn Nanoparticles, Low Photon Energy

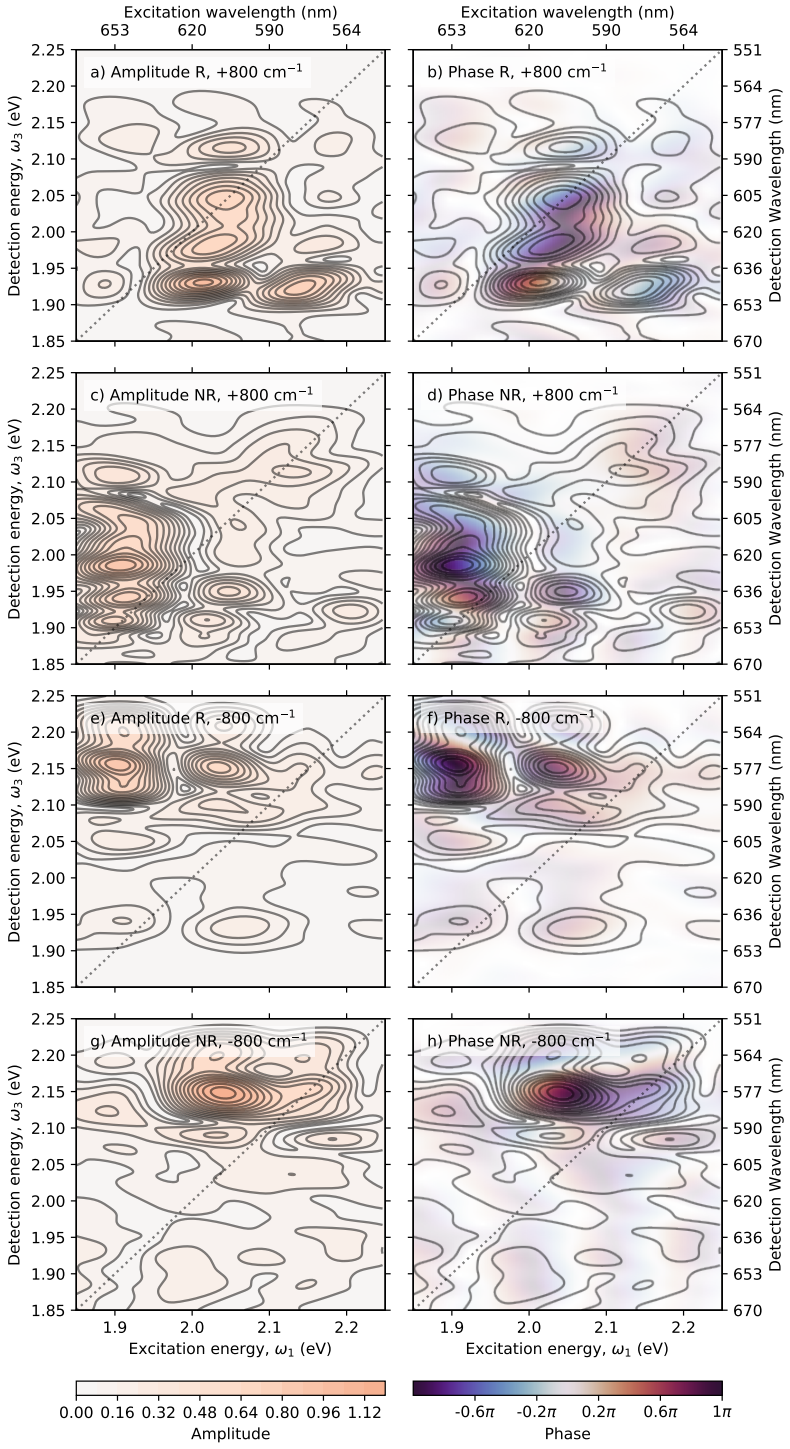

Figure 5.15: Amplitude and phase CAS of component 5 (Table 5.1) from global analysis of amorphous TIPS-Pn NPs. Colour scale is consistent for Figures 5.5–5.7 and 5.15–5.16.

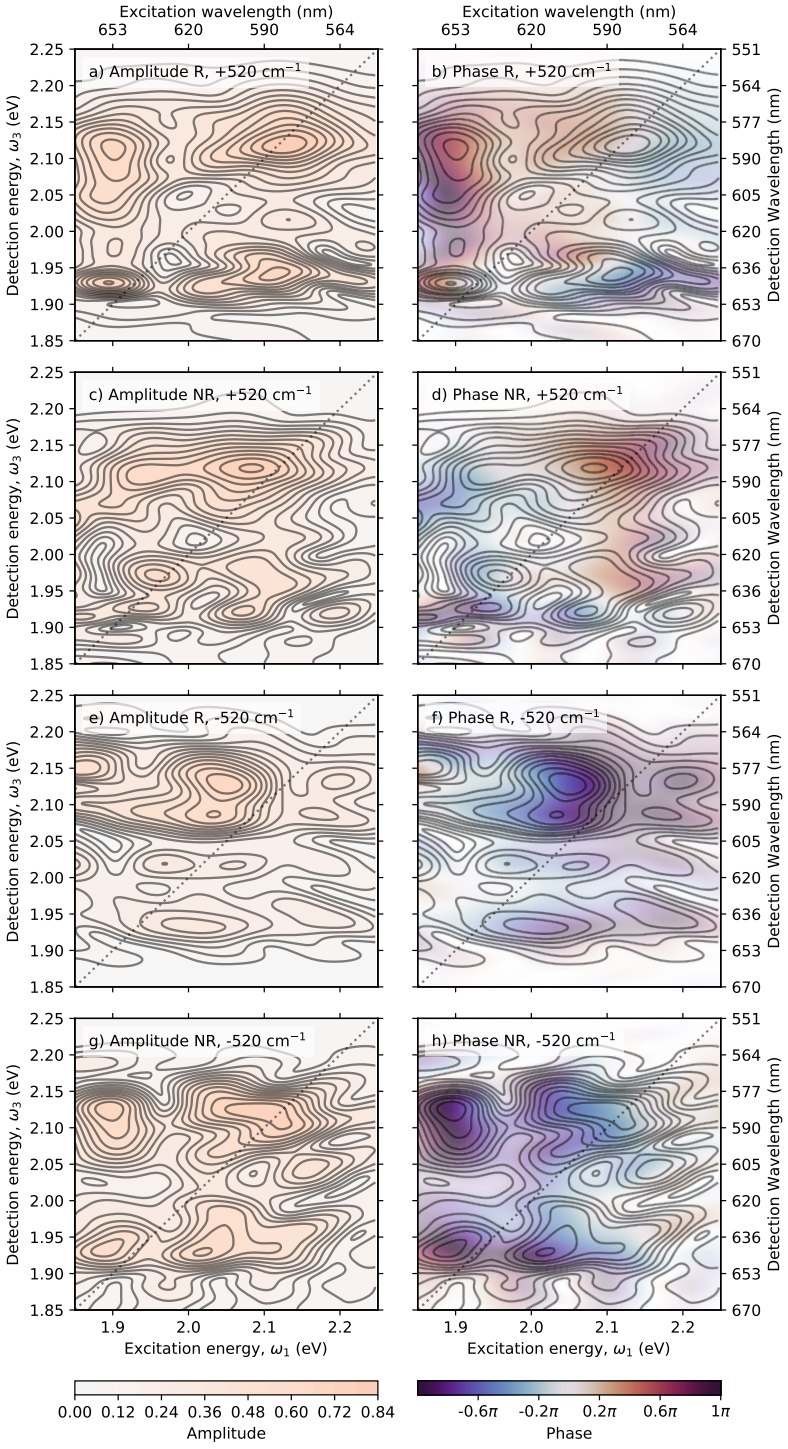

Figure 5.16: Amplitude and phase CAS of component 4 (Table 5.1) from global analysis of amorphous TIPS-Pn NPs. Colour scale is consistent for Figures 5.5–5.7 and 5.15–5.16.

5.5.3 PVA Control Studies

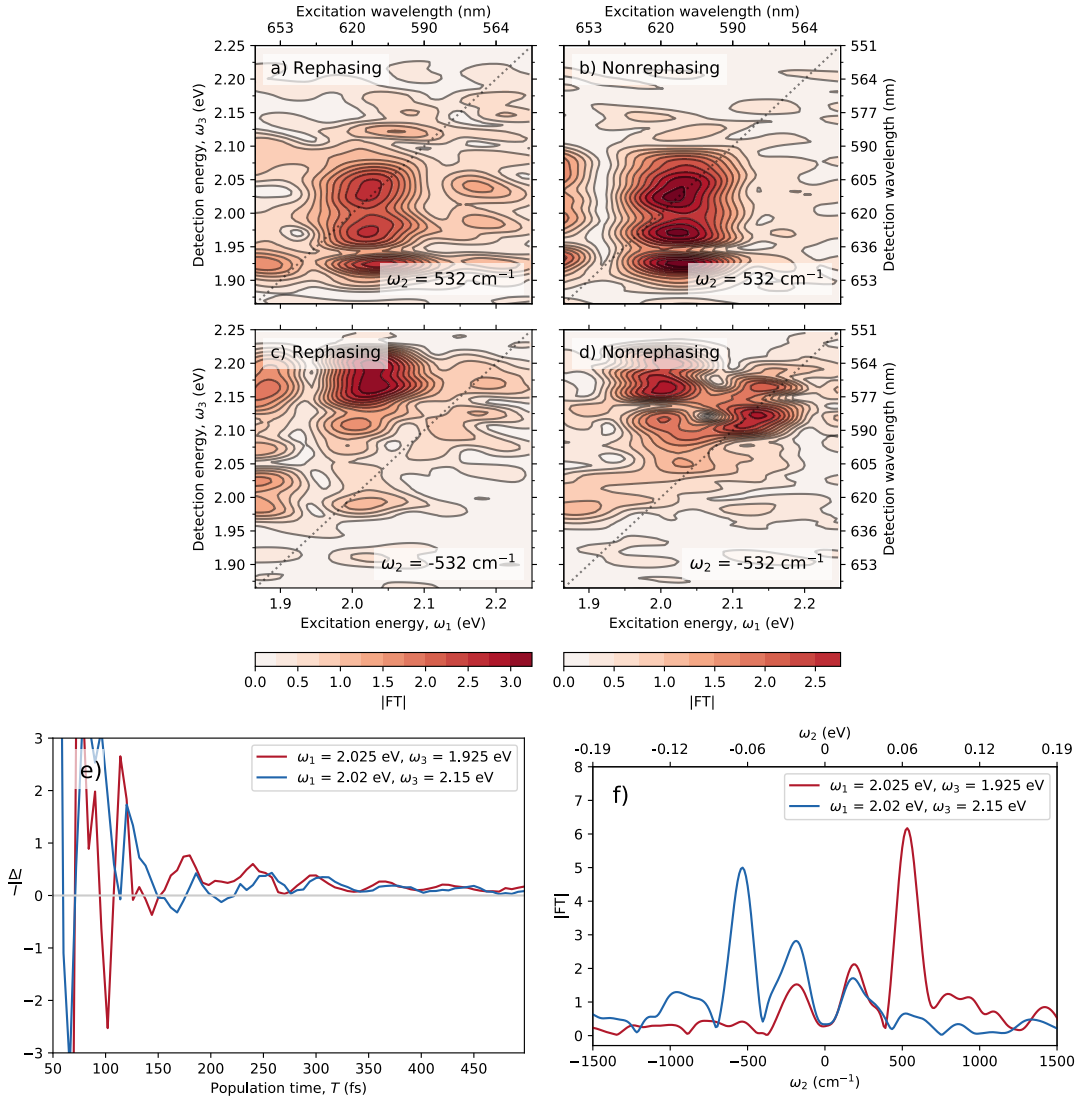

Figure 5.17: Beating maps for aqueous PVA solution at (a) – (b) $\omega_2 = 532\,\mathrm{cm}^{-1}$ and (c) – (d) $\omega_2 = -532\,\mathrm{cm}^{-1}$ in the low photon energy region. (e) Absorptive T-traces at selected ω_1 and ω_3 and (f) FT of those traces. Removal of data before $T = 90\,\mathrm{fs}$, a Butterworth 8th order, $200\,\mathrm{cm}^{-1}$ highpass filter, Hann windowing and zero padding to $n = 512$ was applied before taking FTs.

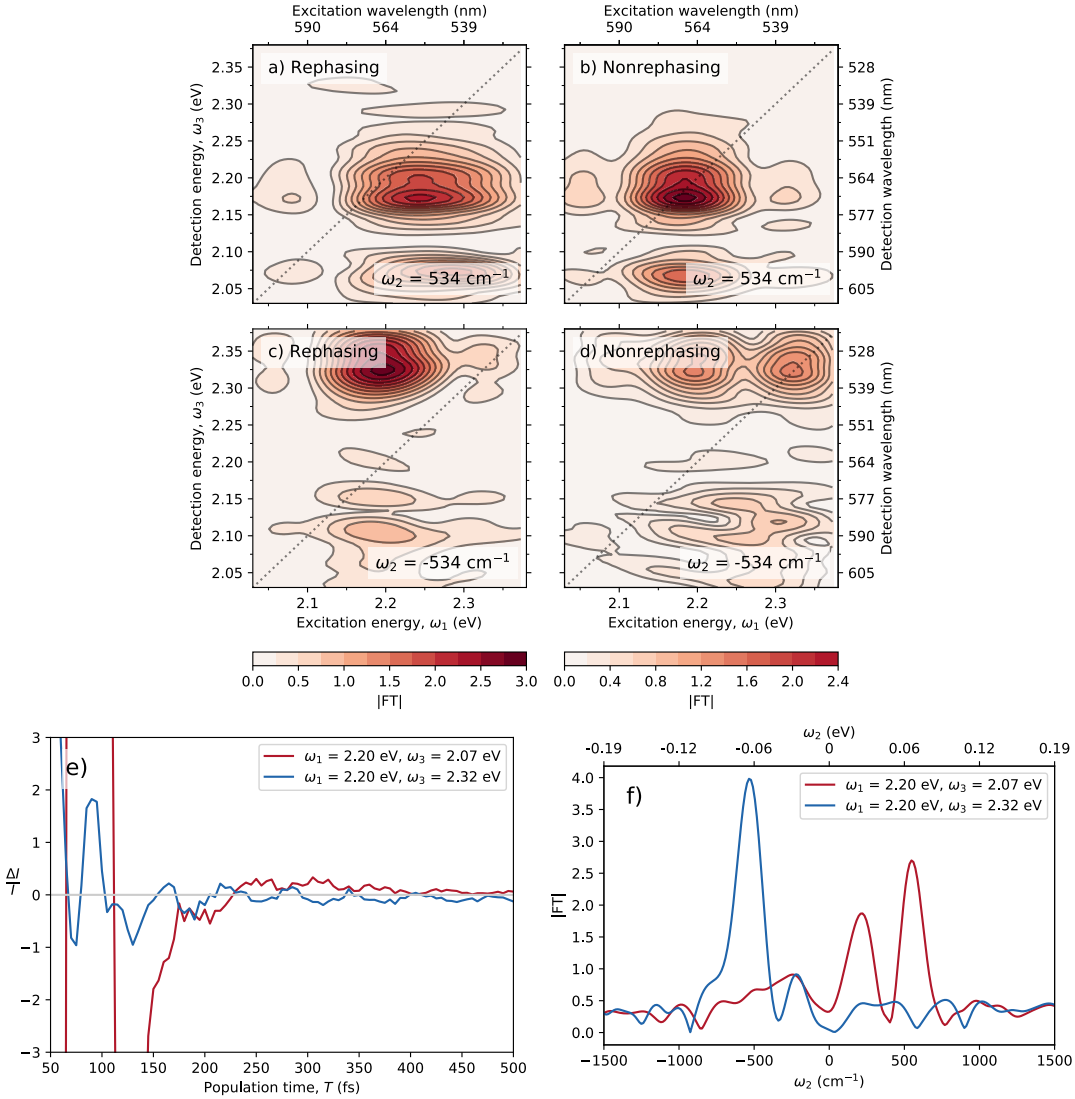

Figure 5.18: Beating maps for aqueous PVA solution at (a) – (b) $\omega_2 = 534\,\mathrm{cm}^{-1}$ and (c) – (d) $\omega_2 = -534\,\mathrm{cm}^{-1}$ in the high photon energy region. (e) Absorptive T-traces at selected ω_1 and ω_3 and (f) FT of those traces. Removal of data before $T = 150\,\mathrm{fs}$, a Butterworth 8th order, $200\,\mathrm{cm}^{-1}$ highpass filter, Hann windowing and zero padding to $n = 512$ was applied before taking FTs.

5.5.4 FT and Beating Maps for Crystalline TIPS-Pn Nanoparticles, High Photon Energy

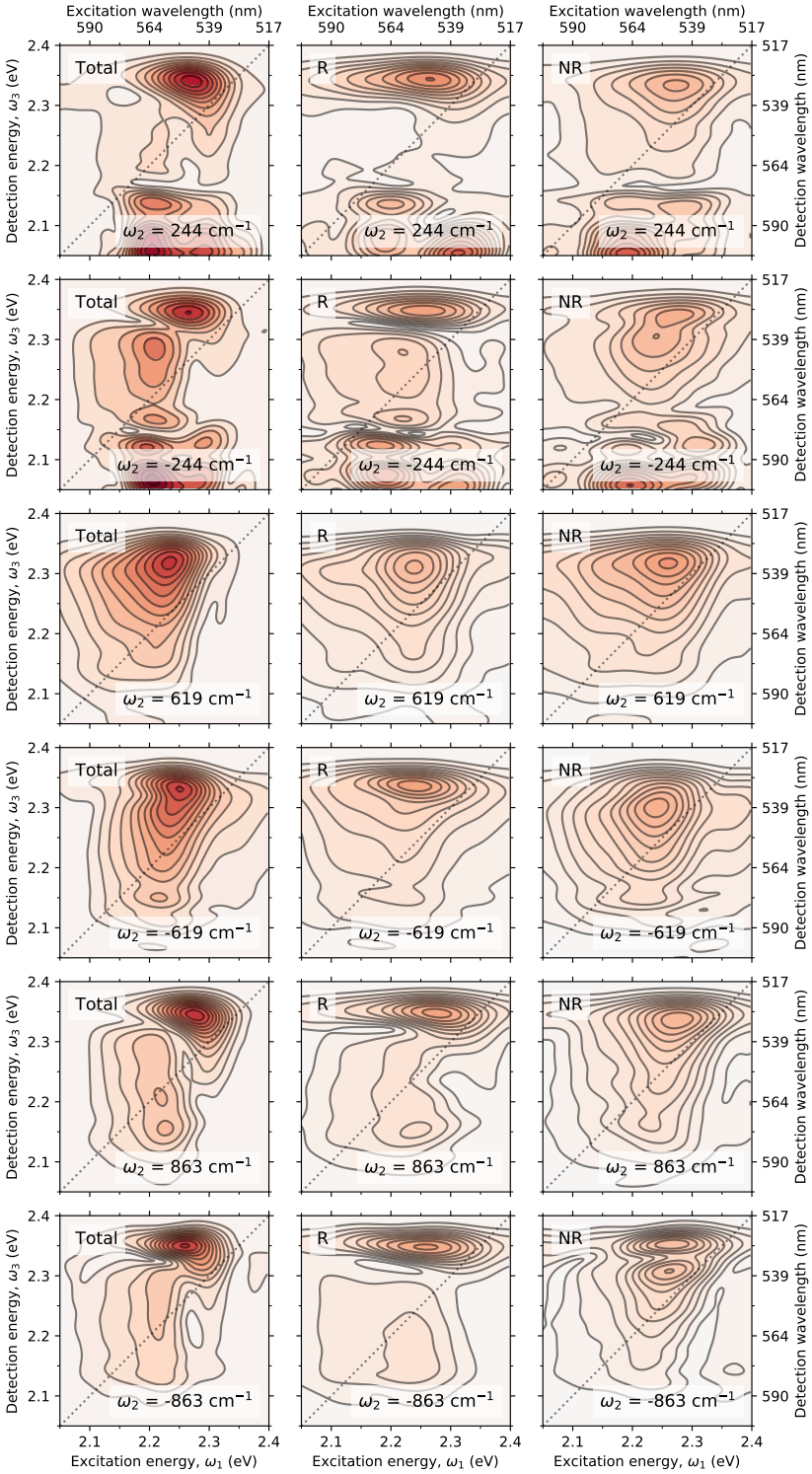

Figure 5.19: Selected total, R and NR (as indicated in the top left) beating maps for 2DES data for crystalline TIPS-Pn NPs with high photon energy pulses. Frequency is given in the bottom right corner of each frame. Removal of data before $T = 120\,\mathrm{fs}$, a Butterworth 8th order, $200\,\mathrm{cm}^{-1}$ highpass filter, Hann windowing and zero padding to $n = 512$ was applied before taking the FT. Colour scale corresponds to $|FT|$.

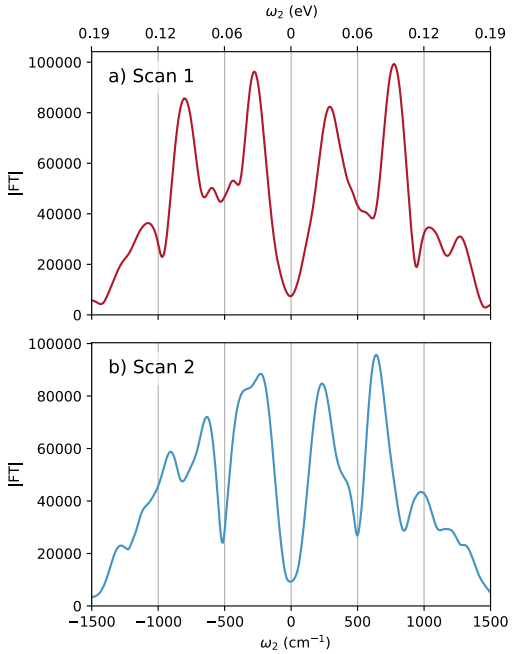

Figure 5.20: Total integrated FT of two 2DES data sets for crystalline TIPS-Pn NPs in the high photon energy region. Data were pre-processed as for Figure 5.19.

CHAPTER 6
Conclusion

In this thesis, two topics were discussed: data analysis of 2DES data using a model system as an example (Chapter 3), and coherence and singlet fission in TIPS-Pn solutions (Chapter 4) and NPs (Chapter 5). In chapter 3, a flexible data analysis framework for the interpretation of 2DES data was presented and used to analyse data from a model two-level, single-mode system: a solution of cresyl violet. The framework included three analytical techniques, FT, TFT, and global analysis, arranged in that order such as to move from model independent to model dependent methods. Interpretation of the results from this analysis framework was supported by prediction of theoretical coherence pathways using double-sided Feynman diagrams. Some improvements over existing implementations of these methods were proposed. Hilbert transforms were used to split the data into analytic and antianalytic components, which allowed TFTs with double-sided frequency axes to be computed. Additionally, global analysis was used to fit the data to a model containing concentration curves generated by a kinetic model in addition to complex multi-exponential components to account for coherence. A method for generating such models for arbitrary complex kinetic schemes and any number of coherence frequencies was proposed.

This analysis framework was used to investigate 2DES data for cresyl violet, a model two-level system with a single vibrational mode in the frequency region available. In the absorptive 2DES data, signals corresponding to GSB and SE were observed, as well as two ultrafast relaxation processes which were assigned as decorrelation of ω_1 and ω_3 due to environmental relaxation, and dynamic Stokes shift. Strong coherence was also observed, which was identified by FT to be concentrated primarily in the R data at $600\,\mathrm{cm}^{-1}$. TFTs showed that this coherence was long-lived, exhibiting a minor variation in intensity over the available T window. Global analysis was used to fit the data to a simple kinetic model of the form A $\xrightarrow{k_1}$ B. Coherence was incorporated into this model using complex exponential components. The model described the data well, returning SAS for species A and B, the rate constant k_1, the coherence frequencies and dephasing rates, and amplitude and phase CAS for the coherence components. Species A and B were found to represent cresyl violet before and after the two relaxation processes described above, respectively. The combined relaxation rate constant was hence represented by k_1, and $1/k_1$ was found to be $\approx 100\,\mathrm{fs}$. In future work, a more sophisticated kinetic scheme could be used to deconvolute the two relaxation processes and determine their rate constants with higher accuracy. The coherence was well described by a pair of complex multi-exponentials with frequencies of $\pm 612\,\mathrm{cm}^{-1}$ and lifetimes of 600 fs. The amplitude CAS for these coherence components were nearly identical to the beating maps generated from FT. Double-sided Feynman diagrams were used to predict theoretical coherence locations based on a model with the $612\,\mathrm{cm}^{-1}$ mode in both the ground and excited states. These locations were highly consistent with the ω_1- and ω_3-dependence observed in the CAS.

The data analysis framework proposed is rather flexible and general, however it may not be suitable in the case where the coherence has a complicated T-dependence

that is not well described by a multi-exponential decay. For example, such complex T-dependence could be found in a system where coherence is transferred from one species to another, potentially accompanied by a change in frequency- or energy- dependence. In these cases it would be advantageous to use global analysis to describe the T-dependence of the coherence. This analysis could be done by using a general kinetic model to describe the T-dependence of the coherence strength, and using the concentration curves rather than exponential decays as the pre-factor to the sinusoidal coherence components in the model. The development of such a model could be aided by using TFTs to generate T-resolved beating maps, which are a model-independent measure of the T-dependence of coherence across the entire 2D map.[119]

We then used the analysis framework to investigate the model SF chromophore TIPS-Pn, beginning in Chapter 4 with PP and 2DES studies of dilute solutions of TIPS-Pn. In dilute solutions, SF was minimal, allowing characterisation of the singlet states of TIPS-Pn in the absence of SF. Broadband PP spectroscopy was used to investigate dilute solutions of TIPS-Pn in three solvents: toluene, THF and acetone. In all three solvents, well-known singlet GSB and ESA signals were observed, with no change in average intensity observed over time. However, strong and highly solvent-dependent coherence was observed at a number of frequencies over the entire T and wavelength window available. As a control, the PP experiments were repeated for samples of the three solvents without TIPS-Pn. These control studies showed that the solvent-dependent coherence observed the samples containing TIPS-Pn was accounted for entirely by the long-lived, non-resonant coherence of the solvents, which was observed at frequencies highly consistent with the Raman spectra of each solvent. Modes at approximately $265\,\mathrm{cm}^{-1}$, $800\,\mathrm{cm}^{-1}$, $1150\,\mathrm{cm}^{-1}$ and $1200\,\mathrm{cm}^{-1}$ were found to be common in multiple samples containing TIPS-Pn and unaccounted for by the solvent, and were hence assigned to TIPS-Pn. These modes were found to be present in both the ESA and GSB region, indicating that they are found at similar frequencies in both the ground and first singlet excited state manifolds.

The coherence of THF was found to overlap the least with the coherence of TIPS-Pn, so THF was used as the solvent for 2DES studies of TIPS-Pn in solution. As with the PP experiments, 2DES was also performed on a sample of THF without TIPS-Pn as a control. As with the PP, coherence was observed at a single frequency around $915\,\mathrm{cm}^{-1}$, corresponding to a Raman-active vibrational mode of THF. FT and global analysis were used to study the ω_1- and ω_3-dependence of this non-resonant solvent coherence; it was found to be present in at both positive and negative frequency in the R and NR data, with a lifetime of $(\pm 860 \pm 50)\,\mathrm{fs}$. The ω_1- and ω_3-dependence was found to be non-trivial, and was rationalised by drawing inspiration from CARS and CSRS, coherent four-wave mixing Raman spectroscopic techniques. In CARS and CSRS, non-resonant coherence is established through a Raman-like mechanism involving two virtual states. Signals corresponding to CARS- and CSRS-like coherence pathways were observed in the THF 2DES data, but these two pathways only account for some of the observed the non-resonant coherence. In the existing literature, solvent coherence is often ignored and assumed to have no specific ω_1- and ω_3-dependence.[25,99] Here, the solvent coherence has strong ω_1- and ω_3-dependence that can be broadly rationalised by Raman-like pathways involving at least two virtual states. This phenomenon warrants further study to confirm this proposed mechanism and determine the conditions under which non-resonant solvent coherence can be significant. This is particularly relevant since many common organic solvents have Raman modes in the frequency region observed

by 2DES.

Having characterised the coherence of the solvent, we moved on to 2DES of TIPS-Pn in THF. The main features of the absorptive maps were assigned as diagonal GSB of the 0–0 and 0–1 transitions, a strong cross peak indicating correlation between those two transitions, and a singlet ESA at 2.15 eV. Over T, only minor changes in the intensity of these signals were observed, aside from oscillations at frequencies of 295 cm^{-1}, 520 cm^{-1}, 781 cm^{-1}, 940 cm^{-1}, 1159 cm^{-1} and 1341 cm^{-1}. The coherence had lifetimes in the range of 0.5 ps to 1.5 ps, although we expect that a longer T window would be required to better characterise these lifetimes. The 940 cm^{-1} mode was attributed to THF and the CAS were similar for this mode in the presence and absence of TIPS-Pn. The remaining modes were attributed to vibrational or vibronic coherence of TIPS-Pn. An attempt was made to use double-sided Feynman diagrams to assign the CAS and confirm the presence of the observed coherence in the ground or singlet excited states. However, this was complicated by the weakness of the coherence and the presence of many vibrational modes. We were able to assign the strongest signals in the 295 cm^{-1}, 1159 cm^{-1} and 1341 cm^{-1} CAS using GSB and SE pathways. This result, combined with the high quality PP data, indicated that the vibronic structures of the ground state and the first excited singlet state of TIPS-Pn are largely similar.

In Chapter 5, we investigated SF and coherence in TIPS-Pn in the solid phase, in the form of amorphous and crystalline NPs. Amorphous TIPS-Pn NPs were found to be largely similar to TIPS-Pn in solution. Diagonal GSB of the 0–0 and 0–1 transitions was observed, as well as cross peaks indicating the shared ground state of these transitions. Singlet ESA was also observed around 2.15 eV. Over T, these signals again showed only minor changes in intensity aside from oscillations. In these amorphous NPs the SF is known to be slow compared to the available T window of the instrument[50,51,54] and hence a stable singlet population over the first 500 fs was expected. Coherence was observed at frequencies of 261 cm^{-1}, 520 cm^{-1}, 800 cm^{-1}, 1160 cm^{-1} and 1340 cm^{-1}, with lifetimes in the 0.9 ps to 2.9 ps range. As with TIPS-Pn in solution, this coherence was assigned as vibrational and vibronic coherence in the ground and singlet states of TIPS-Pn. The CAS were found to be complicated due to the large number of modes, however the 1150 cm^{-1}, 1130 cm^{-1} and 261 cm^{-1} CAS were able to be assigned with a combination of GSB, SE and ESA coherence pathways. For these modes, some signals were only able to be assigned using SE or ESA pathways, indicating that these modes are present in the singlet excited state. Additionally, the CAS were found to be quite similar to the CAS of TIPS-Pn in THF. Hence, in amorphous TIPS-Pn NPs, the coherence within the singlet states of TIPS-Pn is largely similar to isolated TIPS-Pn molecules in dilute solutions. To determine the effect, if any, of these modes on SF in amorphous TIPS-Pn NPs, a wider T-window would be required.

In crystalline TIPS-Pn NPs, 2DES data were collected in both a high and low photon energy region in order to observe the triplet pair ESA at $\omega_3 > 2.20$ eV. In the high photon energy region, the map was dominated by a strong ESA of primarily triplet character. A simple SF kinetic model was fit to the data ($S_1 \xrightarrow{k_{SF}} {}^1(TT)$), with a best-fit SF time constant of $\tau_{SF} = 75$ fs. Unfortunately, due to poor signal-to-noise, it was unclear if coherence was present in the high photon energy region. In the low photon energy region, we observed diagonal GSB assigned to the bleaching of the transitions at 1.92 eV and 2.14 eV, and cross peaks indicating the shared ground state of these transitions. A weak ESA of mixed singlet and triplet character at 1.98 eV was also observed. In the low photon energy region, the coherence of crystalline TIPS-Pn was

weak and close to the noise floor. We used FT and TFT to observe a mode around $250\,\mathrm{cm}^{-1}$ that increased over T in a region of triplet ESA. This result was consistent with the findings of Bakulin et al.,[28] where a vibronic mode at $265\,\mathrm{cm}^{-1}$ was identified in the triplet pair manifold. However, higher quality data would be required to confirm this observation, which is achievable by moving to a thin film sample, which reduces the issues associated with scattering and low extinction coefficients for crystalline TIPS-Pn NPs.

References

[1] Hybl, J. D.; Albrecht, A. W.; Faeder, S. M. G.; Jonas, D. M. Two-Dimensional Electronic Spectroscopy. *Chem. Phys. Lett.* **1998**, *297*, 307–313.

[2] Hybl, J. D.; Albrecht Ferro, A.; Jonas, D. M. Two-Dimensional Fourier Transform Electronic Spectroscopy. *J. Chem. Phys.* **2001**, *115*, 6606–6622.

[3] Song, Y.; Clafton, S. N.; Pensack, R. D.; Kee, T. W.; Scholes, G. D. Vibrational Coherence Probes the Mechanism of Ultrafast Electron Transfer in Polymer-Fullerene Blends. *Nat. Commun.* **2014**, *5*, 4933.

[4] De Sio, A.; Troiani, F.; Maiuri, M.; Réhault, J.; Sommer, E.; Lim, J.; Huelga, S. F.; Plenio, M. B.; Rozzi, C. A.; Cerullo, G.; Molinari, E.; Lienau, C. Tracking the Coherent Generation of Polaron Pairs in Conjugated Polymers. *Nat. Commun.* **2016**, *7*, 1–8.

[5] Mandal, A.; Chen, M.; Foszcz, E. D.; Schultz, J. D.; Kearns, N. M.; Young, R. M.; Zanni, M. T.; Wasielewski, M. R. Two-Dimensional Electronic Spectroscopy Reveals Excitation Energy-Dependent State Mixing during Singlet Fission in a Terrylenediimide Dimer. *J. Am. Chem. Soc.* **2018**, *140*, 17907–17914.

[6] Lee, Y.; Das, S.; Malamakal, R. M.; Meloni, S.; Chenoweth, D. M.; Anna, J. M. Ultrafast Solvation Dynamics and Vibrational Coherences of Halogenated Boron-Dipyrromethene Derivatives Revealed through Two-Dimensional Electronic Spectroscopy. *J. Am. Chem. Soc.* **2017**, *139*, 14733–14742.

[7] Kobayashi, Y.; Chuang, C.-H.; Burda, C.; Scholes, G. D. Exploring Ultrafast Electronic Processes of Quasi-Type II Nanocrystals by Two-Dimensional Electronic Spectroscopy. *J. Phys. Chem. C* **2014**, *118*, 16255–16263.

[8] Seiler, H.; Palato, S.; Sonnichsen, C.; Baker, H.; Kambhampati, P. Seeing Multiexcitons through Sample Inhomogeneity: Band-edge Biexciton Structure in Cdse Nanocrystals Revealed by Two-dimensional Electronic Spectroscopy. *Nano Lett.* **2018**, *18*, 2999–3006.

[9] Cassette, E.; Dean, J. C.; Scholes, G. D. Two-Dimensional Visible Spectroscopy For Studying Colloidal Semiconductor Nanocrystals. *Small* **2016**, *12*, 2234–2244.

[10] Wong, C. Y.; Alvey, R. M.; Turner, D. B.; Wilk, K. E.; Bryant, D. A.; Curmi, P. M.; Silbey, R. J.; Scholes, G. D. Electronic Coherence Lineshapes Reveal Hidden Excitonic Correlations in Photosynthetic Light Harvesting. *Nat. Chem.* **2012**, *4*, 396.

[11] Ostroumov, E. E.; Mulvaney, R. M.; Cogdell, R. J.; Scholes, G. D. Broadband 2D Electronic Spectroscopy Reveals a Carotenoid Dark State in Purple Bacteria. *Science* **2013**, *340*, 52–56.

[12] Wang, L.; Allodi, M. A.; Engel, G. S. Quantum Coherences Reveal Excited-State Dynamics in Biophysical Systems. *Nat. Rev. Chem.* **2019**, *3*, 477–490.

[13] Lambrev, P. H.; Akhtar, P.; Tan, H.-S. Insights into the Mechanisms and Dy-

namics of Energy Transfer in Plant Light-Harvesting Complexes from Two-Dimensional Electronic Spectroscopy. *Biochem. Biophys. Acta—Bioenerg.* **2019**,

[14] Dostál, J.; Pšenčík, J.; Zigmantas, D. In Situ Mapping of the Energy Flow through the Entire Photosynthetic Apparatus. *Nat. Chem.* **2016**, *8*, 705.

[15] Zigmantas, D.; Read, E. L.; Mančal, T.; Brixner, T.; Gardiner, A. T.; Cogdell, R. J.; Fleming, G. R. Two-Dimensional Electronic Spectroscopy of the B800–B820 Light-Harvesting Complex. *Proc. Natl. Acad. Sci.* **2006**, *103*, 12672–12677.

[16] Brixner, T.; Stenger, J.; Vaswani, H. M.; Cho, M.; Blankenship, R. E.; Fleming, G. R. Two-Dimensional Spectroscopy of Electronic Couplings in Photosynthesis. *Nature* **2005**, *434*, 625–628.

[17] Fuller, F. D.; Ogilvie, J. P. Experimental Implementations of Two-dimensional Fourier Transform Electronic Spectroscopy. *Ann. Rev. Phys. Chem.* **2015**, *66*, 667–690.

[18] Tollerud, J. O.; Davis, J. A. Coherent Multi-Dimensional Spectroscopy: Experimental Considerations, Direct Comparisons and New Capabilities. *Prog. Quantum Electron.* **2017**, *55*, 1–34.

[19] Tapping, P. C.; Song, Y.; Kobayashi, Y.; Scholes, G. D.; Kee, T. W. Two-Dimensional Electronic Spectroscopy Using Rotating Optical Flats. *J. Phys. Chem. A* **2020**, *124*, 1053–1061.

[20] Jansen, T. l. C.; Saito, S.; Jeon, J.; Cho, M. Theory of Coherent Two-Dimensional Vibrational Spectroscopy. *J. Chem. Phys.* **2019**, *150*, 100901.

[21] Turner, D. B.; Stone, K. W.; Gundogdu, K.; Nelson, K. A. Three-Dimensional Electronic Spectroscopy of Excitons in GaAs Quantum Wells. *J. Chem. Phys.* **2009**, *131*, 144510.

[22] Cundiff, S. T. Optical Three Dimensional Coherent Spectroscopy. *Phys. Chem. Chem. Phys.* **2014**, *16*, 8193–8200.

[23] Volpato, A.; Collini, E. Time-Frequency Methods for Coherent Spectroscopy. *Opt. Express* **2015**, *23*, 20040–20050.

[24] Volpato, A.; Collini, E. Optimization and Selection of Time-Frequency Transforms for Wave-Packet Analysis in Ultrafast Spectroscopy. *Opt. Express* **2019**, *27*, 2975–2987.

[25] Volpato, A.; Bolzonello, L.; Meneghin, E.; Collini, E. Global Analysis of Coherence and Population Dynamics in 2D Electronic Spectroscopy. *Opt. Express* **2016**, *24*, 24773–24785.

[26] Mukamel, S. *Principles of Nonlinear Optical Spectroscopy*; Oxford University Press on Demand, 1999.

[27] Seibt, J.; Pullerits, T. Beating Signals in 2D Spectroscopy: Electronic or Nuclear Coherences? Application to a Quantum Dot Model System. *J. Phys. Chem. C* **2013**, *117*, 18728–18737.

[28] Bakulin, A. A.; Morgan, S. E.; Kehoe, T. B.; Wilson, M. W.; Chin, A. W.; Zigmantas, D.; Egorova, D.; Rao, A. Real-Time Observation of Multiexcitonic

States in Ultrafast Singlet Fission using Coherent 2D Electronic Spectroscopy. *Nat. Chem.* **2016**, *8*, 16–23.

[29] Song, Y.; Hellmann, C.; Stingelin, N.; Scholes, G. D. The Separation of Vibrational Coherence from Ground-and Excited-Electronic States in P3HT Film. *J. Chem. Phys.* **2015**, *142*, 212410.

[30] Paleček, D.; Edlund, P.; Westenhoff, S.; Zigmantas, D. Quantum Coherence as a Witness of Vibronically Hot Energy Transfer in Bacterial Reaction Center. *Sci. Adv.* **2017**, *3*, e1603141.

[31] Butkus, V.; Zigmantas, D.; Valkunas, L.; Abramavicius, D. Vibrational Vs. Electronic Coherences in 2D Spectrum of Molecular Systems. *Chem. Phys. Lett.* **2012**, *545*, 40–43.

[32] Kreisbeck, C.; Kramer, T.; Aspuru-Guzik, A. Disentangling Electronic and Vibronic Coherences in Two-Dimensional Echo Spectra. *J. Phys. Chem. B* **2013**, *117*, 9380–9385.

[33] Kobayashi, T.; Saito, T.; Ohtani, H. Real-Time Spectroscopy of Transition States in Bacteriorhodopsin During Retinal Isomerization. *Nature* **2001**, *414*, 531–534.

[34] Torrence, C.; Compo, G. P. A Practical Guide to Wavelet Analysis. *Bull. Am. Meterol. Soc.* **1998**, *79*, 61–78.

[35] Prior, J.; Castro, E.; Chin, A. W.; Almeida, J.; Huelga, S. F.; Plenio, M. B. Wavelet Analysis of Molecular Dynamics: Efficient Extraction of Time-Frequency Information in Ultrafast Optical Processes. *J. Chem. Phys.* **2013**, *139*, 224103.

[36] Claasen, T.; Mecklenbrauker, W. The Wigner Distribution—A Tool for Time-Frequency Signal Analysis. *Philips J. Res.* **1980**, *35*, 217–250.

[37] Novoderezhkin, V. I.; Romero, E.; Prior, J.; van Grondelle, R. Exciton-Vibrational Resonance and Dynamics of Charge Separation in the Photosystem II Reaction Center. *Phys. Chem. Chem. Phys.* **2017**, *19*, 5195–5208.

[38] Bolzonello, L.; Polo, A.; Volpato, A.; Meneghin, E.; Cordaro, M.; Trapani, M.; Fortino, M.; Pedone, A.; Castriciano, M. A.; Collini, E. Two-Dimensional Electronic Spectroscopy Reveals Dynamics and Mechanisms of Solvent-Driven Inertial Relaxation in Polar BODIPY Dyes. *J. Phys. Chem. Lett.* **2018**, *9*, 1079–1085.

[39] Beechem, J. M.; Ameloot, M.; Brand, L. Global and Target Analysis of Complex Decay Phenomena. *Instrum. Sci. Technol.* **1985**,

[40] Beechem, J. M. A Second Generation Global Analysis Program for the Recovery of Complex Inhomogeneous Fluorescence Decay Kinetics. *Chem. Phys. Lipids* **1989**, *50*, 237–251.

[41] Van Stokkum, I. H.; Larsen, D. S.; Van Grondelle, R. Global and Target Analysis of Time-Resolved Spectra. *Biochem. Biophys. Acta—Bioenerg.* **2004**, *1657*, 82–104.

[42] Hendler, R. W.; Shrager, R. I. Deconvolutions Based on Singular Value Decomposition and the Pseudoinverse: a Guide for Beginners. *J. Biochem. Bioph. Meth.* **1994**, *28*, 1–33.

[43] O'leary, D. P.; Rust, B. W. Variable Projection for Nonlinear Least Squares

Problems. *Comput. Optim. Appl.* **2013**, *54*, 579–593.

[44] Golub, G.; Pereyra, V. Separable Nonlinear Least Squares: the Variable Projection Method and its Applications. *Inverse Probl.* **2003**, *19*, R1.

[45] Mullen, K. M.; Van Stokkum, I. H. The Variable Projection Algorithm in Time-Resolved Spectroscopy, Microscopy and Mass Spectrometry Applications. *Numer. Algorithms* **2009**, *51*, 319–340.

[46] Penrose, R. A Generalized Inverse for Matrices. Mathematical Proceedings of the Cambridge Philosophical Society. 1955; pp 406–413.

[47] Duan, H.-G.; Prokhorenko, V. I.; Wientjes, E.; Croce, R.; Thorwart, M.; Miller, R. D. Primary Charge Separation in the Photosystem II Reaction Center Revealed by a Global Analysis of the Two-Dimensional Electronic Spectra. *Sci. Rep.* **2017**, *7*, 1–9.

[48] Perlik, V.; Lincoln, C.; Šanda, F.; Hauer, J. Distinguishing Electronic and Vibronic Coherence in 2D Spectra by their Temperature Dependence. *J. Phys. Chem. Lett.* **2014**, *5*, 404–407.

[49] Walker, B. J.; Musser, A. J.; Beljonne, D.; Friend, R. H. Singlet Exciton Fission in Solution. *Nat. Chem.* **2013**, *5*, 1019.

[50] Hudson, R. J.; de la Perrelle, J. M.; Pensack, R. D.; Kudisch, B.; Scholes, G. D.; Huang, D. M.; Kee, T. W. Organizing Crystalline Functionalized Pentacene using Periodicity of Poly (Vinyl Alcohol). *J. Phys. Chem. Lett.* **2019**, *11*, 516–523.

[51] Stuart, A. N.; Tapping, P. C.; Schrefl, E.; Huang, D. M.; Kee, T. W. Controlling the Efficiency of Singlet Fission in TIPS-Pentacene/Polymer Composite Nanoparticles. *J. Phys. Chem. C* **2019**, *123*, 5813–5825.

[52] Tayebjee, M. J.; Schwarz, K. N.; MacQueen, R. W.; Dvoˇ rák, M.; Lam, A. W.; Ghiggino, K. P.; McCamey, D. R.; Schmidt, T. W.; Conibeer, G. J. Morphological Evolution and Singlet Fission in Aqueous Suspensions of TIPS-Pentacene Nanoparticles. *J. Phys. Chem. C* **2016**, *120*, 157–165.

[53] Pensack, R. D.; Grieco, C.; Purdum, G. E.; Mazza, S. M.; Tilley, A. J.; Ostroumov, E. E.; Seferos, D. S.; Loo, Y.-L.; Asbury, J. B.; Anthony, J. E.; ; Scholes, G. D. Solution-Processable, Crystalline Material for Quantitative Singlet Fission. *Mater. Horiz.* **2017**, *4*, 915–923.

[54] Pensack, R. D.; Tilley, A. J.; Parkin, S. R.; Lee, T. S.; Payne, M. M.; Gao, D.; Jahnke, A. A.; Oblinsky, D. G.; Li, P.-F.; Anthony, J. E.; Seferos, D. S.; Scholes, G. D. Exciton Delocalization Drives Rapid Singlet Fission in Nanoparticles of Acene Derivatives. *J. Am. Chem. Soc.* **2015**, *137*, 6790–6803.

[55] Pensack, R. D.; Tilley, A. J.; Grieco, C.; Purdum, G. E.; Ostroumov, E. E.; Granger, D. B.; Oblinsky, D. G.; Dean, J. C.; Doucette, G. S.; Asbury, J. B.; Yueh-Lin, L.; Seferos, D. S.; Anthony, J. E.; Scholes, G. D. Striking the Right Balance of Intermolecular Coupling for High-Efficiency Singlet Fission. *Chem. Sci.* **2018**, *9*, 6240–6259.

[56] Musser, A. J.; Liebel, M.; Schnedermann, C.; Wende, T.; Kehoe, T. B.; Rao, A.; Kukura, P. Evidence for Conical Intersection Dynamics Mediating Ultrafast Singlet Exciton Fission. *Nat. Phys.* **2015**, *11*, 352–357.

[57] Folie, B. D.; Haber, J. B.; Refaely-Abramson, S.; Neaton, J. B.; Ginsberg, N. S. Long-Lived Correlated Triplet Pairs in a π-Stacked Crystalline Pentacene Derivative. *J. Am. Chem. Soc.* **2018**, *140*, 2326–2335.

[58] Grieco, C.; Doucette, G. S.; Pensack, R. D.; Payne, M. M.; Rimshaw, A.; Scholes, G. D.; Anthony, J. E.; Asbury, J. B. Dynamic Exchange During Triplet Transport in Nanocrystalline TIPS-Pentacene Films. *J. Am. Chem. Soc.* **2016**, *138*, 16069–16080.

[59] Grieco, C.; Kennehan, E. R.; Kim, H.; Pensack, R. D.; Brigeman, A. N.; Rimshaw, A.; Payne, M. M.; Anthony, J. E.; Giebink, N. C.; Scholes, G. D.; Asbury, J. B. Direct Observation of Correlated Triplet Pair Dynamics during Singlet Fission using Ultrafast Mid-IR Spectroscopy. *J. Phys. Chem. C* **2018**, *122*, 2012–2022.

[60] Lee, T. S.; Lin, Y. L.; Kim, H.; Pensack, R. D.; Rand, B. P.; Scholes, G. D. Triplet Energy Transfer Governs the Dissociation of the Correlated Triplet Pair in Exothermic Singlet Fission. *J. Phys. Chem. Lett.* **2018**, *9*, 4087–4095.

[61] Wilson, M. W.; Rao, A.; Clark, J.; Kumar, R. S. S.; Brida, D.; Cerullo, G.; Friend, R. H. Ultrafast Dynamics of Exciton Fission in Polycrystalline Pentacene. *J. Am. Chem. Soc.* **2011**, *133*, 11830–11833.

[62] Smith, M. B.; Michl, J. Singlet Fission. *Chem. Rev.* **2010**, *110*, 6891–6936.

[63] Smith, M. B.; Michl, J. Recent Advances in Singlet Fission. *Annu. Rev. Phys. Chem.* **2013**, *64*, 361–386.

[64] Shockley, W.; Queisser, H. J. Detailed Balance Limit of Efficiency of P-N Junction Solar Cells. *J. Appl. Phys.* **1961**, *32*, 510–519.

[65] Lee, J.; Jadhav, P.; Reusswig, P. D.; Yost, S. R.; Thompson, N. J.; Congreve, D. N.; Hontz, E.; Van Voorhis, T.; Baldo, M. A. Singlet Exciton Fission Photovoltaics. *Acc. Chem. Res.* **2013**, *46*, 1300–1311.

[66] Singh, S.; Jones, W.; Siebrand, W.; Stoicheff, B.; Schneider, W. Laser Generation of Excitons and Fluorescence in Anthracene Crystals. *J. Chem. Phys.* **1965**, *42*, 330–342.

[67] Swenberg, C.; Stacy, W. Bimolecular Radiationless Transitions in Crystalline Tetracene. *Chem. Phys. Lett.* **1968**, *2*, 327–328.

[68] Casanova, D. Theoretical Modeling of Singlet Fission. *Chem. Rev.* **2018**, *118*, 7164–7207.

[69] Ehrler, B.; Musselman, K. P.; Böhm, M. L.; Friend, R. H.; Greenham, N. C. Hybrid Pentacene/A-Silicon Solar Cells Utilizing Multiple Carrier Generation Via Singlet Exciton Fission. *Appl. Phys. Lett.* **2012**, *101*, 153507.

[70] Congreve, D. N.; Lee, J.; Thompson, N. J.; Hontz, E.; Yost, S. R.; Reusswig, P. D.; Bahlke, M. E.; Reineke, S.; Van Voorhis, T.; Baldo, M. A. External Quantum Efficiency above 100% in a Singlet-Exciton-Fission–Based Organic Photovoltaic Cell. *Science* **2013**, *340*, 334–337.

[71] Yang, L.; Tabachnyk, M.; Bayliss, S. L.; Böhm, M. L.; Broch, K.; Greenham, N. C.; Friend, R. H.; Ehrler, B. Solution-Processable Singlet Fission Photovoltaic Devices. *Nano Lett.* **2015**, *15*, 354–358.

[72] Pazos-Outón, L. M.; Lee, J. M.; Futscher, M. H.; Kirch, A.; Tabachnyk, M.; Friend, R. H.; Ehrler, B. A Silicon–Singlet Fission Tandem Solar Cell Exceeding 100% External Quantum Efficiency with High Spectral Stability. *ACS Energy Lett.* **2017**, *2*, 476–480.

[73] Rao, A.; Friend, R. H. Harnessing Singlet Exciton Fission to Break the Shockley–Queisser Limit. *Nat. Rev. Mater.* **2017**, *2*, 1–12.

[74] Grieco, C.; Doucette, G. S.; Munson, K. T.; Swartzfager, J. R.; Munro, J. M.; Anthony, J. E.; Dabo, I.; Asbury, J. B. Vibrational Probe of the Origin of Singlet Exciton Fission in TIPS-pentacene Solutions. *J. Chem. Phys.* **2019**, *151*, 154701.

[75] Wilson, M. W.; Rao, A.; Ehrler, B.; Friend, R. H. Singlet Exciton Fission in Polycrystalline Pentacene: From Photophysics toward Devices. *Acc. Chem. Res.* **2013**, *46*, 1330–1338.

[76] Yost, S. R.; Lee, J.; Wilson, M. W.; Wu, T.; McMahon, D. P.; Parkhurst, R. R.; Thompson, N. J.; Congreve, D. N.; Rao, A.; Johnson, K.; Sfeir, M. Y.; Bawendi, M. G.; Swager, T. M.; Friend, R. H.; Baldo, M. A.; Van Voorhis, T. A Transferable Model for Singlet-Fission Kinetics. *Nat. Chem.* **2014**, *6*, 492–497.

[77] Šanda, F.; Perlík, V.; Lincoln, C. N.; Hauer, J. Center Line Slope Analysis in Two-Dimensional Electronic Spectroscopy. *J. Phys. Chem. A* **2015**, *119*, 10893–10909.

[78] Wells, K. L.; Zhang, Z.; Rouxel, J. R.; Tan, H.-S. Measuring the Spectral Diffusion of Chlorophyll a Using Two-Dimensional Electronic Spectroscopy. *J. Phys. Chem. B* **2013**, *117*, 2294–2299.

[79] Khyasudeen, M. F.; Nowakowski, P. J.; Tan, H.-S. Measuring the Ultrafast Correlation Dynamics between the Qx and Qy Bands in Chlorophyll Molecules. *J. Phys. Chem. B* **2019**, *123*, 1359–1364.

[80] Khyasudeen, M. F.; Nowakowski, P. J.; Nguyen, H. L.; Sim, J. H.; Do, T. N.; Tan, H.-S. Studying the Spectral Diffusion Dynamics of Chlorophyll a and Chlorophyll b Using Two-Dimensional Electronic Spectroscopy. *Chem. Phys.* **2019**, *527*, 110480.

[81] *Zetasizer Nano Series User Manual*; Malvern Instruments Ltd., 2004.

[82] *Dynamic Light Scattering, Common Terms Defined*; Malvern Instruments Ltd., 2011; pp 1–6.

[83] Alvarez-Buylla, A.; Ling, C.-Y.; Kirn, J. R. Cresyl Violet: A Red Fluorescent Nissl Stain. *J. Neurosci. Meth.* **1990**, *33*, 129–133.

[84] Gacoin, P.; Flamant, P. High Efficiency Cresyl Violet Laser. *Opt. Commun.* **1972**, *5*, 351–353.

[85] Schmidt, W.; Appt, W.; Wittekindt, N. Characteristics of a Cresyl Violet Laser. *Zeitschrift für Naturforschung A* **1972**, *27*, 37–41.

[86] Ma, X.; Dostál, J.; Brixner, T. Broadband 7-fs Diffractive-optic-based 2d Electronic Spectroscopy Using Hollow-core Fiber Compression. *Opt. Express* **2016**, *24*, 20781–20791.

[87] Bizimana, L. A.; Brazard, J.; Carbery, W. P.; Gellen, T.; Turner, D. B. Resolving

Molecular Vibronic Structure Using High-sensitivity Two-dimensional Electronic Spectroscopy. *J. Chem. Phys.* **2015**, *143*, 164203.

[88] Carbery, W. P.; Pinto-Pacheco, B.; Buccella, D.; Turner, D. B. Resolving the Fluorescence Quenching Mechanism of an Oxazine Dye Using Ultrabroadband Two-Dimensional Electronic Spectroscopy. *J. Phys. Chem. A* **2019**, *123*, 5072–5080.

[89] Turner, D. B.; Wilk, K. E.; Curmi, P. M.; Scholes, G. D. Comparison of Electronic and Vibrational Coherence Measured by Two-dimensional Electronic Spectroscopy. *J. Phys. Chem. Lett.* **2011**, *2*, 1904–1911.

[90] Heisler, I. A.; Moca, R.; Camargo, F. V.; Meech, S. R. Two-dimensional Electronic Spectroscopy Based on Conventional Optics and Fast Dual Chopper Data Acquisition. *Rev. Sci. Instrum.* **2014**, *85*, 063103.

[91] Lu, J.; Lee, Y.; Anna, J. M. Extracting the Frequency Dependent Dynamic Stokes Shift from Two-Dimensional Electronic Spectra with Prominent Vibrational Coherences. *J. Phys. Chem. B* **2020**, *124*, 8857–8867.

[92] Vogel, E.; Gbureck, A.; Kiefer, W. Vibrational Spectroscopic Studies on the Dyes Cresyl Violet and Coumarin 152. *J. Mol. Struct.* **2000**, *550*, 177–190.

[93] Fleming, G. R.; Cho, M. Chromophore–Solvent Dynamics. *Ann. Phys. Chem.* **1996**, *47*, 109–134.

[94] Smith, J. O. *Mathematics of the Discrete Fourier Transform (DFT)*; `http://-ccrma.stanford.edu/~jos/mdft/`, accessed 18th September 2020; online book, 2007 edition.

[95] Dyson, R.; Maeder, M.; Puxty, G.; Neuhold, Y.-M. Simulation of Complex Chemical Kinetics. *BioInorg. React. Mech.* **2003**, *5*, 39–46.

[96] Puxty, G.; Maeder, M.; Hungerbühler, K. Tutorial on the Fitting of Kinetics Models to Multivariate Spectroscopic Measurements with Non-linear Least-squares Regression. *Chemom. Intell. Lab. Syst.* **2006**, *81*, 149–164.

[97] Rafiq, S.; Scholes, G. D. Slow Intramolecular Vibrational Relaxation Leads to Long-lived Excited-state Wavepackets. *J. Phys. Chem. A* **2016**, *120*, 6792–6799.

[98] Aragó, J.; Viruela, P. M.; Ortí, E.; Osuna, R. M.; Hernández, V.; Navarrete, J. T. L.; Swartz, C. R.; Anthony, J. E. Functionalized Pentacenes: a Combined Theoretical, Raman and UV–Vis Spectroscopic Study. *Theor. Chem. Acc.* **2011**, *128*, 521–530.

[99] Fransted, K. A.; Caram, J. R.; Hayes, D.; Engel, G. S. Two-dimensional Electronic Spectroscopy of Bacteriochlorophyll a in Solution: Elucidating the Coherence Dynamics of the Fenna-Matthews-Olson Complex Using Its Chromophore As a Control. *J. Chem. Phys.* **2012**, *137*, 125101.

[100] Irgen-Gioro, S.; Spencer, A. P.; Hutson, W. O.; Harel, E. Coherences of Bacteriochlorophyll a Uncovered using 3D-Electronic Spectroscopy. *J. Phys. Chem. Lett.* **2018**, *9*, 6077–6081.

[101] Caram, J. R.; Zheng, H.; Dahlberg, P. D.; Rolczynski, B. S.; Griffin, G. B.; Fidler, A. F.; Dolzhnikov, D. S.; Talapin, D. V.; Engel, G. S. Persistent Interexcitonic Quantum Coherence in CdSe Quantum Dots. *J. Phys. Chem. Lett.* **2014**,

5, 196–204.

[102] Kapitán, J.; Hecht, L.; Bouř, P. Raman Spectral Evidence of Methyl Rotation in Liquid Toluene. *Phys. Chem. Chem. Phys.* **2008**, *10*, 1003–1008.

[103] Takasu, Y.; Matsumoto, S.; Fujii, Y.; Nishio, I. Raman Study of the Low Temperature Behavior of Tetrahydrofuran Molecule in the Cage of Clathrate Hydrate. *Chem. Phys. Lett.* **2015**, *627*, 39–43.

[104] Jensen, L.; Mortensen, P. M.; Trane, R.; Harris, P.; Berg, R. W. Reaction Kinetics of Acetone Peroxide Formation and Structure Investigations Using Raman Spectroscopy and X-Ray Diffraction. *Appl. Spectrosc.* **2009**, *63*, 92–97.

[105] Tolles, W. M.; Nibler, J.; McDonald, J.; Harvey, A. A Review of the Theory and Application of Coherent Anti-Stokes Raman Spectroscopy (CARS). *Appl. Spectrosc.* **1977**, *31*, 253–271.

[106] Begley, R.; Harvey, A.; Byer, R. L. Coherent Anti-Stokes Raman Spectroscopy. *Appl. Phys. Lett.* **1974**, *25*, 387–390.

[107] Joo, T.; Dugan, M.; Albrecht, A. Time-resolved Coherent Stokes Raman Spectroscopy (CSRS) of Benzene. *Chem. Phys. Lett.* **1991**, *177*, 4–10.

[108] Kolesnichenko, P. V.; Tollerud, J. O.; Davis, J. A. Background-free Time-resolved Coherent Raman Spectroscopy (CSRS and CARS): Heterodyne Detection of Low-energy Vibrations and Identification of Excited-state Contributions. *APL Photonics* **2019**, *4*, 056102.

[109] Brüggemann, B.; Pullerits, T. Nonperturbative Modeling of Fifth-Order Coherent Multidimensional Spectroscopy in Light Harvesting Antennas. *New J. Phys.* **2011**, *13*, 025024.

[110] Fulmer, E. C.; Ding, F.; Zanni, M. T. Heterodyned Fifth-Order 2D-IR Spectroscopy of the Azide Ion in an Ionic Glass. *J. Chem. Phys.* **2005**, *122*, 034302.

[111] Ding, F.; Fulmer, E. C.; Zanni, M. T. Heterodyned Fifth-Order Two-Dimensional IR Spectroscopy: Third-Quantum States and Polarization Selectivity. *J. Chem. Phys.* **2005**, *123*, 094502.

[112] Farfan, C. A.; Turner, D. B. Interference among Multiple Vibronic Modes in Two-Dimensional Electronic Spectroscopy. *Mathematics* **2020**, *8*, 157.

[113] Platt, A. D.; Day, J.; Subramanian, S.; Anthony, J. E.; Ostroverkhova, O. Optical, Fluorescent, and (Photo) Conductive Properties of High-Performance Functionalized Pentacene and Anthradithiophene Derivatives. *J. Phys. Chem. C* **2009**, *113*, 14006–14014.

[114] Lehnherr, D.; Gao, J.; Hegmann, F. A.; Tykwinski, R. R. Synthesis and Electronic Properties of Conjugated Pentacene Dimers. *Org. Lett.* **2008**, *10*, 4779–4782.

[115] Sharifzadeh, S.; Wong, C. Y.; Wu, H.; Cotts, B. L.; Kronik, L.; Ginsberg, N. S.; Neaton, J. B. Relating the Physical Structure and Optoelectronic Function of Crystalline TIPS-Pentacene. *Adv. Funct. Mater.* **2015**, *25*, 2038–2046.

[116] Carey, D. M.; Korenowski, G. M. Measurement of the Raman Spectrum of Liquid Water. *J. Chem. Phys.* **1998**, *108*, 2669–2675.

[117] Omkaram, I.; Chakradhar, R. S.; Rao, J. L. EPR, Optical, Infrared and Raman Studies of VO2+ Ions in Polyvinylalcohol Films. *Physica B Condens. Matter* **2007**, *388*, 318–325.

[118] Prosanov, I. Y.; Matvienko, A. Study of PVA Thermal Destruction by Means of IR and Raman Spectroscopy. *Phys. Solid State* **2010**, *52*, 2203–2206.

[119] Romero, E.; Prior, J.; Chin, A. W.; Morgan, S. E.; Novoderezhkin, V. I.; Plenio, M. B.; van Grondelle, R. Quantum–Coherent Dynamics in Photosynthetic Charge Separation Revealed by Wavelet Analysis. *Sci. Rep.* **2017**, *7*, 1–8.